Molecular Cell

Article

Ca^{2+}/calmodulin-dependent protein kinase II β decodes ER Ca^{2+} transients to trigger autophagosome formation

Graphical abstract

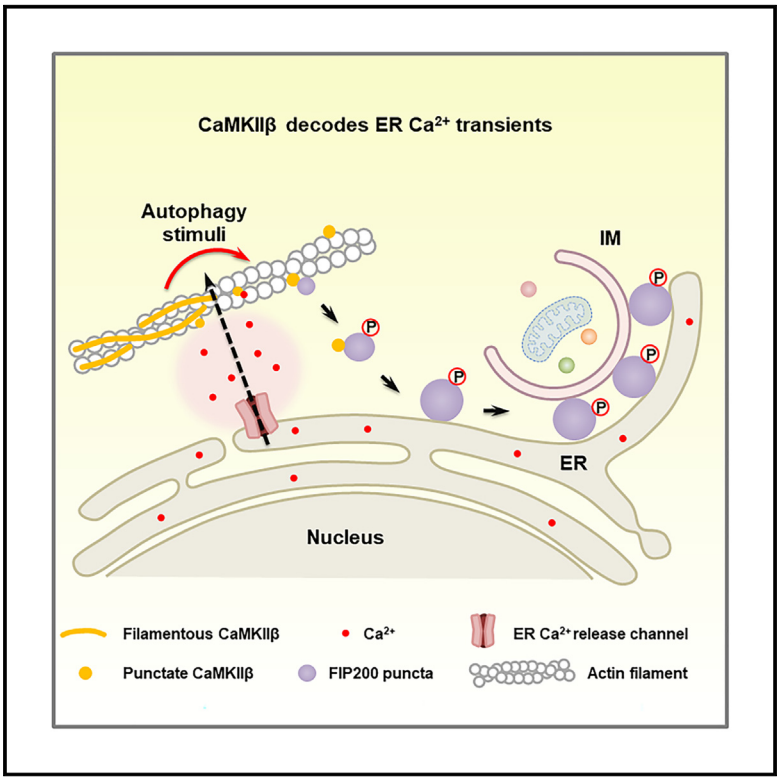

Authors

Qiaoxia Zheng, Huan Zhang, Hongyu Zhao, ..., Youjun Wang, Mingjie Zhang, Hong Zhang

Correspondence

hongzhang@ibp.ac.cn

In brief

Zheng et al. show that in response to ER Ca^{2+} transients, CaMKIIβ is recruited from actin filaments to modulate phase separation of the FIP200 complex, thereby controlling the organization of autophagosome initiation sites. CaMKIIβ is also essential for sustaining ER Ca^{2+} transients during autophagy induction.

Highlights

- CaMKIIβ decodes ER Ca^{2+} transients to trigger autophagosome formation
- CaMKIIβ phosphorylates FIP200 to modulate LLPS of the FIP200 complex
- CaMKIIβ controls propagation of ER Ca^{2+} transients during autophagy induction
- CaMKIIβ mutations in the neurodevelopmental disorder MRD54 affect autophagy

Zheng et al., 2025, Molecular Cell *85*, 620–637
February 6, 2025
https://doi.org/10.1016/j.molcel.2024.12.005

CellPress

CellPress

Molecular Cell

Article

Ca^{2+}/calmodulin-dependent protein kinase II β decodes ER Ca^{2+} transients to trigger autophagosome formation

Qiaoxia Zheng,[1,2,9] Huan Zhang,[1,3,9] Hongyu Zhao,[1] Yong Chen,[1] Hongzhining Yang,[4] Tingting Li,[4] Qixu Cai,[5] Yingyu Chen,[3] Youjun Wang,[6] Mingjie Zhang,[7] and Hong Zhang[1,8,10,*]

[1]National Laboratory of Biomacromolecules, New Cornerstone Science Laboratory, Institute of Biophysics, Chinese Academy of Sciences, Beijing 100101, China
[2]Department of Physiology and Pathophysiology, School of Basic Medical Sciences, Peking University, Beijing 100191, China
[3]Department of Immunology, School of Basic Medical Sciences, Peking University, Beijing 100191, China
[4]Department of Medical Bioinformatics, School of Basic Medical Sciences, Peking University, Beijing 100191, China
[5]School of Public Health, Xiamen University, Xiamen 361102, China
[6]College of Life Sciences, Beijing Normal University, Beijing 100875, China
[7]School of Life Sciences, Southern University of Science and Technology, Shenzhen 518055, China
[8]College of Life Sciences, University of Chinese Academy of Sciences, Beijing 100049, China
[9]These authors contributed equally
[10]Lead contact
*Correspondence: hongzhang@ibp.ac.cn
https://doi.org/10.1016/j.molcel.2024.12.005

SUMMARY

In multicellular organisms, very little is known about how Ca^{2+} transients on the ER outer surface elicited by autophagy stimuli are sustained and decoded to trigger autophagosome formation. Here, we show that Ca^{2+}/calmodulin-dependent protein kinase II β (CaMKIIβ) integrates ER Ca^{2+} transients to trigger liquid-liquid phase separation (LLPS) of the autophagosome-initiating FIP200 complex. In response to ER Ca^{2+} transients, CaMKIIβ is recruited from actin filaments and forms condensates, which serve as sites for the emergence of or interaction with FIP200 puncta. CaMKIIβ phosphorylates FIP200 at Thr269, Thr1127, and Ser1484 to modulate LLPS and properties of the FIP200 complex, thereby controlling its function in autophagosome formation. CaMKIIβ also controls the amplitude, duration, and propagation of ER Ca^{2+} transients during autophagy induction. CaMKIIβ mutations identified in the neurodevelopmental disorder MRD54 affect the function of CaMKIIβ in autophagy. Our study reveals that CaMKIIβ is essential for sustaining and decoding ER Ca^{2+} transients to specify autophagosome formation in mammalian cells.

INTRODUCTION

Ca^{2+} acts as a versatile signal to control a myriad of cellular activities.[1,2] Ca^{2+} signals are transduced through various Ca^{2+}-binding effectors[1] and also multiple Ca^{2+} or Ca^{2+}/calmodulin (CaM)-dependent protein kinases (CDPKs or CaMKs) that phosphorylate downstream factors.[3,4] Ca^{2+} signals are highly dynamic, exhibiting complex spatiotemporal forms such as Ca^{2+} transients that differ in frequency, amplitude, and duration.[1,5]

One of the molecular machineries to decode frequency-encoded Ca^{2+} signals is Ca^{2+}/CaM-dependent protein kinase II (CaMKII), which belongs to a family of multifunctional CaMKs.[6–8] The four members of the CaMKII subfamily—α, β, γ, and δ—are differentially expressed in different tissues and also differ in actin-binding activity. CaMKII contains an N-terminal catalytic domain, a regulatory domain, a variable domain, and a C-terminal association domain. The regulatory domain contains autoinhibitory and Ca^{2+}/CaM-binding regions, while the association domain drives the assembly of CaMKII into a holoenzyme, typically a dodecamer.[9–11] Upon binding of Ca^{2+}/CaM, the basal autoinhibited state of CaMKII is relieved, resulting in autophosphorylation at Thr287 (the residue number corresponds to CaMKIIβ) that further activates the kinase. Activated CaMKII remains partially active after dissociation of Ca^{2+}/CaM, and the degree of this autonomous activity is specified by the frequency, amplitude, and duration of Ca^{2+} pulses.[7,9,11] CaMKII, via both enzymatic and structural roles, functions in various physiological events.[8,10,12] For example, CaMKII decodes and transduces synaptic Ca^{2+} signals to control multiple aspects of neural functions such as synaptic plasticity, learning, and memory.[8,13] Perturbation of CaMKII function is associated with neuropsychiatric and neurodevelopmental disorders, including depression, schizophrenia, and mental retardation.[14–17]

Autophagy involves the engulfment of a portion of the cytosol into double-membrane autophagosomes and their subsequent

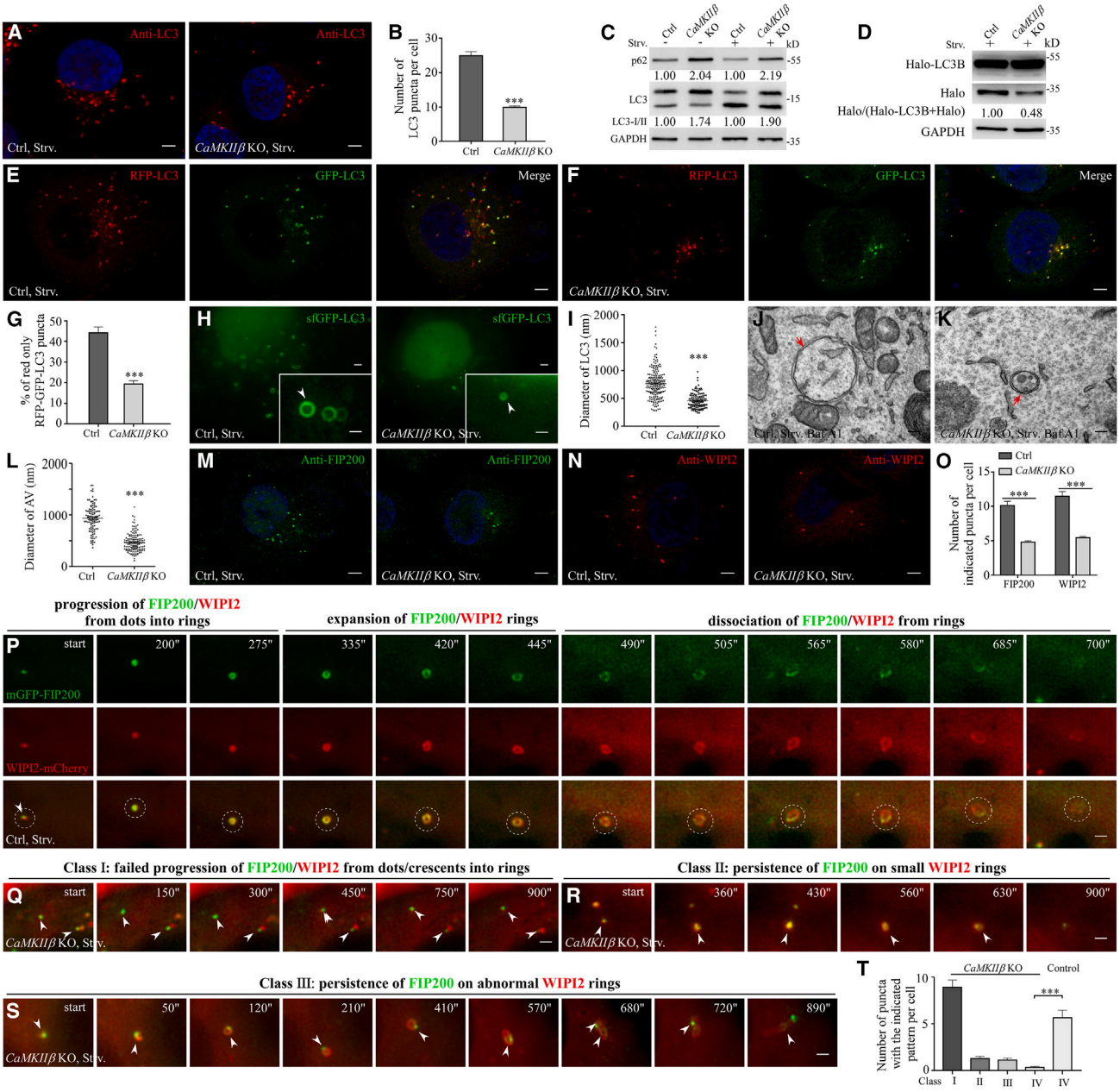

Figure 1. Depleting CaMKIIβ blocks autophagy

(A and B) Compared with starved control cells, the number of LC3 puncta is dramatically decreased in starved *CaMKIIβ* knockout (KO) cells. (B) Shows quantification results (n = 44 and 49 for control and *CaMKIIβ* KO cells, respectively).

(C) Levels of p62 and the ratio of LC3-I/LC3-II are increased in *CaMKIIβ* KO cells. Quantifications are shown under each blot. The level in control cells is set to 1.00.

(D) The ratio of Halo/(Halo -LC3B+Halo) is reduced in *CaMKIIβ* KO cells under starved conditions.

(E–G) Many red RFP-GFP-LC3 puncta accumulate in control cells after 4 h amino acid starvation, while the majority of LC3 puncta are yellow in starved *CaMKIIβ* KO cells. Quantifications are shown in (G) (n = 23 and 28 for control and *CaMKIIβ* KO cells, respectively).

(H and I) Multi-SIM imaging shows that the size of LC3 ring structures in starved *CaMKIIβ* KO cells is smaller than control cells. Quantifications are shown in (I) (n = 35 and 35 for control and *CaMKIIβ* KO cells, respectively).

(J–L) TEM analysis of autophagosomes (AVs, arrows) in starved control and *CaMKIIβ* KO cells after BafA1 treatment. Column scatter chart in (L) shows the size of AVs/unclosed AVs (n = 70 and 78 for control and *CaMKIIβ* KO cells, respectively).

(M–O) The numbers of FIP200 puncta and WIPI2 puncta are dramatically reduced in starved *CaMKIIβ* KO cells compared with control cells. (O) Shows quantification results (n = 34, 40, 34, and 42 cells for bars from left to right).

(P–S) Multi-SIM imaging analysis of dynamic progression of FIP200-labeled structures. In control cells (*CaMKIIβ* KO cells expressing SNAP-CaMKIIβ) (P), FIP200/WIPI2 dots progress into ring-like structures. FIP200/WIPI2 then dissociate from the rings and disappear. Several classes of defects are observed in *CaMKIIβ* KO

(legend continued on next page)

delivery to lysosomes for degradation.[18–21] It is crucial for cells to cope with various stresses, such as starvation, and to maintain homeostasis.[22,23] Dysfunction of autophagy is associated with various human pathologies, including cancer, neurodegenerative diseases, and immune disorders.[24–26] Autophagosome formation in multicellular organisms starts with the initiation and nucleation of an autophagosomal isolation membrane (IM, autophagosomal precursor) on the ER, followed by its expansion and closure.[19,27–29] A set of autophagy genes, including *ATG* genes and metazoan-specific *EPG* genes, act at different steps of autophagosome formation.[30,31] Mechanistically, upon autophagy induction, the most upstream-acting complex, i.e., the FIP200 complex (composed of FIP200, ATG13, ATG101, and ULK1), forms ER-associated puncta to constitute autophagosome initiation sites.[32,33] Other autophagy proteins are then recruited for IM nucleation and expansion.[34,35]

Autophagosome initiation is specified by Ca^{2+} transients on the ER cytosolic surface elicited by autophagy stimuli.[36,37] The ER Ca^{2+} transients during autophagy induction are dynamic in nature and can propagate from a local signal into a large or global signal on the ER network.[36] ER Ca^{2+} transients trigger liquid-liquid phase separation (LLPS) of the FIP200 complex, and the resultant puncta associate with the ER.[36] Dynamic Ca^{2+} signals on the ER are generated via concerted actions of Ca^{2+} channels such as IP3Rs (inositol 1,4,5-trisphosphate receptors) and RyRs (ryanodine receptors) and Ca^{2+} pumps such as SERCAs (sarcoplasmic/endoplasmic reticulum Ca^{2+}-ATPase).[1,2,5] The Ca^{2+}-induced Ca^{2+} release property of Ca^{2+} channels enables local Ca^{2+} signals to propagate into regional or global signals.[38,39] On the other hand, the Ca^{2+} level dissipates sharply with distance from active channels by diffusion, by association with Ca^{2+}-binding proteins, and also by pumps and exchangers that remove Ca^{2+} from the cytosol into storage compartments.[1,40] The activities of Ca^{2+} channels and pumps are controlled by interacting proteins, and also by stress-sensing kinases and phosphatase-mediated phosphorylation levels.[41,42] For example, the autophagy protein EPG-4/EI24 interacts with IP3Rs and SERCAs to modulate ER Ca^{2+} transients.[36] It is unknown how ER Ca^{2+} transients are sustained during the period of autophagy induction and how they are decoded to trigger the formation of ER-associated FIP200 puncta.

Here, we show that in response to Ca^{2+} transients, the actin filament-bound CaMKIIβ forms condensates with which FIP200 puncta associate. CaMKIIβ phosphorylates FIP200, which modulates LLPS of the FIP200 complex and induces organization of FIP200 puncta into functional autophagosome formation sites. Our results indicate that CaMKIIβ is involved in transducing Ca^{2+} transients to initiate autophagosome formation.

RESULTS

Depleting CaMKIIβ blocks autophagy

We investigated whether CaMKII kinases are required for autophagy. Compared with control cells, the number of LC3 puncta was dramatically reduced in *CaMKIIβ* knockout (KO) COS7 cells under starvation conditions (Figures 1A and 1B), while levels of p62 and the ratio of LC3-I/LC3-II were increased (Figure 1C). Upon BafA1 treatment, which blocks formation of degradative autolysosomes,[43] starved *CaMKIIβ* KO cells contained far fewer LC3 puncta than starved control cells (Figures S1A and S1B). The HaloTag-LC3 processing assay measures autophagic flux.[44] Upon binding to tetramethylrhodamine (TMR)-conjugated ligand, Halo becomes resistant to proteolysis and accumulates in lysosomes. The ratio of $Halo^{TMR}$/($Halo^{TMR}$-LC3B + $Halo^{TMR}$) was reduced in starved *CaMKIIβ* KO cells compared with control cells (Figure 1D). The ratio of red RFP-GFP-LC3 puncta (due to the quenching of GFP fluorescence in acidified compartments) in *CaMKIIβ* KO cells 4 h after starvation was much less than in control cells (Figures 1E–1G). Consistent with this, LC3 puncta were largely separate from LysoTracker-labeled lysosomes in starved *CaMKIIβ* KO cells (Figures S1C–S1E). The number of LC3 puncta was increased in *CaMKIIα* knockdown (KD) cells but remained unaltered in cells depleted of *CaMKIIγ* and *CaMKIIδ* (Figures S1F–S1I). The number of LC3 puncta induced by Torin1 treatment was also dramatically reduced in *CaMKIIβ* KO cells compared with control cells (Figures S1J and S1S).

Super-resolution multi-SIM analysis showed that the size of LC3-ring structures was much smaller in *CaMKIIβ* KO cells than in control cells after starvation (Figures 1H and 1I). Transmission electron microscopy (TEM) analysis revealed that in BafA1-treated starved control cells, autophagosomes and amphisomes (hybrid structures resulted from fusion of autophagosomes with endosomes) accumulated (Figures 1J and S1M). By contrast, *CaMKIIβ* KO cells contained fewer and smaller autophagosomes (Figures 1K, 1L, S1N, and S1O). Some autophagic structures were non-spherical and unclosed (Figure S1N). Taken together, our results indicate that CaMKIIβ is required for autophagosome formation.

CaMKIIβ is essential for the assembly of FIP200-labeled autophagosome initiation sites and their progression into autophagosomes

We next examined which step of autophagosome formation was impaired in *CaMKIIβ* KO cells. Levels of autophagy proteins, including FIP200, ULK1, ATG13, ATG101, and WIPI2, remained unaltered in *CaMKIIβ* KO cells (Figure S1P). The numbers of autophagosome formation sites indicated as FIP200 puncta and IMs indicated as WIPI2 puncta were reduced in *CaMKIIβ* KO

cells (Q–S). "Start" refers to the start point for imaging. Similar-sized dot structures were analyzed for their dynamic progression into autophagic structures. The duration of the dot stage was variable.

(T) Quantification of different FIP200/WIPI2 organization patterns. I, II, III indicate the defective patterns shown in (Q)–(S). Class IV indicates progression of FIP200/WIPI2 dots to normal autophagosomes during the imaging time course. After cells were starved for 3 h, multi-SIM imaging was performed for 60 min at intervals of 15 s (n = 231 FIP200 puncta from 20 *CaMKIIβ* KO cells and n = 66 FIP200 puncta from 10 control cells).

In this study, COS7 cells were used unless otherwise noted. Strv, starvation. Data are shown as mean ± SEM. ns, no significant difference; $^{*}p < 0.05$; $^{**}p < 0.01$; $^{***}p < 0.001$. Scale bars: 5 μm (A, E, F, M, and N), 2 μm (H), 1 μm (P–S and inserts in H), and 200 nm (J and K).

See also Figure S1.

cells compared with control cells under starvation conditions or Torin1 treatment (Figures 1M–1O and S1Q–S1S). The same defects were detected in *CaMKIIβ* KD Hela and SHSY5Y cells (Figures S1K, S1L, and S1T–S1V). In the rest of the study, we focused on *CaMKIIβ* KO COS7 cells.

CaMKII activity is inhibited by the CN21 peptide with high specificity and potency.[45] Expressing GFP-CN21 reduced the number of FIP200 puncta, WIPI2 puncta, and LC3 puncta in starved control cells (Figures S1W–S1Z) but did not further exacerbate the defect in *CaMKIIβ* KO cells (Figures S1A1 and S1B1). Depleting *CaMKIIα*, *CaMKIIγ*, and *CaMKIIδ* had no evident effect on the formation of FIP200 puncta or WIPI2 puncta (Figures S1C1–S1E1).

We then used multi-SIM to examine the dynamics of FIP200 structures during autophagosome formation. WIPI2 was used to label IMs. FIP200 and WIPI2 first formed small dots that were closely associated (Figure 1P). They then elongated into crescent-shaped and small ring-like structures (unclosed) that further expanded into large ring structures. FIP200/WIPI2 signals gradually dissolved from the enlarged ring structures and eventually disappeared (Figure 1P). The whole process, from dots to the disappearance of WIPI2 from ring structures, took ~700 s in starved control cells (Figures 1P and S1F1). In starved *CaMKIIβ* KO cells, we observed three classes of defects in this process. In class I defects, small FIP200 puncta were stably associated with WIPI2 puncta that failed to enlarge during the observation time (900 s) (Figures 1Q and 1T). In class II defects, WIPI2 dots expanded into small autophagosomes with persistent FIP200, which indicates failed closure of IMs (Figures 1R and 1T). In class III defects, the dots expanded into irregularly shaped ring structures, also with persistent FIP200 (Figures 1S and 1T). Thus, CaMKIIβ controls the formation of FIP200 puncta and their organization into functional autophagosome formation sites.

The kinase and actin-binding activities of CaMKIIβ are required for its function in autophagosome formation

We determined whether the kinase activity of CaMKIIβ is required for its function in autophagy (Figure 2A). The autophagy defects in *CaMKIIβ* KO cells were rescued by expression of SNAP (self-labeling protein tag)-CaMKIIβ but not by kinase-attenuated CaMKIIβ(K43R or T287A) mutants (Figures 2B–2D, S2A, S2B, and S2I). Low-level expression of constitutively active SNAP-CaMKIIβ(T287D), but not SNAP-CaMKIIβ(K43R T287D), also rescued the defect in *CaMKIIβ* KO cells (Figures S2C, S2D, S2F, S2G, and S2M). However, high-level expression of SNAP-CaMKIIβ(T287D) failed to rescue the defect (Figures S2E, S2H, and S2M) and even inhibited autophagy in control cells (Figures S2J–S2L and S2N). Thus, a properly controlled level of CaMKIIβ kinase activity is essential for its function in autophagosome formation.

Time-lapse multi-SIM analysis showed that in *CaMKIIβ* KO cells expressing SNAP-CaMKIIβ(T287A or K43R), as in *CaMKIIβ* KO cells, FIP200 puncta exhibited defects in organization into functional autophagosome formation sites, including failed expansion of FIP200/WIPI2 dots, formation of small autophagosomes, and persistence of FIP200/WIPI2 on the ring structures (Figures 2E, S2O, and S2P). In *CaMKIIβ* KO cells expressing a low level of SNAP-CaMKIIβ(T287D), progression of FIP200/WIPI2 dots to ring-like structures and also dissociation of FIP200/WIPI2 from ring structures were faster than in control cells (Figures 1P, 2F, S1F1, and S2Q).

CaMKIIβ contains an actin-binding region (V1) (Figure 2A). The association of CaMKIIβ with actin filaments (filamentous actin [F-actin]) is disrupted by the binding of Ca^{2+}/CaM and the resultant autophosphorylation at the F-actin-binding region.[8,46,47] Consistent with this, SNAP-CaMKIIβ exhibited filamentous distribution under normal growth conditions (Figure 2G). CaMKIIβ with a deletion of the actin-binding motif (CaMKIIβ(ΔV1)) and SNAP-CaMKIIβ(T287D) exhibited a diffuse distribution pattern (Figures 2H and 2I). CaMKIIβ(ΔV1) failed to rescue the autophagy defect in *CaMKIIβ* KO cells (Figures 2B–2D, S2A, S2B, and S2I). Thus, both the kinase and actin-binding activities are essential for the function of CaMKIIβ in autophagosome formation.

LLPS of the FIP200 complex is also triggered by exogenous (exo) Ca^{2+} stimulation (adding Ca^{2+} in the culture medium), which causes an abrupt increase in cytosolic Ca^{2+} transients (Figure S2R).[36] Compared with control cells, mGFP-FIP200 puncta were much less abundant in *CaMKIIβ* KO cells upon exo Ca^{2+} stimulation (Figure 2J). Fluorescence recovery after photobleaching (FRAP) assays showed that the recovery of fluorescence signal in bleached mGFP-FIP200 puncta was slower in *CaMKIIβ* KO cells than in control cells (Figures S2S–S2U). There were also fewer mGFP-FIP200 puncta in *CaMKIIβ* KO cells expressing CaMKIIβ(T287A, K43R, or ΔV1) mutants (Figure S2V).

ER Ca^{2+} transients trigger formation of CaMKIIβ puncta

We investigated how CaMKIIβ responds to ER Ca^{2+} transients elicited by autophagy stimuli. Upon Hank's balanced salt solution (HBSS) starvation, SNAP-CaMKIIβ formed distinct puncta, and the number and intensity of puncta gradually increased as the starvation proceeded (Figures 2K and 2L). Formation of CaMKIIβ puncta was inhibited by BAPTA-AM (cell-permeant intracellular Ca^{2+} chelator) treatment (Figure S2W). When expressed at a similar level (Figure S2X), SNAP-CaMKIIβ(T287A or K43R) exhibited filamentous distribution under nutrient-rich conditions (Figures S2Y and S2Z) and formed fewer puncta after starvation than SNAP-CaMKIIβ (Figure S2A1). SNAP-CaMKIIα, SNAP-CaMKIIβ(T287D), and SNAP-CaMKIIβ(ΔV1) were diffuse under both fed and starvation conditions (Figures S2B1–S2D1). In *EI24* KO cells, in which ER Ca^{2+} transients are much stronger in amplitude and show oscillations,[36] SNAP-CaMKIIβ puncta were more abundant than in control cells (Figures S2E1 and S2F1).

We next analyzed the dynamic formation of CaMKIIβ puncta. Under normal growth conditions, CaMKIIβ was attached on F-actin, although the signal was not homogeneously distributed (Figure S3A). Upon HBSS starvation, the CaMKIIβ signal on F-actin became discontinuous at some places, which we called "breakage sites" in the CaMKIIβ filaments. The underlying actin filaments, however, remained intact (Figures S3A and S3D). At these breakage sites, CaMKIIβ concentrated into distinct puncta that associated with or were adjacent to F-actin (Figures S3A–S3D and S3I). CaMKIIβ puncta also accumulated in the cytosol, separate from F-actin (Figures S3B, S3C, and S3I). Gradual growth and fusion of small CaMKIIβ puncta were observed (Figure S3E). CaMKIIβ puncta were dynamic during starvation. They migrated from CaMKIIβ filaments into the cytosol (Figure S3F). They also moved away from F-actin and fused with cytosolic

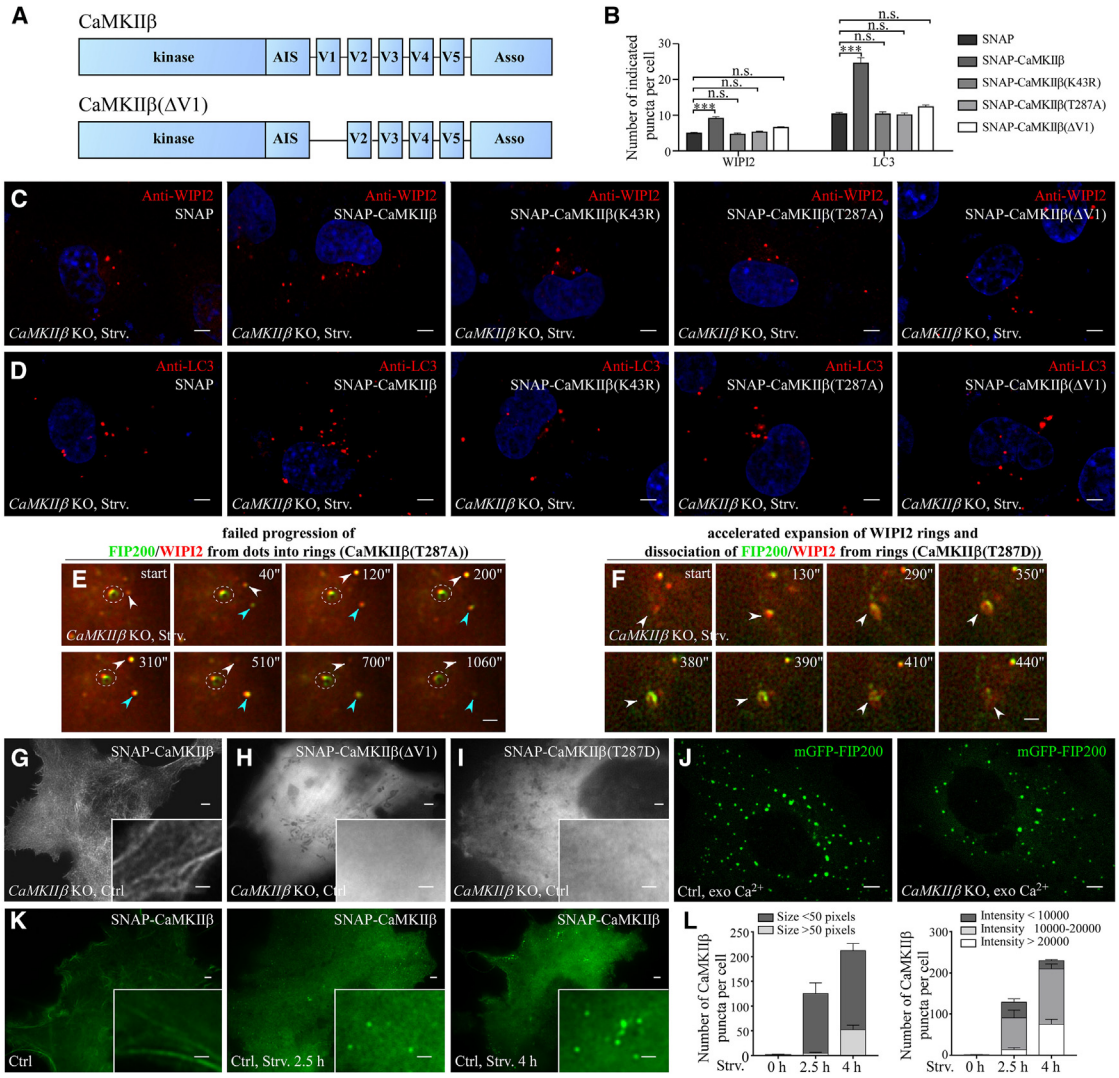

Figure 2. The kinase activity of CaMKIIβ is required for its function in autophagosome formation

(A) Schematic illustration of domains in wild-type and V1-deleted CaMKIIβ. AIS, autoinhibitory segment. Asso, association domain.

(B–D) The formation of WIPI2 puncta (C) and LC3 puncta (D) in starved *CaMKIIβ* KO cells expressing wild-type or mutant CaMKIIβ. (B) Shows quantifications (for bars from left to right: n = 30, 27, 29, 33, and 24 cells for WIPI2 puncta; n = 33, 27, 30, 24, and 26 cells for LC3 puncta).

(E) Multi-SIM analysis showing that in starved *CaMKIIβ* KO cells expressing CaMKIIβ(T287A), FIP200/WIPI2 forms dots (arrows) or small ring-like structures (dashed circles).

(F) Expressing CaMKIIβ(T287D) facilitates the progression of autophagosome formation. The channels showing expression of SNAP-CaMKIIβ mutants are not displayed in (E) and (F).

(G–I) Distribution pattern of wild-type and mutant CaMKIIβ.

(J) Formation of mGFP-FIP200 puncta in response to exogenous Ca^{2+} stimulation.

(K and L) SNAP-CaMKIIβ forms puncta after starvation. (L) Shows quantifications of the size (in pixels) and fluorescence intensity of CaMKIIβ puncta (n = 12 puncta from 12 control cells, 1,503 puncta from 12 cells starved for 2.5 h cells, and 4,240 puncta from 20 cells starved for 4 h).

Scale bars: 5 μm (C, D, and J), 2 μm (G–I and K), and 1 μm (I–L and inserts in G–I and K).

See also Figure S2.

CaMKIIβ puncta (Figure S3G) or moved on F-actin (Figure S3H). The CaMKIIβ signal redistributed to filamentous structures after the cells were replenished with nutrients (Figure S3J).

The ER strands intimately interact with F-actin. Accompanied with an elevation of the GCaMP6f-CYB5 signal, SNAP-CaMKIIβ dissociated from filaments and concentrated into puncta in the vicinity of the ER strands (Figure 3A). We detected the following relationships between CaMKIIβ puncta and the ER (Figures 3B–3E). Small CaMKIIβ puncta attached onto and moved with the ER (class I, Figure 3B). The ER underwent remodeling by anchoring on static CaMKIIβ puncta (class II, Figure 3C). The ER strands moved toward and touched on CaMKIIβ puncta (class III, Figure 3D). The majority of CaMKIIβ puncta were separated from the ER strands (class IV, Figure 3E).

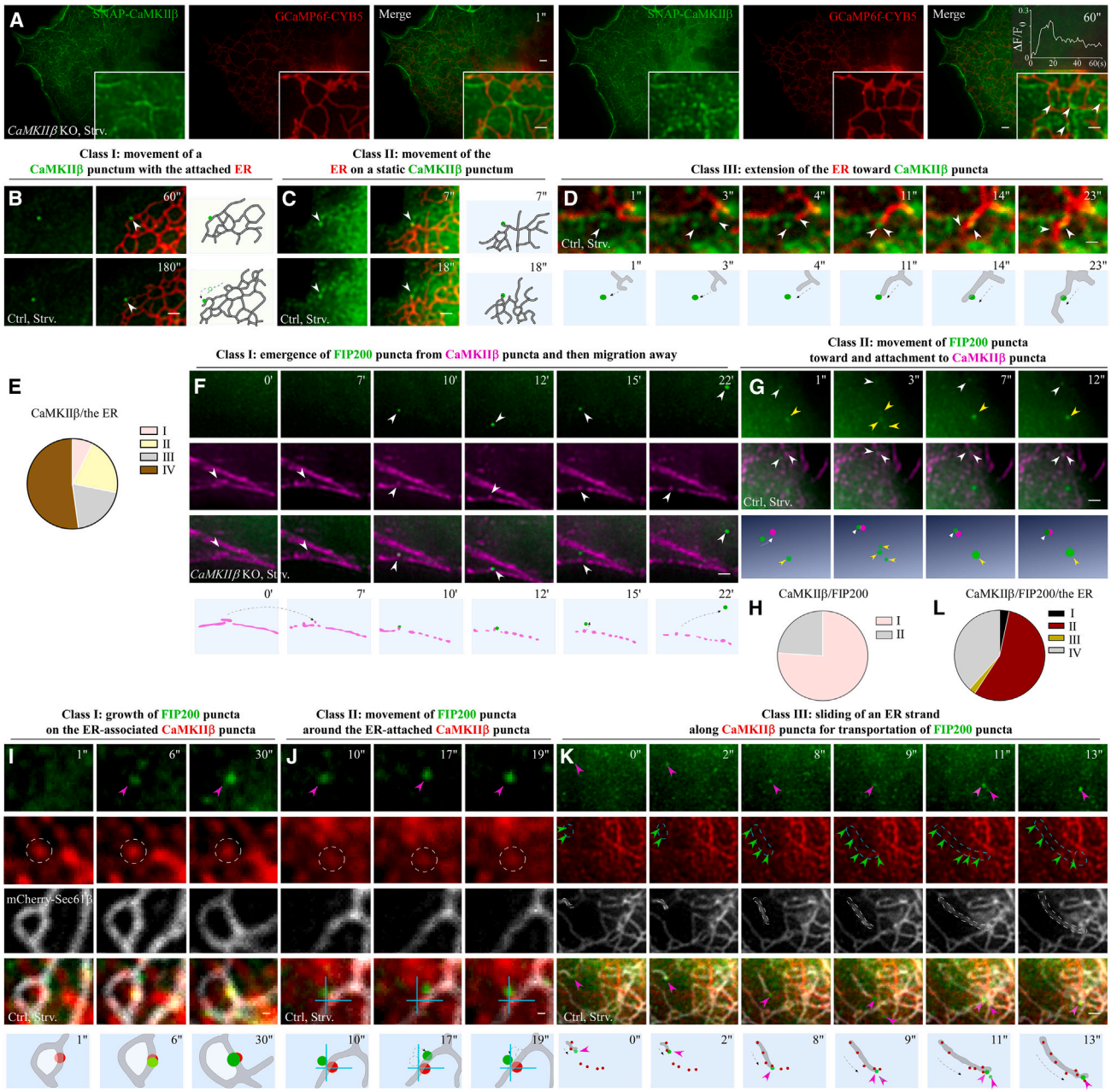

Figure 3. ER Ca^{2+} transients trigger formation of CaMKIIβ puncta

(A) Time-lapse analysis showing that in response to ER Ca^{2+} transients during HBSS starvation, CaMKIIβ forms puncta close to the ER (arrowheads). The normalized GCaMP6f-CYB5 trace is shown in the top right corner of the right panel.

(B–E) CaMKIIβ puncta (arrowheads) show the following relationship with the ER. Class I (B), class II (C), and class III (D) relationships are described on the top of each panel. Class IV refers to separation of CaMKIIβ puncta from the ER. Schematic illustrations of the relationship are also shown in each panel. (E) Shows quantification of the different types of relationship (n = 551 CaMKIIβ puncta from 17 cells).

(F–H) The relationship between CaMKIIβ puncta and FIP200 puncta. Class I and class II relationships are described on the top of (F) and (G), respectively. In (G), fusion of the neighboring FIP200 puncta is indicated by yellow arrowheads. Schematic illustrations are shown underneath. (H) Shows quantification of the relationship shown in (F) and (G). n = 580 CaMKIIβ/FIP200 puncta from 13 cells were analyzed.

(I–L) The relationship between CaMKIIβ puncta/FIP200 puncta and the ER. Classifications for class I, II, and III are described on the top of (I)–(K), respectively. FIP200 puncta are indicated by magenta arrowheads. In (K), the white line outlines an ER strand, and green arrowheads indicate CaMKIIβ puncta. Class IV refers

(legend continued on next page)

In response to exo Ca^{2+} stimulation, SNAP-CaMKIIβ formed a large number of condensates that were largely localized in the cytosol (Figure S3K). These puncta also underwent fusion (Figure S3L). SNAP-CaMKIIβ(T287A or K43R) formed fewer puncta, while CaMKIIβ(T287D) and CaMKIIβ(ΔV1) remained diffuse (Figure S3M). CaMKIIβ puncta were attached to or separated from the F-actin (Figure S3N), and they reformed filamentous structures after exo Ca^{2+} was removed (Figure S3O). Thus, CaMKIIβ reversibly forms puncta in response to Ca^{2+} transients.

The spatiotemporal formation of CaMKIIβ puncta and FIP200 puncta

Time-lapse multi-SIM analysis was performed to reveal the spatiotemporal formation of mGFP-FIP200 and CaMKIIβ puncta. Upon HBSS starvation, small mGFP-FIP200 puncta were formed at the breakage sites in the CaMKIIβ filaments (Figure 3F). The majority of FIP200 puncta were seen emerging adjacent to or on CaMKIIβ puncta, and the intensity of FIP200 then became gradually stronger (Figures 3F and 3H). Some FIP200 puncta also migrated toward and attached to CaMKIIβ puncta (Figure 3G, white arrowhead). The neighboring FIP200 puncta, but not the associated CaMKIIβ puncta, fused to form larger ones (Figure 3G, yellow arrowhead). FIP200 puncta then detached from CaMKIIβ puncta and subsequently reassociated with CaMKIIβ or migrated away (Figure 3F). Co-imaging of CaMKIIβ puncta, FIP200 puncta, and the ER revealed that they displayed the following patterns (Figures 3I–3L and S3P). FIP200 puncta grew on CaMKIIβ puncta, both of which were attached on ER strands (Figure 3I, class I). The FIP200 puncta loosely associated with ER-attached CaMKIIβ puncta (Figure 3J, class II). ER strands attached to FIP200 puncta were able to slide along CaMKIIβ puncta, transporting FIP200 puncta to fuse with remote FIP200 puncta (Figure 3K, class III). FIP200/CaMKIIβ puncta were separate from the ER (Figure S3P, class IV). Only some FIP200 puncta/CaMKIIβ puncta were positive for LC3 (Figures S3Q and S3R). In *FIP200* KO cells, CaMKIIβ still formed puncta (Figure S3S). Our results indicate that CaMKIIβ puncta triggered by ER Ca^{2+} transients dynamically and transiently associate with FIP200 puncta.

In response to exo Ca^{2+} stimulation, FIP200 puncta were formed on the CaMKIIβ filaments, and many of them were formed at the breakage sites in the CaMKIIβ filaments or on the tip of CaMKIIβ puncta (Figure S3T). FIP200 puncta moved around the CaMKIIβ puncta (Figure S3U). Fusion of neighboring FIP200 puncta was detected, while CaMKIIβ remained separate (Figure S3V). FIP200 puncta were able to detach from SNAP-CaMKIIβ puncta, then they reassociated or moved away (Figures S3T–S3V). Thus, ER Ca^{2+} transients or exo Ca^{2+} stimulation result in a similar interaction pattern of CaMKIIβ puncta with FIP200 puncta.

CaMKIIβ-mediated phosphorylation of FIP200 modulates phase separation and organization of FIP200 puncta

In GFP-Trap assays, GFP-FIP200 co-immunoprecipitated FLAG-CaMKIIβ (Figure 4A). FIP200 fragments containing the NTD(1–643), CC1(865–1,232), CC2(1,285–1,396), or Claw(1,396–1,594) were phosphorylated by CaMKIIβ in *in vitro* phosphorylation assays (Figures 4B and S4A). Mass spectrometry analysis of *in vitro*-phosphorylated FIP200 fragments identified that S105, S161, T269, S415, T1127, T1465, and S1484 were phosphorylated by CaMKIIβ (Figures S4B–S4E).

Wild-type FIP200 and FIP200(S105A, S161A, S415A, or T1465A) mutants rescued the formation of WIPI2 puncta and LC3 puncta in *FIP200* KO cells upon starvation (Figures S4G–S4J). FIP200(T269A, T1127A, or S1484A) mutants still interacted with ULK1, ATG13, and ATG101 in co-immunoprecipitation assays (Figure S4F) but showed attenuated rescuing activity (Figures 4C, 4D, and S4G–S4J). FRAP analysis showed no evident difference in the recovery of fluorescence intensity in bleached mGFP-FIP200 puncta and FIP200(T269A, T1127A, or S1484A) mutant puncta triggered by exo Ca^{2+} stimulation or starvation (Figure S4K), suggesting that multiple CaMKIIβ-phosphorylated residues in FIP200 or other components of the FIP200 complex are involved in modulating the material properties of FIP200 puncta. In starved *FIP200* KO cells, FIP200(T269A, T1127A, or S1484A) formed puncta, but the ratio colocalized with WIPI2 puncta was much lower than wild-type FIP200 (Figures S4L–S4P). An antibody specifically recognizing phosphorylated Thr1127 of FIP200 detected no signal in starved *FIP200* KO cells and a much weaker signal in *FIP200* KO cells expressing mGFP-FIP200(T1127A) than expressing wild-type FIP200 (Figure 4E). The signal recognized by anti-pT1127 was reduced in starved *CaMKIIβ* KO cells, supporting the notion that T1127 is phosphorylated by CaMKIIβ (Figure 4F).

We next examined the effect of CaMKIIβ-mediated phosphorylation of FIP200 in assembly of autophagosome formation sites. Upon HBSS starvation, FIP200 puncta were induced and organized into ring-like clusters that were also positive for WIPI2 and LC3 (Figures 4G and 4H). mGFP-FIP200(T269A, T1127A, or S1484A) showed defective organization of autophagosome formation sites. Some mGFP-FIP200(T269A, T1127A, or S1484A)/WIPI2-mCherry puncta failed to proceed from dots into ring-like structures (Figures 4I–4K and 4S). Some of the mGFP-FIP200(T269A, T1127A, or T1484A) puncta underwent extensive fusion, and the resultant larger puncta failed to trigger formation of LC3 structures (Figures 4L–4O). We also observed persistence of FIP200 signal on the WIPI2/LC3 ring structures (Figures 4P–4S). These results indicate that CaMKIIβ-mediated phosphorylation of FIP200 affects the formation of phase-separated puncta and also their organization into functional autophagosome formation sites.

to separation of CaMKIIβ puncta/FIP200 puncta from the ER. Schematic illustrations in (I)–(K) are shown underneath. (L) Shows quantification of the different types of relationship. n = 420 CaMKIIβ/FIP200 puncta/ER from 8 cells were analyzed.

Multi-SIM time-lapse images shown in (B)–(D), (F), (G), and (I)–(K) were collected every second for 30 s. Ratios of the relationship shown in (E), (H), and (L) were analyzed by GraphPad Prism 7.0. Scale bars: 2 μm (A), 1 μm (B, C, F, G, K, and inserts in A), 500 nm (D), and 200 nm (I and J).

See also Figure S3.

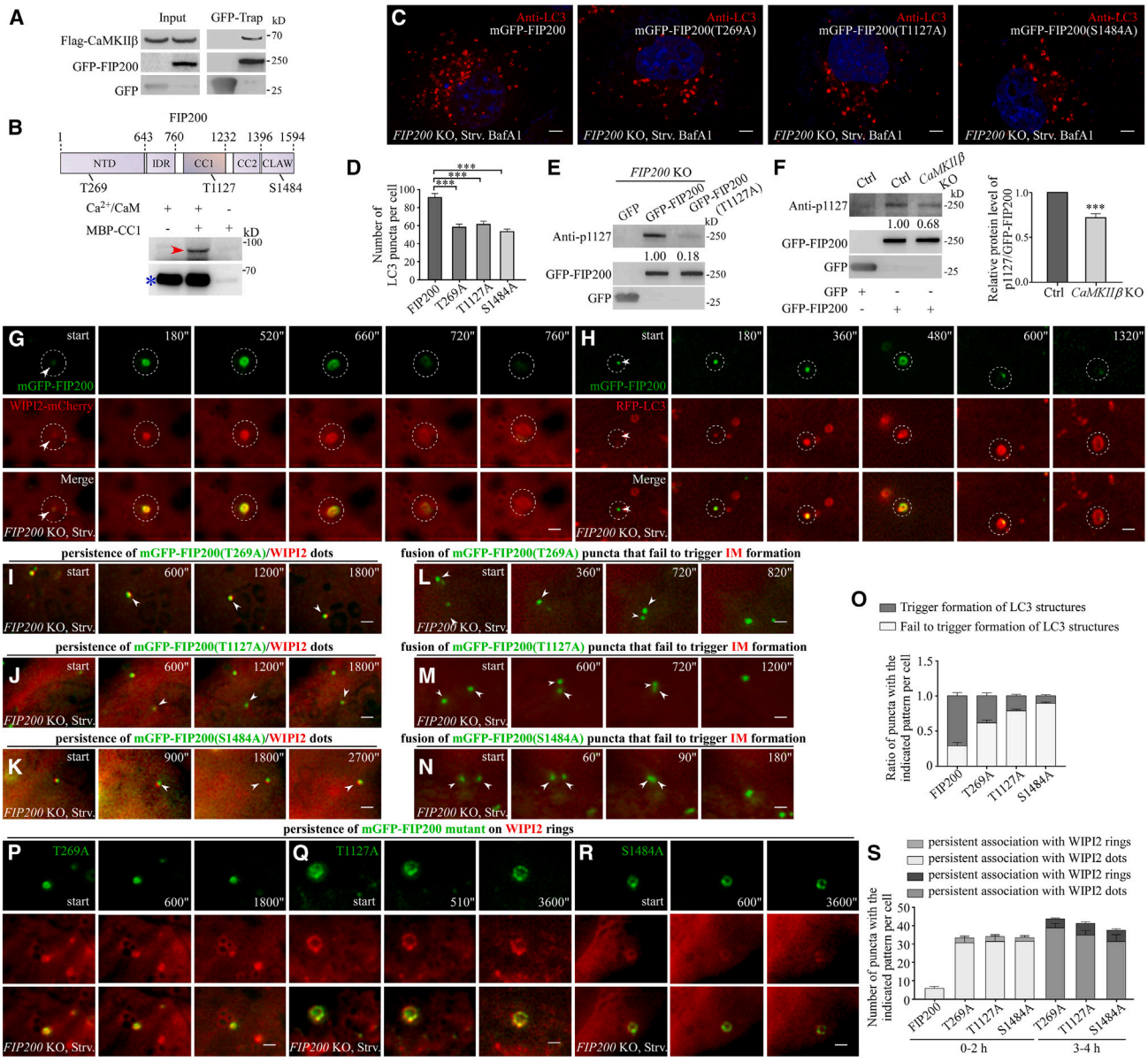

Figure 4. CaMKIIβ-mediated phosphorylation of FIP200 controls phase separation and organization of FIP200 puncta

(A) GFP-FIP200 co-immunoprecipitates FLAG-CaMKIIβ in a GFP-TRAP assay.

(B) Top: schematic illustration of domains in FIP200. Bottom: in *in vitro* phosphorylation assays, purified FIP200-CC1(865–1,232) is phosphorylated by CaMKIIβ (red arrow). The asterisk indicates CaMKIIβ autophosphorylation. The signal is detected by anti-thiophosphate ester antibody. The reaction contains purified CaMKIIβ and ATP-γS.

(C and D) The number of LC3 puncta is lower in cells expressing FIP200(T269A, T1127A, or S1484A) compared with wild-type FIP200. Quantifications are shown in (D) (n = 25, 26, 25, and 29 cells for bars from left to right).

(E) The antibody recognizing phosphorylated Thr1127 of FIP200 detects no signal in starved *FIP200* KO cells. Compared with *FIP200* KO cells expressing mGFP-FIP200, the antibody detects a much weaker signal in cells expressing mGFP-FIP200(T1127A).

(F) Compared with control cells, the anti-p1127 antibody detects a weaker signal in starved *CaMKIIβ* KO cells expressing mGFP-FIP200. Quantifications are shown on the right.

(G and H) Multi-SIM time-lapse imaging of the dynamic changes of FIP200 signal (arrowheads and circles) during formation of autophagic structures labeled by WIPI2 (G) or LC3 (H).

(I–K) mGFP-FIP200(T269A, T1127A, or S1484A)/WIPI2 puncta (arrowheads) do not proceed into ring-like structures during the observation time.

(L–O) mGFP-FIP200(T269A, T1127A, or S1484A) puncta undergo fusion (arrowheads) and fail to induce the formation of LC3 structures. RFP-LC3 shows a diffuse pattern. (O) Shows ratios of the indicated FIP200 puncta that trigger the formation of LC3 structures in starved *FIP200* KO cells (n = 451 FIP200 puncta from 15 cells, 519 FIP200(T269A) puncta from 17 cells, 501 FIP200(T1127A) puncta from 15 cells, and 455 FIP200(S1484A) puncta from 14 cells).

(P–R) mGFP-FIP200(T269A, T1127A, or S1484A)/WIPI2 rings fail to progress into large rings (P) or show persistence of FIP200/WIPI2 (Q and R).

(legend continued on next page)

Phosphomimetic FIP200 promotes assembly of autophagosome formation sites and rescues autophagy defects in CaMKIIβ KO cells

Phosphomimetic FIP200(T269D, T1127D, or S1484D) mutants rescued the autophagy defect in *FIP200* KO cells (Figures 5A–5D and S5A–S5D). The numbers of WIPI2 puncta and LC3 puncta were higher in *FIP200* KO cells expressing FIP200 (T269D, T1127D, or S1484D) compared with wild-type FIP200 (Figures 5A–5D and S5A–S5D). Expression of FIP200(T269D, T1127D, or S1484D), but not wild-type FIP200, induced the formation of WIPI2 puncta and LC3 puncta in control cells under nutrient-rich conditions and further increased their numbers under starvation conditions (Figures S5E–S5L).

Multi-SIM analysis revealed that after HBSS starvation, mGFP-FIP200(T269D, T1127D, or T1484D) formed more puncta and organized ring-like structures than wild-type mGFP-FIP200 (Figures S5M–S5P). mGFP-FIP200(T269D, T1127D, or T1484D) puncta colocalized with WIPI2 puncta from small dots to ring-like structures, and then FIP200 gradually dissociated from the rings (Figures 5E, S5Q, and S5R). Wild-type mGFP-FIP200/WIPI2-mCherry dots were sometimes associated with SNAP-CaMKIIβ puncta, but they separated during the progression of mGFP-FIP200/WIPI2-mCherry into ring structures (Figure 5F), while mGFP-FIP200(T269D, T1127D, or S1484D)/WIPI2-mCherry puncta associated with SNAP-CaMKIIβ puncta during progression of the FIP200/WIPI2-labeled IMs into rings (Figures 5G–5I).

Expressing FIP200(T269D, T1127D, or S1484D), but not wild-type FIP200, also increased the number of WIPI2 puncta and LC3 puncta in *CaMKIIβ* KO cells after starvation (Figures 5J–5M). These results indicate that CaMKIIβ acts in autophagy at least in part by directly phosphorylating FIP200.

Depleting CaMKIIβ attenuates the amplitude, duration, and propagation of ER Ca^{2+} oscillations during autophagy induction

In starved control cells, the ER Ca^{2+} transients occurred at multiple sites that persisted and propagated into larger areas of the ER network (Figures 6A and 6B). In starved *CaMKIIβ* KO cells, local transients were detected, but their amplitude was weaker, and they failed to propagate into larger signals (Figures 6C–6H). Each signal also lasted for a shorter period of time (Figures 6C, 6D, and 6G). In *CaMKIIβ* KO cells, the ER Ca^{2+} store was slightly decreased, while the cytosolic Ca^{2+} was slightly increased (Figures 6I and 6J). The Ca^{2+} baseline on the ER outer surface, detected by the ER-localized ratiometric Ca^{2+} biosensor NEMOf/mTurquoise2-CYB5, was slightly reduced compared with control cells (Figure 6K). HBSS starvation still triggered lysosomal Ca^{2+} release in *CaMKIIβ* KO cells (Figures S6A and S6B), which further induced LLPS of mCherry-FIP200 on lysosomes (Figure S6C). Torin1 treatment-triggered ER Ca^{2+} transients were also greatly attenuated by depletion of *CaMKIIβ* (Figure S6D).

We determined the spatial requirement for CaMKIIβ activity in controlling ER Ca^{2+} transients. The CYB5 ER transmembrane domain-tethered CN21 was used to inhibit CaMKIIβ specifically in the narrow ER-cytosol interface. In cells expressing CN21-CYB5, Ca^{2+} transients on the ER were greatly attenuated upon starvation (Figure 6L). Expressing CN21-CYB5 also inhibited autophagy upon starvation (Figures 6M, 6N, and S6E–S6G). These results indicate that CaMKIIβ acts at the ER-cytosol interface to modulate the sustainability and the spatial propagation of ER Ca^{2+} transients triggered by autophagy stimuli.

Depleting CaMKIIβ attenuates ER Ca^{2+} oscillations in *EI24* KO cells

Ca^{2+} transients persist on the ER outer surface in *EI24* KO cells.[36] Consistent with this, the level of FIP200 phosphorylated at T1127 was increased in *EI24* KO cells compared with control cells (Figure 6O). Simultaneously depleting CaMKIIβ or expressing CN21-CYB5 greatly attenuated the number, amplitude, and duration of Ca^{2+} transients in *EI24* KO cells (Figures 6P, 6Q, and S6H). *CaMKIIβ* KD or expression of CN21-CYB5 reduced the levels of p62 and LC3-II and the accumulation of FIP200 puncta, WIPI2 puncta, and LC3 puncta, and also enlarged the size of LC3 puncta in *EI24* KO cells (Figures 6R, 6T, 6U, and S6I–S6L). TEM analysis showed that *EI24* KO cells accumulated IMs and small unclosed autophagic structures (Figure 6V),[36] while larger and closed autophagosomes were formed by simultaneous depletion of *CaMKIIβ* or expression of CN21-CYB5 (Figures 6S, 6W, and 6X). Thus, the autophagy defect in *EI24* KO cells is ameliorated by attenuating *CaMKIIβ* activity.

Disease-related CaMKIIβ mutations impair autophagy

Mutations in *CaMKIIβ*, including Glu110Lys, Pro139Leu, Glu237Lys, Arg284Ser, and Lys301Glu, have been linked to intellectual disability (ID) (Figure 7A).[14,15,48] The mutations identified in ID locate at the interface of the kinase domain and the autoinhibitory segment (AIS) (Figure 7A). The E110K, P139L, E237K, and R284S mutations cause a partial loss of autoinhibition of kinase activity and increase the phosphorylation of Thr287,[15,48] while the K301E mutation nearly abolishes Thr287 phosphorylation of CaMKIIβ.[15] Autophagy is critical for cognition and memory formation,[49,50] which prompted us to investigate the effect of the disease-related CaMKIIβ mutations on autophagy. Compared with wild-type SNAP-CaMKIIβ, SNAP-CaMKIIβ(P139L, E237K, R284S, and K301E) showed impaired ability to rescue the autophagy defect in starved *CaMKIIβ* KO cells (Figures 7B–7E, S7A, and S7B).

Compared with wild-type CaMKIIβ, CaMKIIβ(E237K) filaments were more evident (Figure 7F), while CaMKIIβ(P139L or R284S) displayed a weaker filamentous pattern (Figures S7C and

(S) Quantifications of persistent association of FIP200 mutants with WIPI2 structures in *FIP200* KO cells during the first 120 min after starvation or 3–4 h after starvation. The number of puncta analyzed for bars from left to right are 251 (from 9 cells), 266 (from 7 cells), 274 (from 7 cells), 234 (from 7 cells), 623 (from 20 cells), 1,304 (from 28 cells), 966 (from 24 cells), and 1,026 (from 28 cells). In FIP200-transfected *FIP200* KO cells, nearly all FIP200/WIP2 dots progressed into rings and then dissociated after starvation for 3–4 h. Multi-SIM images, collected for 60 min at intervals of 30 s, were analyzed.
Scale bars: 5 μm (C) and 1 μm (G–N and P–R).
See also Figure S4.

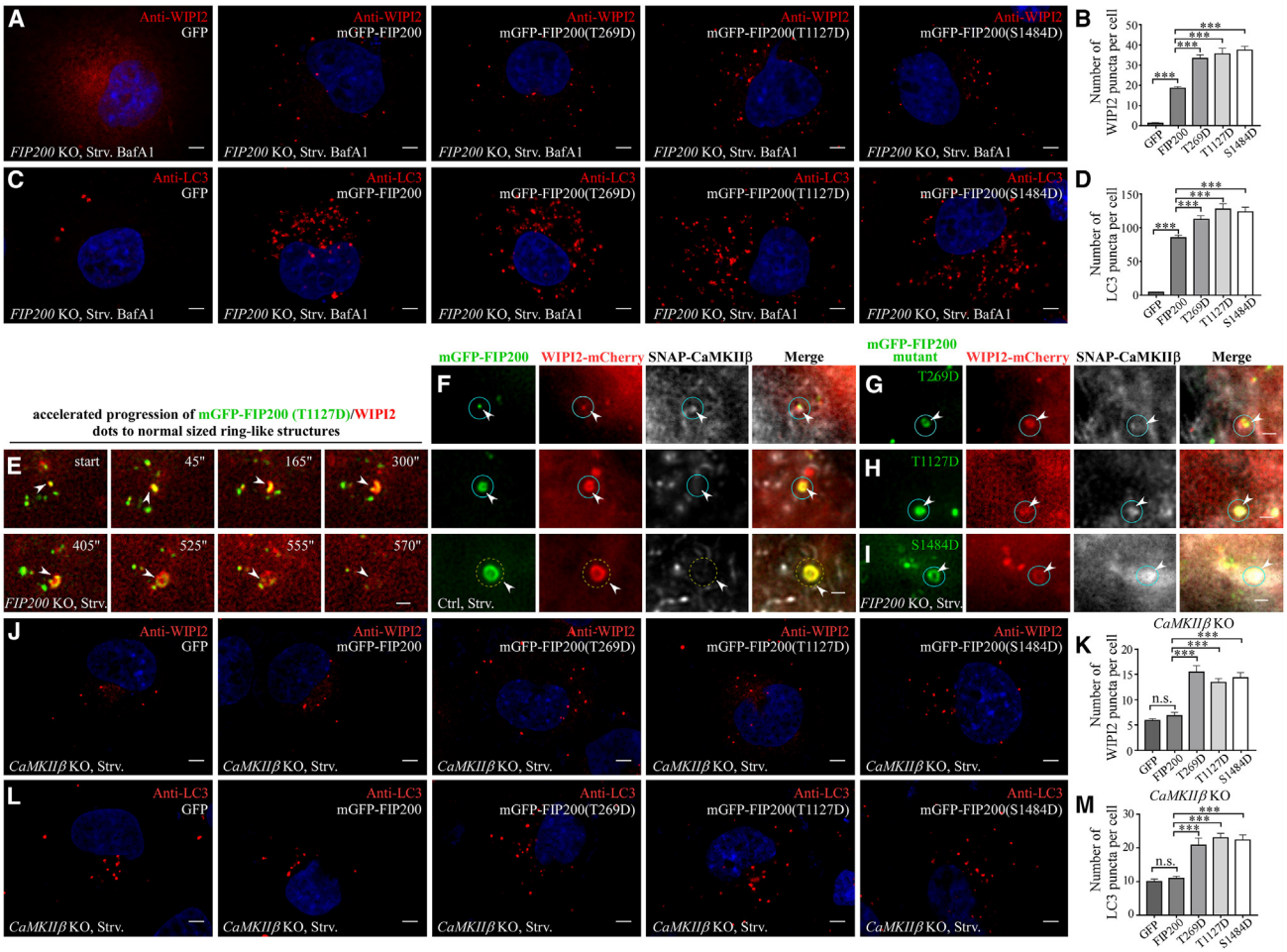

Figure 5. Phosphomimetic FIP200 promotes autophagosome formation and rescues the autophagy defects in *CaMKIIβ* KO cells

(A–D) Phosphomimetic FIP200(T269D, T1127D, or S1484D) mutants rescue the defective formation of WIPI2 puncta (A) and LC3 puncta (C) in BafA1-treated starved *FIP200* KO cells. Quantifications are shown in (B) and (D) (for bars from left to right: $n = 19$, 28, 27, 26, and 30 cells in B; $n = 24$, 31, 29, 27, and 31 cells in D).

(E) Time-lapse analysis of the progression of mGFP-FIP200(T1127D)/WIPI2-mCherry dots (arrowheads) into ring structures and their dissociation from the rings.

(F–I) In starved control cells, mGFP-FIP200/WIPI2-mCherry dots are associated with SNAP-CaMKIIβ puncta (blue circles and arrowheads) and become dissociated during progression into ring structures (dashed yellow circles) (F), while mGFP-FIP200(T269D, T1127D, or S1484D)/WIPI2-mCherry (blue circles) show persistent association with SNAP-CaMKIIβ puncta (G–I).

(J–M) Compared with wild-type FIP200, expression of FIP200(T269D, T1127D, or S1484D) causes formation of more WIPI2 puncta and LC3 puncta in *CaMKIIβ* KO cells. Quantifications are shown in (K) and (M) (for bars from left to right: $n = 28$, 23, 24, 22, and 24 cells in K and $n = 28$, 24, 22, 23, and 22 cells in M).

Scale bars: 5 μm (A, C, J, and L) and 1 μm (E–I).

See also Figure S5.

S7D). CaMKIIβ(K301E) was diffuse in the cytosol (Figure 7G). Upon starvation, CaMKIIβ(E237K) formed fewer puncta (Figure 7F). CaMKIIβ(P139L, R284S, or K301E) formed more large-sized puncta than control CaMKIIβ (Figures 7G and S7C–S7E). The few CaMKIIβ(E237K) puncta still showed interaction with FIP200/WIPI2 puncta (Figures S7F and S7G). However, the large puncta formed by CaMKIIβ(P139L, R284S, or K301E) exhibited no association with FIP200/WIPI2 puncta (Figures 7H, S7H, and S7I). In CaMKIIβ(R284S or K301E)-expressing cells, FIP200/WIPI2 failed to organize into ring-like structures and/or persisted on the ring structures (Figures 7I, S7J, and S7K).

The CaMKIIβ(E110K) mutant shows a significant increase in autophosphorylation at Thr287.[15] SNAP-CaMKIIβ(E110K) was diffuse in the cytosol and failed to form puncta upon starvation (Figure 7J). In CaMKIIβ(E110K)-expressing cells, FIP200 puncta/WIPI2 puncta organized into small ring structures in *CaMKIIβ* KO cells (Figure 7K). High-level expression of SNAP-CaMKIIβ(E110K) caused accumulation of small-sized yellow RFP-GFP-LC3 puncta in control cells (Figures S7L and S7M). Cells expressing CaMKIIβ(E110K) exhibited persistent Ca^{2+} signals, such as long-lasting regional ER transients (Figure 7L). This phenotype resembles *EI24* KO cells.[36] Thus, disease-related CaMKIIβ mutants exhibit differences in the formation of starvation-induced puncta and in triggering the formation of FIP200-labeled autophagosome formation sites.

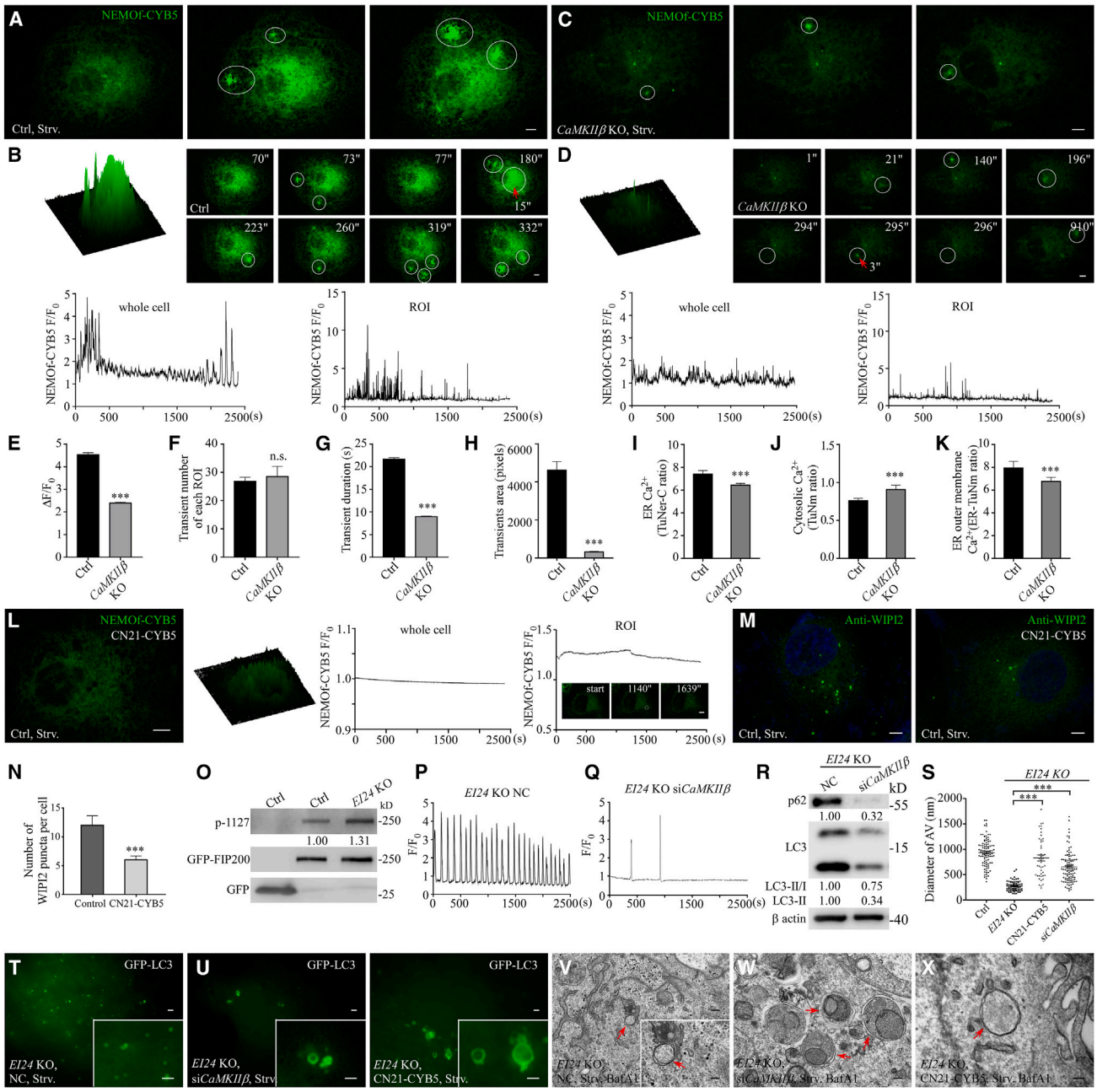

Figure 6. Depleting CaMKIIβ attenuates the amplitude, duration, and propagation of ER Ca^{2+} oscillations during autophagy induction

(A–D) The ER Ca^{2+} transients in starved control cells (A and B) and *CaMKIIβ* KO cells (C and D). White circles indicate examples of regional transients (ROI). A 3D surface plot of one transient is shown in (B, top left) and (D, top left). The trace diagrams (bottom in B and D) show dynamic fluorescence changes in the whole cell or in a selected area. Images showing dynamic fluorescence signals are also presented (top right in B and D). The duration time for the indicated transient (red arrows) is also specified.

(E–H) Quantifications of amplitude, frequency, duration, and areas of ER Ca^{2+} transients in control cells (n = 3,018 transients) and *CaMKIIβ* KO cells (n = 3,043 transients).

(I and J) The ER Ca^{2+} store is reduced, while the cytosolic Ca^{2+} is increased in *CaMKIIβ* KO cells (n = 44 cells for control, n = 63 cells for *CaMKIIβ* KO in I, n = 21 cells for control, and n = 21 cells for *CaMKIIβ* KO in J).

(K) The Ca^{2+} baseline on the ER outer surface is reduced in *CaMKIIβ* KO cells compared with control cells (n = 34 and 50 cells for control and *CaMKIIβ* KO, respectively).

(L) In cells expressing CN21-CYB5, ER Ca^{2+} transients are attenuated upon starvation. The trace diagrams show fluorescence changes in the whole cell or in the ROI (dashed circle).

(legend continued on next page)

DISCUSSION

CaMKIIβ controls LLPS of the FIP200 complex and organization of FIP200 puncta into autophagosome formation sites

Here, we showed that CaMKIIβ transduces the ER Ca^{2+} transient for the assembly of FIP200 puncta. CaMKIIβ directly phosphorylates FIP200 to promote its LLPS. Protein phosphorylation, which affects the valency and strength of protein-protein interactions, is a widely employed mechanism to modulate phase separation and transition.[51–55] In *CaMKIIβ* KO cells, formation of FIP200 puncta is greatly reduced. The remaining FIP200 puncta may be induced by the abundant local ER Ca^{2+} transients and lysosomal Ca^{2+} release. CaMKIIβ also specifies the organization of FIP200 puncta into functional autophagosome formation sites. FIP200 puncta in *CaMKIIβ* KO cells still trigger the formation of WIPI2-labeled IMs, while their progression into closed autophagosomes is impaired (Figure 7M). CaMKIIβ-mediated phosphorylation of FIP200 may modulate its interaction with the ER or downstream-acting autophagy proteins or regulate the material properties of FIP200 puncta, thereby affecting their behaviors. CaMKIIβ may also phosphorylate other autophagy proteins that control IM expansion and closure. Autophagy activity is partially retained in *CaMKIIβ* KO cells. Other Ca^{2+}-responsive kinases may modify components of the FIP200 complex in CaMKIIβ-depleted cells. Moreover, unclosed autophagosomes are still able to fuse with lysosomes, although at a reduced rate.[56]

CaMKIIα responds to changes in the cytosolic Ca^{2+} level to modulate the autophagy level in a context-dependent manner.[57–59] For example, CaMKIIα phosphorylates Beclin 1 at Ser90 to increase autophagy,[57] or at Ser295 to inhibit autophagy.[58] CaMKIIα and CaMKIIβ, which exhibit distinct enzymatic kinetics and affinities for CaM,[8,60] can co-assemble into heteromeric holoenzymes. The α/β subunit ratio of CaMKII holoenzymes specifies synaptic strength.[10,61,62] Depleting CaMKIIα increases the number of LC3 puncta, which could be in part due to a concomitant increase in CaMKIIβ-containing holoenzymes. CaMKI and CaMKIV, members of the multifunctional CaMK family, also regulate autophagy in response to alterations of the cytosolic Ca^{2+} level.[63–66] Distinct from these CaMKs, CaMKIIβ is essential for autophagosome formation.

The actin-binding activity of CaMKIIβ is critical for autophagosome formation

CaMKIIβ binds to and bundles F-actin.[67] The dynamic CaMKIIβ-F-actin association in response to synaptic Ca^{2+} influx during LTP (long-term potentiation) allows actin reorganization in the spine and thus gates synaptic plasticity.[4,46,47] Here, we showed that in response to ER Ca^{2+} transients, the F-actin-associated CaMKIIβ filaments break up in places, and CaMKIIβ puncta appear at these sites. The actin-bound CaMKIIβ is auto-inhibited.[68] The ER Ca^{2+} transient-triggered CaMKIIβ puncta, which presumably contain active CaMKIIβ, provide a local environment to promote FIP200 phosphorylation, thus facilitating LLPS of FIP200. Actin filaments intimately associate with ER tubules.[69] ER Ca^{2+} transients triggered by autophagy stimuli propagate into a very short range from the outer surface due to the presence of Ca^{2+}-binding proteins and SERCA pumps that export Ca^{2+} from the cytosol to the ER lumen. The F-actin-bound CaMKIIβ that aligns adjacent to the ER provides a local concentrated pool of CaMKIIβ and also acts as a scaffold for formation of FIP200 puncta, ensuring a quick response to fast and spatially restricted local Ca^{2+} signals.

High-level expression of the constitutively active CaMKIIβ(T287D) inhibits formation of FIP200 puncta. The high level of CaMKIIβ(T287D) may cause ectopic or hyper-phosphorylation of autophagy proteins. For example, phosphorylation of ULK1 at some residues inhibits autophagy.[70] The actin-binding activity of CaMKIIβ serves as a mechanism to control the kinase activity and subsequently the phosphorylation level of FIP200 or other components to ensure the level of autophagy induction corresponds to the level of the stimulus.

CaMKIIβ regulates the properties of autophagy stimulus-triggered ER Ca^{2+} transients

CaMKIIβ acts at the ER-cytosol interface to sustain and propagate ER Ca^{2+} transients. In *CaMKIIβ* KO cells, ER Ca^{2+} transients are still induced by autophagy stimuli, but the duration of each transient is shortened, and the signals fail to propagate into larger signals. CaMKIIδ has been shown to phosphorylate IP3R2 and RyR2 to regulate channel open probability,[41,42,71] and phospholamban to release its inhibition on SERCA2.[72] CaMKIIβ may also phosphorylate ER-localized Ca^{2+} channels, pumps, and/or their binding proteins to sustain ER Ca^{2+} transients. The formation of FIP200 puncta is attenuated by exo Ca^{2+} stimulus in *CaMKIIβ* KO cells, indicating that CaMKIIβ controls LLPS of the FIP200 complex independently of its role in modulating the ER transients.

The properties of CaMKII (e.g., dual requirement of Ca^{2+}-CaM for CaMKII autophosphorylation) and the action of phosphatases ensure that CaMKII autophosphorylation occurs in a switch-like fashion over a narrow range of Ca^{2+} concentrations.[73]

(M and N) Compared with control cells, the number of WIPI2 puncta is reduced in cells expressing CN21-CYB5 under starvation conditions. (N) Shows quantifications (n = 24 for control and n = 24 for cells expressing CN21-CYB5).
(O) The level of FIP200 with phosphorylated T1127 is increased in starved *EI24* KO cells compared with control cells.
(P and Q) Compared with Ca^{2+} transients in *EI24* KO cells, the number and amplitude of Ca^{2+} transients are attenuated by simultaneously depleting CaMKIIβ.
(R) Levels of p62 and LC3-II in *EI24* KO cells are reduced by *CaMKIIβ* KD.
(S) Column scatter chart shows the size of AVs/unclosed AVs revealed by TEM analysis in the indicated cells. Data for control cells are the same as in Figure 1L.
(T and U) Multi-SIM imaging reveals that starved *EI24* KO cells accumulate small GFP-LC3 structures (T), while depletion of *CaMKIIβ* or expression of mCherry-CN21-CYB5 (U) causes formation of large LC3 ring structures in *EI24* KO cells.
(V–X) TEM images of autophagic structures in BafA1-treated starved *EI24* KO cells and also in *EI24* KO cells with depletion of *CaMKIIβ* or expression of CYB5-CN21.
Scale bars: 5 μm (A–D, L, and M), 2 μm (T and U), 1 μm (inserts in T and U), 200 nm (V–X), and 100 nm (insert in V).
See also Figure S6.

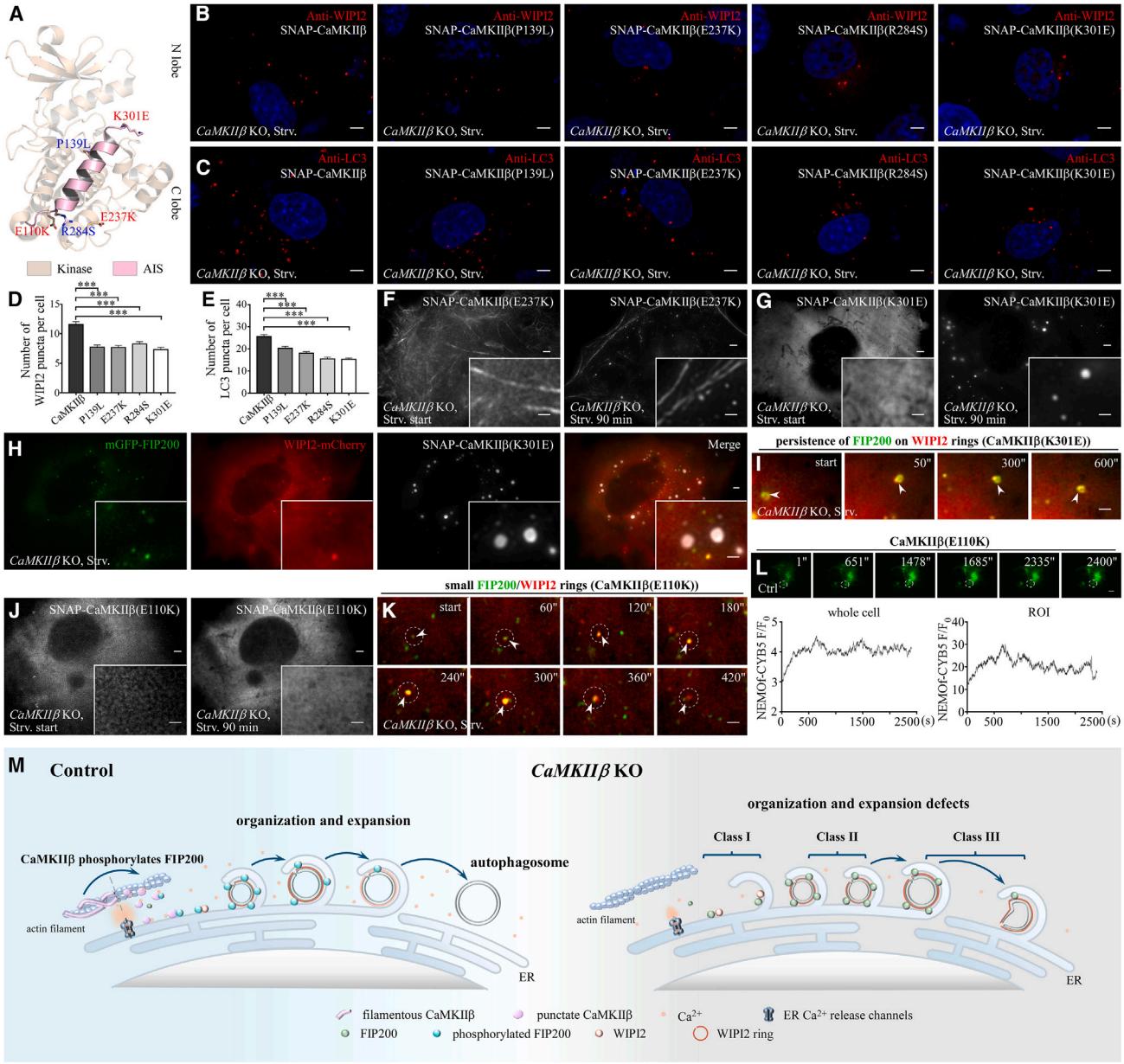

Figure 7. Disease-related CaMKIIβ mutations impair autophagy

(A) Crystal structure of the kinase domain and AIS of CaMKIIβ (PDB: 3BHH). The disease-associated mutations of CaMKIIβ are specified.

(B–E) Compared with wild-type CaMKIIβ, CaMKIIβ(P139L, E237K, R284S, or K301E) show impaired ability to rescue the number of WIPI2 puncta (B) and LC3 puncta (C) in starved *CaMKIIβ* KO cells. Quantifications are shown in (D) and (E) (for bars from left to right: $n = 45, 62, 56, 53$, and 53 cells in D and $n = 23, 26, 31, 22$, and 31 cells in E).

(F) CaMKIIβ(E237K) displays a filamentous pattern under nutrient-rich conditions and forms a few puncta upon starvation.

(G) SNAP-CaMKIIβ(K301E) forms numerous puncta under starvation conditions.

(H) The enlarged SNAP-CaMKIIβ(K301E) puncta show no association with FIP200/WIPI2 puncta.

(I) Persistence of FIP200/WIPI2 signals (arrowheads) in the small ring structures in *CaMKIIβ* KO cells expressing SNAP-CaMKIIβ(K301E).

(J) When expressed at a low level, CaMKIIβ(E110K) exhibits a diffuse pattern.

(K) FIP200/WIPI2 form small ring structures in starved *CaMKIIβ* KO cells expressing CaMKIIβ(E110K).

(L) In starved control cells expressing CaMKIIβ(E110K), the NEMOf-CYB5 signal indicates the presence of long-lasting regional ER Ca^{2+} transients (indicated by circles). Other types of Ca^{2+} transients, such as Ca^{2+} oscillations, are also detected. The trace diagrams show dynamic fluorescence changes (ROI is indicated by the dashed circle).

(legend continued on next page)

Phosphatases may act coordinately with CaMKIIβ to ensure that CaMKIIβ activity drives LLPS of the FIP200 complex only when the combined properties of Ca^{2+} transients reach a certain degree, while stochastic ER Ca^{2+} transients are buffered, preventing the FIP200 complex from generating futile puncta.

In yeast, autophagosomes are formed on the vacuolar membrane.[74] The vacuole (not the ER) is the Ca^{2+} storage organelle.[75] Whether LLPS of the Atg1 complex is triggered by vacuolar Ca^{2+} release remains unknown. Homologs of CaMKIIβ are absent in yeast. Nevertheless, LLPS of the autophagy-initiating Atg1 complex in yeast is also controlled by its phosphorylation level.[76] Unlike the constitutively formed FIP200/ULK1 complex in mammalian cells,[77] formation of yeast Atg1 complex is triggered by starvation or TORC1 (target of rapamycin complex 1) inhibition-mediated dephosphorylation of Atg13.[78,79] The Atg1 condensates driven by LLPS are tethered to the vacuolar membrane to organize the autophagosome assembly site.[74,80]

CaMKIIβ mutations identified in ID impair autophagy

Autophagy regulates neuronal development and functions, such as memory formation, erasure, and learning.[49,50,81,82] For example, autophagy promotes structural and functional synaptic plasticity, including dendritic spine formation, synaptic strength, and LTP.[49] Long-term depression (LTD)-inducing activity triggers autophagy in the dendrites of postsynaptic excitatory neurons to degrade postsynaptic components.[50] Loss of function of the autophagy gene *WDR45b* causes ID in humans and also impairs learning and memory in mouse models.[83,84]

Mutations in *CaMKIIβ* have been identified in patients with the neurodevelopmental disorder MRD54, which is characterized by delayed psychomotor development and ID.[8,14,15,48] We found that disease-related mutations in CaMKIIβ exert differential effects on CaMKIIβ phase separation and ER Ca^{2+} transients. Compared with wild-type CaMKIIβ, CaMKIIβ(E237K) displays a more evident filamentous pattern, while CaMKIIβ(P139L, R284S, or K301E) are more diffuse in the cytosol. Upon starvation, mutant CaMKIIβ forms fewer or larger puncta that are not associated with FIP200/WIPI2 puncta. Thus, CaMKIIβ mutants behave as partial loss-of-function mutations in autophagosome formation. The E110K mutant is diffusely localized and causes more dynamic ER Ca^{2+} transients and the formation of small unacidified autophagosomes, a phenotype known to be associated with persistent ER Ca^{2+} transients.[36] Our findings indicate that dysregulated autophagy is a commonly shared defect in these disease-related CaMKIIβ mutants. Impairment of autophagy caused by CaMKIIβ mutation may be a major driver for disease pathogenesis.

Limitations of the study

Although we demonstrated that CaMKIIβ transduces the ER Ca^{2+} transients to initiate autophagosome formation, it remains technically challenging to determine the frequency and amplitude of local Ca^{2+} transients sensed by CaMKIIβ. The ER Ca^{2+} transients are specified by the combinatory action of channels, pumps, and interacting proteins. The mechanism by which CaMKIIβ maintains the Ca^{2+} transients during autophagy induction has yet to be determined. In *CaMKIIβ* KO cells, the autophagic flux is not completely blocked. Other machineries may be employed to decode ER Ca^{2+} transients, and this requires future investigations.

RESOURCE AVAILABILITY

Lead contact

Further information and requests for resources and reagents should be directed to and will be fulfilled by the lead contact, Hong Zhang (hongzhang@ibp.ac.cn).

Materials availability

Plasmids and other reagents generated in this study are available from the lead contact with a completed Materials Transfer Agreement.

Data and code availability

- Original western blot and microscopy images have been deposited at Mendeley and are publicly available as of the date of publication: https://www.doi.org/10.17632/vhtn5s5dbx.1.
- This paper does not report original code.
- Any additional information required to reanalyze the data reported in this paper is available from the lead contact upon request.

ACKNOWLEDGMENTS

We are grateful to Dr. Isabel Hanson for editing work, and Mr. Jifeng Wang from the Laboratory of Proteomics, IBP, for MS analysis, and Mr. Shihan Zhu from Southern University of Science and Technology for providing purified CaMKIIβ protein. This work was supported by the National Natural Science Foundation of China (grant 82188101 to Hong Zhang, and grant 32322038 to Qiaoxia Zheng) and the New Cornerstone Science Foundation to Hong Zhang.

AUTHOR CONTRIBUTIONS

Hong Zhang, Mingjie Zhang, Tingting Li, Youjun Wang, and Qiaoxia Zheng designed the experiments. Qiaoxia Zheng, Huan Zhang, Hongyu Zhao, Yong Chen, Hongzhining Yang, Qixu Cai, and Yingyu Chen conducted the experiments. Qiaoxia Zheng and Hong Zhang wrote the manuscript.

DECLARATION OF INTERESTS

The authors declare no competing interests.

STAR★METHODS

Detailed methods are provided in the online version of this paper and include the following:

- KEY RESOURCES TABLE
- EXPERIMENTAL MODEL AND STUDY PARTICIPANT DETAILS
  - Cell lines

(M) Model for the role of CaMKIIβ in transducing ER Ca^{2+} transients to autophagosome formation. Under normal conditions, CaMKIIβ associates with actin filaments that intimately interact with the ER. In response to ER Ca^{2+} transients, CaMKIIβ forms distinct puncta, which mediate phosphorylation of FIP200 to modulate formation of FIP200 puncta. FIP200 puncta then associate with the ER to trigger autophagosome formation. In *CaMKIIβ* KO cells, FIP200 puncta are fewer in number and are defective in organizing into functional autophagosome formation sites. The FIP200/WIPI2 structures remain as dots (class I defect), or progress into small rings (class II defect) or enlarged irregular structures (class III defect).
Scale bars: 5 μm (B, C, and L), 2 μm (F–H and J), and 1 μm (I, K, and inserts in F–H and J).
See also Figure S7.

SUPPLEMENTAL INFORMATION

Supplemental information can be found online at https://doi.org/10.1016/j.molcel.2024.12.005.

Received: May 1, 2024
Revised: September 16, 2024
Accepted: December 6, 2024
Published: December 31, 2024

REFERENCES

1. Berridge, M.J., Lipp, P., and Bootman, M.D. (2000). The versatility and universality of calcium signalling. Nat. Rev. Mol. Cell Biol. *1*, 11–21. https://doi.org/10.1038/35036035.
2. Sammels, E., Parys, J.B., Missiaen, L., De Smedt, H., and Bultynck, G. (2010). Intracellular Ca^{2+} storage in health and disease: a dynamic equilibrium. Cell Calcium *47*, 297–314. https://doi.org/10.1016/j.ceca.2010.02.001.
3. Bredow, M., and Monaghan, J. (2022). Cross-kingdom regulation of calcium- and/or calmodulin-dependent protein kinases by phospho-switches that relieve autoinhibition. Curr. Opin. Plant Biol. *68*, 102251. https://doi.org/10.1016/j.pbi.2022.102251.
4. Takemoto-Kimura, S., Suzuki, K., Horigane, S.I., Kamijo, S., Inoue, M., Sakamoto, M., Fujii, H., and Bito, H. (2017). Calmodulin kinases: essential regulators in health and disease. J. Neurochem. *141*, 808–818. https://doi.org/10.1111/jnc.14020.
5. Bootman, M.D., and Bultynck, G. (2020). Fundamentals of cellular calcium signaling: a primer. Cold Spring Harb. Perspect. Biol. *12*, a038802. https://doi.org/10.1101/cshperspect.a038802.
6. Dupont, G., and Goldbeter, A. (1998). CaM kinase II as frequency decoder of Ca^{2+} oscillations. BioEssays *20*, 607–610. https://doi.org/10.1002/(SICI)1521-1878(199808)20:8<607::AID-BIES2>3.0.CO;2-F.
7. De Koninck, P., and Schulman, H. (1998). Sensitivity of CaM kinase II to the frequency of Ca2+ oscillations. Science *279*, 227–230. https://doi.org/10.1126/science.279.5348.227.
8. Yasuda, R., Hayashi, Y., and Hell, J.W. (2022). CaMKII: a central molecular organizer of synaptic plasticity, learning and memory. Nat. Rev. Neurosci. *23*, 666–682. https://doi.org/10.1038/s41583-022-00624-2.
9. Hudmon, A., and Schulman, H. (2002). Structure-function of the multifunctional Ca^{2+}/calmodulin-dependent protein kinase II. Biochem. J. *364*, 593–611. https://doi.org/10.1042/BJ20020228.
10. Rostas, J.A.P., and Skelding, K.A. (2023). Calcium/Calmodulin-Stimulated Protein Kinase II (CaMKII): Different Functional Outcomes from Activation, Depending on the Cellular Microenvironment. Cells *12*, 401. https://doi.org/10.3390/cells12030401.
11. Stratton, M.M., Chao, L.H., Schulman, H., and Kuriyan, J. (2013). Structural studies on the regulation of Ca2+/calmodulin dependent protein kinase II. Curr. Opin. Struct. Biol. *23*, 292–301. https://doi.org/10.1016/j.sbi.2013.04.002.
12. Ishida, A., Sueyoshi, N., Shigeri, Y., and Kameshita, I. (2008). Negative regulation of multifunctional Ca^{2+}/calmodulin-dependent protein kinases: physiological and pharmacological significance of protein phosphatases. Br. J. Pharmacol. *154*, 729–740. https://doi.org/10.1038/bjp.2008.127.
13. Tullis, J.E., Larsen, M.E., Rumian, N.L., Freund, R.K., Boxer, E.E., Brown, C.N., Coultrap, S.J., Schulman, H., Aoto, J., Dell'Acqua, M.L., et al. (2023). LTP induction by structural rather than enzymatic functions of CaMKII. Nature *621*, 146–153. https://doi.org/10.1038/s41586-023-06465-y.
14. Borghi, R., Trivisano, M., Specchio, N., Tartaglia, M., and Compagnucci, C. (2023). Understanding the pathogenetic mechanisms underlying altered neuronal function associated with CAMK2B mutations. Neurosci. Biobehav. Rev. *152*, 105299. https://doi.org/10.1016/j.neubiorev.2023.105299.
15. Küry, S., van Woerden, G.M., Besnard, T., Proietti Onori, M.P., Latypova, X., Towne, M.C., Cho, M.T., Prescott, T.E., Ploeg, M.A., Sanders, S., et al. (2017). De Novo Mutations in Protein Kinase Genes CAMK2A and CAMK2B Cause Intellectual Disability. Am. J. Hum. Genet. *101*, 768–788. https://doi.org/10.1016/j.ajhg.2017.10.003.
16. Li, K., Zhou, T., Liao, L., Yang, Z., Wong, C., Henn, F., Malinow, R., Yates, J.R., 3rd, and Hu, H. (2013). βCaMKII in lateral habenula mediates core symptoms of depression. Science *341*, 1016–1020. https://doi.org/10.1126/science.1240729.
17. Nicole, O., and Pacary, E. (2020). CaMKIIβ in Neuronal Development and Plasticity: An Emerging Candidate in Brain Diseases. Int. J. Mol. Sci. *21*, 7272. https://doi.org/10.3390/ijms21197272.
18. Lamb, C.A., Yoshimori, T., and Tooze, S.A. (2013). The autophagosome: origins unknown, biogenesis complex. Nat. Rev. Mol. Cell Biol. *14*, 759–774. https://doi.org/10.1038/nrm3696.
19. Nakatogawa, H. (2020). Mechanisms governing autophagosome biogenesis. Nat. Rev. Mol. Cell Biol. *21*, 439–458. https://doi.org/10.1038/s41580-020-0241-0.
20. Vargas, J.N.S., Hamasaki, M., Kawabata, T., Youle, R.J., and Yoshimori, T. (2023). The mechanisms and roles of selective autophagy in mammals. Nat. Rev. Mol. Cell Biol. *24*, 167–185. https://doi.org/10.1038/s41580-022-00542-2.
21. Zhao, Y.G., Codogno, P., and Zhang, H. (2021). Machinery, regulation and pathophysiological implications of autophagosome maturation. Nat. Rev. Mol. Cell Biol. *22*, 733–750. https://doi.org/10.1038/s41580-021-00392-4.
22. Mizushima, N., and Komatsu, M. (2011). Autophagy: renovation of cells and tissues. Cell *147*, 728–741. https://doi.org/10.1016/j.cell.2011.10.026.
23. Morishita, H., and Mizushima, N. (2019). Diverse Cellular Roles of Autophagy. Annu. Rev. Cell Dev. Biol. *35*, 453–475. https://doi.org/10.1146/annurev-cellbio-100818-125300.
24. Deretic, V. (2021). Autophagy in inflammation, infection, and immunometabolism. Immunity *54*, 437–453. https://doi.org/10.1016/j.immuni.2021.01.018.
25. Dikic, I., and Elazar, Z. (2018). Mechanism and medical implications of mammalian autophagy. Nat. Rev. Mol. Cell Biol. *19*, 349–364. https://doi.org/10.1038/s41580-018-0003-4.
26. Yamamoto, H., Zhang, S., and Mizushima, N. (2023). Autophagy genes in biology and disease. Nat. Rev. Genet. *24*, 382–400. https://doi.org/10.1038/s41576-022-00562-w.

27. Gómez-Sánchez, R., Tooze, S.A., and Reggiori, F. (2021). Membrane supply and remodeling during autophagosome biogenesis. Curr. Opin. Cell Biol. *71*, 112–119. https://doi.org/10.1016/j.ceb.2021.02.001.

28. Ktistakis, N.T., and Tooze, S.A. (2016). Digesting the Expanding Mechanisms of Autophagy. Trends Cell Biol. *26*, 624–635. https://doi.org/10.1016/j.tcb.2016.03.006.

29. Mizushima, N. (2020). The ATG conjugation systems in autophagy. Curr. Opin. Cell Biol. *63*, 1–10. https://doi.org/10.1016/j.ceb.2019.12.001.

30. Ohsumi, Y. (2014). Historical landmarks of autophagy research. Cell Res. *24*, 9–23. https://doi.org/10.1038/cr.2013.169.

31. Zhang, H. (2022). The genetics of autophagy in multicellular organisms. Annu. Rev. Genet. *56*, 17–39. https://doi.org/10.1146/annurev-genet-022422-095608.

32. Karanasios, E., Walker, S.A., Okkenhaug, H., Manifava, M., Hummel, E., Zimmermann, H., Ahmed, Q., Domart, M.C., Collinson, L., and Ktistakis, N.T. (2016). Autophagy initiation by ULK complex assembly on ER tubulovesicular regions marked by ATG9 vesicles. Nat. Commun. *7*, 12420. https://doi.org/10.1038/ncomms12420.

33. Orsi, A., Razi, M., Dooley, H.C., Robinson, D., Weston, A.E., Collinson, L.M., and Tooze, S.A. (2012). Dynamic and transient interactions of Atg9 with autophagosomes, but not membrane integration, are required for autophagy. Mol. Biol. Cell *23*, 1860–1873. https://doi.org/10.1091/mbc.E11-09-0746.

34. Axe, E.L., Walker, S.A., Manifava, M., Chandra, P., Roderick, H.L., Habermann, A., Griffiths, G., and Ktistakis, N.T. (2008). Autophagosome formation from membrane compartments enriched in phosphatidylinositol 3-phosphate and dynamically connected to the endoplasmic reticulum. J. Cell Biol. *182*, 685–701. https://doi.org/10.1083/jcb.200803137.

35. Karanasios, E., Stapleton, E., Manifava, M., Kaizuka, T., Mizushima, N., Walker, S.A., and Ktistakis, N.T. (2013). Dynamic association of the ULK1 complex with omegasomes during autophagy induction. J. Cell Sci. *126*, 5224–5238. https://doi.org/10.1242/jcs.132415.

36. Zheng, Q.X., Chen, Y., Chen, D., Zhao, H.Y., Feng, Y., Meng, Q., Zhao, Y., and Zhang, H. (2022). Calcium transients on the ER surface trigger liquid-liquid phase separation of FIP200 to specify autophagosome initiation sites. Cell *185*, 4082–4098.e22. https://doi.org/10.1016/j.cell.2022.09.001.

37. Decuypere, J.P., Welkenhuyzen, K., Luyten, T., Ponsaerts, R., Dewaele, M., Molgó, J., Agostinis, P., Missiaen, L., De Smedt, H., Parys, J.B., et al. (2011). Ins(1,4,5)P3 receptor-mediated Ca2+ signaling and autophagy induction are interrelated. Autophagy *7*, 1472–1489. https://doi.org/10.4161/auto.7.12.17909.

38. Vervloessem, T., Yule, D.I., Bultynck, G., and Parys, J.B. (2015). The type 2 inositol 1,4,5-trisphosphate receptor, emerging functions for an intriguing Ca^{2+}-release channel. Biochim. Biophys. Acta *1853*, 1992–2005.

39. Yue, L.L., Wang, L.Q., Du, Y.C., Zhang, W., Hamada, K., Matsumoto, Y., Jin, X., Zhou, Y.D., Mikoshiba, K., Gill, D.L., et al. (2020). Type 3 inositol 1,4,5-trisphosphate receptor is a crucial regulator of calcium dynamics mediated by endoplasmic reticulum in HEK cells. Cells *9*, 275. https://doi.org/10.3390/cells9020275.

40. Burgoyne, R.D., and Clague, M.J. (2003). Calcium and calmodulin in membrane fusion. Biochim. Biophys. Acta *1641*, 137–143. https://doi.org/10.1016/s0167-4889(03)00089-2.

41. Carlson, C.R., Aronsen, J.M., Bergan-Dahl, A., Moutty, M.C., Lunde, M., Lunde, P.K., Jarstadmarken, H., Wanichawan, P., Pereira, L., Kolstad, T.R.S., et al. (2022). AKAP18δ Anchors and Regulates CaMKII Activity at Phospholamban-SERCA2 and RYR. Circ. Res. *130*, 27–44. https://doi.org/10.1161/CIRCRESAHA.120.317976.

42. Vanderheyden, V., Devogelaere, B., Missiaen, L., De Smedt, H., Bultynck, G., and Parys, J.B. (2009). Regulation of inositol 1,4,5-trisphosphate-induced Ca^{2+} release by reversible phosphorylation and dephosphorylation. Biochim. Biophys. Acta *1793*, 959–970. https://doi.org/10.1016/j.bbamcr.2008.12.003.

43. Mauvezin, C., and Neufeld, T.P. (2015). Bafilomycin A1 disrupts autophagic flux by inhibiting both V-ATPase-dependent acidification and Ca-P60A/SERCA-dependent autophagosome-lysosome fusion. Autophagy *11*, 1437–1438. https://doi.org/10.1080/15548627.2015.1066957.

44. Yim, W.W.Y., Yamamoto, H., and Mizushima, N. (2022). A pulse-chasable reporter processing assay for mammalian autophagic flux with HaloTag. eLife *11*, e78923. https://doi.org/10.7554/eLife.78923.

45. Vest, R.S., Davies, K.D., O'Leary, H., Port, J.D., and Bayer, K.U. (2007). Dual mechanism of a natural CaMKII inhibitor. Mol. Biol. Cell *18*, 5024–5033. https://doi.org/10.1091/mbc.e07-02-0185.

46. Kim, K., Lakhanpal, G., Lu, H.E., Khan, M., Suzuki, A., Hayashi, M.K., Narayanan, R., Luyben, T.T., Matsuda, T., Nagai, T., et al. (2015). A Temporary Gating of Actin Remodeling during Synaptic Plasticity Consists of the Interplay between the Kinase and Structural Functions of CaMKII. Neuron *87*, 813–826. https://doi.org/10.1016/j.neuron.2015.07.023.

47. Wang, Q., Chen, M.C., Schafer, N.P., Bueno, C., Song, S.S., Hudmon, A., Wolynes, P.G., Waxham, M.N., and Cheung, M.S. (2019). Assemblies of calcium/calmodulin-dependent kinase II with actin and their dynamic regulation by calmodulin in dendritic spines. Proc. Natl. Acad. Sci. USA *116*, 18937–18942. https://doi.org/10.1073/pnas.1911452116.

48. Akita, T., Aoto, K., Kato, M., Shiina, M., Mutoh, H., Nakashima, M., Kuki, I., Okazaki, S., Magara, S., Shiihara, T., et al. (2018). *De novo* variants in *CAMK2A* and *CAMK2B* cause neurodevelopmental disorders. Ann. Clin. Transl. Neurol. *5*, 280–296. https://doi.org/10.1002/acn3.528.

49. Glatigny, M., Moriceau, S., Rivagorda, M., Ramos-Brossier, M., Nascimbeni, A.C., Lante, F., Shanley, M.R., Boudarene, N., Rousseaud, A., Friedman, A.K., et al. (2019). Autophagy Is Required for Memory Formation and Reverses Age-Related Memory Decline. Curr. Biol. *29*, 435–448.

50. Kallergi, E., Daskalaki, A.D., Kolaxi, A., Camus, C., Ioannou, E., Mercaldo, V., Haberkant, P., Stein, F., Sidiropoulou, K., Dalezios, Y., et al. (2022). Dendritic autophagy degrades postsynaptic proteins and is required for long-term synaptic depression in mice. Nat. Commun. *13*, 680. https://doi.org/10.1038/s41467-022-28301-z.

51. Alberti, S., and Hyman, A.A. (2021). Biomolecular condensates at the nexus of cellular stress, protein aggregation disease and ageing. Nat. Rev. Mol. Cell Biol. *22*, 196–213. https://doi.org/10.1038/s41580-020-00326-6.

52. Snead, W.T., and Gladfelter, A.S. (2019). The Control Centers of Biomolecular Phase Separation: How Membrane Surfaces, PTMs, and Active Processes Regulate Condensation. Mol. Cell *76*, 295–305. https://doi.org/10.1016/j.molcel.2019.09.016.

53. Shin, Y., and Brangwynne, C.P. (2017). Liquid phase condensation in cell physiology and disease. Science *357*, eaaf4382. https://doi.org/10.1126/science.aaf4382.

54. Wang, Z., Lou, J., and Zhang, H. (2022). Essence determines phenomenon: Assaying the material properties of biological condensates. J. Biol. Chem. *298*, 101782. https://doi.org/10.1016/j.jbc.2022.101782.

55. Zhang, H., Ji, X., Li, P.L., Liu, C., Lou, J.Z., Wang, Z., Wen, W.Y., Xiao, Y., Zhang, M.J., and Zhu, X.L. (2020). Liquid-liquid phase separation in biology: mechanisms, physiological functions and human diseases. Sci. China Life Sci. *63*, 953–985. https://doi.org/10.1007/s11427-020-1702-x.

56. Tsuboyama, K., Koyama-Honda, I., Sakamaki, Y., Koike, M., Morishita, H., and Mizushima, N. (2016). The ATG conjugation systems are important for degradation of the inner autophagosomal membrane. Science *354*, 1036–1041. https://doi.org/10.1126/science.aaf6136.

57. Li, X., Wu, X.Q., Deng, R., Li, D.D., Tang, J., Chen, W.D., Chen, J.H., Ji, J., Jiao, L., Jiang, S., et al. (2017). CaMKII-mediated Beclin 1 phosphorylation regulates autophagy that promotes degradation of Id and neuroblastoma cell differentiation. Nat. Commun. *8*, 1159. https://doi.org/10.1038/s41467-017-01272-2.

58. Wang, Q., Guo, W.J., Hao, B.X., Shi, X.L., Lu, Y.Y., Wong, C.W.M., Ma, V.W.S., Yip, T.T.C., Au, J.S.K., Hao, Q., et al. (2016). Mechanistic study of TRPM2-Ca^{2+}-CAMK2-BECN1 signaling in oxidative stress-induced autophagy inhibition. Autophagy *12*, 1340–1354. https://doi.org/10.1080/15548627.2016.1187365.

59. Zhan, Q., Jeon, J., Li, Y., Huang, Y., Xiong, J., Wang, Q., Xu, T.L., Li, Y., Ji, F.H., Du, G., et al. (2022). CAMK2/CaMKII activates MLKL in short-term starvation to facilitate autophagic flux. Autophagy *18*, 726–744. https://doi.org/10.1080/15548627.2021.1954348.

60. Brocke, L., Chiang, L.W., Wagner, P.D., and Schulman, H. (1999). Functional implications of the subunit composition of neuronal CaM kinase II. J. Biol. Chem. *274*, 22713–22722. https://doi.org/10.1074/jbc.274.32.22713.

61. Shen, K., Teruel, M.N., Subramanian, K., and Meyer, T. (1998). CaMKIIβ functions as an F-actin targeting module that localizes CaMKIIα/β heterooligomers to dendritic spines. Neuron *21*, 593–606. https://doi.org/10.1016/s0896-6273(00)80569-3.

62. Thiagarajan, T.C., Piedras-Renteria, E.S., and Tsien, R.W. (2002). alpha- and betaCaMKII. Inverse regulation by neuronal activity and opposing effects on synaptic strength. Neuron *36*, 1103–1114. https://doi.org/10.1016/s0896-6273(02)01049-8.

63. Guo, L., Stripay, J.L., Zhang, X., Collage, R.D., Hulver, M., Carchman, E.H., Howell, G.M., Zuckerbraun, B.S., Lee, J.S., and Rosengart, M.R. (2013). CaMKIα regulates AMP kinase-dependent, TORC-1-independent autophagy during lipopolysaccharide-induced acute lung neutrophilic inflammation. J. Immunol. *190*, 3620–3628. https://doi.org/10.4049/jimmunol.1102975.

64. Pfisterer, S.G., Mauthe, M., Codogno, P., and Proikas-Cezanne, T. (2011). Ca2+/calmodulin-dependent kinase (CaMK) signaling via CaMKI and AMP-activated protein kinase contributes to the regulation of WIPI-1 at the onset of autophagy. Mol. Pharmacol. *80*, 1066–1075. https://doi.org/10.1124/mol.111.071761.

65. Evankovich, J., Zhang, R., Cardinal, J.S., Zhang, L., Chen, J., Huang, H., Beer-Stolz, D., Billiar, T.R., Rosengart, M.R., and Tsung, A. (2012). Calcium/calmodulin-dependent protein kinase IV limits organ damage in hepatic ischemia-reperfusion injury through induction of autophagy. Am. J. Physiol. Gastrointest. Liver Physiol. *303*, G189–G198. https://doi.org/10.1152/ajpgi.00051.2012.

66. Zhang, X., Howell, G.M., Guo, L., Collage, R.D., Loughran, P.A., Zuckerbraun, B.S., and Rosengart, M.R. (2014). CaMKIV-dependent preservation of mTOR expression is required for autophagy during lipopolysaccharide-induced inflammation and acute kidney injury. J. Immunol. *193*, 2405–2415. https://doi.org/10.4049/jimmunol.1302798.

67. O'Leary, H., Lasda, E., and Bayer, K.U. (2006). CaMKIIβ association with the actin cytoskeleton is regulated by alternative splicing. Mol. Biol. Cell *17*, 4656–4665. https://doi.org/10.1091/mbc.e06-03-0252.

68. Fink, C.C., Bayer, K.U., Myers, J.W., Ferrell, J.E., Schulman, H., and Meyer, T. (2003). Selective regulation of neurite extension and synapse formation by the β but not the of isoform of CaMKII. Neuron *39*, 283–297. https://doi.org/10.1016/s0896-6273(03)00428-8.

69. LeBeux, Y.J., and Willemot, J. (1975). An ultrastructural study of the microfilaments in rat brain by means of heavy meromyosin labeling. I. The perikaryon, the dendrites and the axon. Cell Tissue Res. *160*, 1–36. https://doi.org/10.1007/BF00219840.

70. Wong, P.M., Feng, Y., Wang, J., Shi, R., and Jiang, X. (2015). Regulation of autophagy by coordinated action of mTORC1 and protein phosphatase 2A. Nat. Commun. *6*, 8048. https://doi.org/10.1038/ncomms9048.

71. Zhu, D.M., Tekle, E., Chock, P.B., and Huang, C.Y. (1996). Reversible phosphorylation as a controlling factor for sustaining calcium oscillations in HeLa cells: Involvement of calmodulin-dependent kinase II and a calyculin A-inhibitable phosphatase. Biochemistry *35*, 7214–7223. https://doi.org/10.1021/bi952471h.

72. Mattiazzi, A., and Kranias, E.G. (2011). CaMKII regulation of phospholamban and SR Ca^{2+} load. Heart Rhythm *8*, 784–787. https://doi.org/10.1016/j.hrthm.2010.11.035.

73. Bradshaw, J.M., Kubota, Y., Meyer, T., and Schulman, H. (2003). An ultrasensitive Ca2+/calmodulin-dependent protein kinase II-protein phosphatase 1 switch facilitates specificity in postsynaptic calcium signaling. Proc. Natl. Acad. Sci. USA *100*, 10512–10517. https://doi.org/10.1073/pnas.1932759100.

74. Fujioka, Y., Alam, J.M., Noshiro, D., Mouri, K., Ando, T., Okada, Y., May, A.I., Knorr, R.L., Suzuki, K., Ohsumi, Y., et al. (2020). Phase separation organizes the site of autophagosome formation. Nature *578*, 301–305. https://doi.org/10.1038/s41586-020-1977-6.

75. Denis, V., and Cyert, M.S. (2002). Internal Ca^{2+} release in yeast is triggered by hypertonic shock and mediated by a TRP channel homologue. J. Cell Biol. *156*, 29–34. https://doi.org/10.1083/jcb.200111004.

76. Noda, N.N., and Fujioka, Y. (2015). Atg1 family kinases in autophagy initiation. Cell. Mol. Life Sci. *72*, 3083–3096. https://doi.org/10.1007/s00018-015-1917-z.

77. Hosokawa, N., Hara, T., Kaizuka, T., Kishi, C., Takamura, A., Miura, Y., Iemura, S., Natsume, T., Takehana, K., Yamada, N., et al. (2009). Nutrient-dependent mTORC1 association with the ULK1-Atg13-FIP200 complex required for autophagy. Mol. Biol. Cell *20*, 1981–1991. https://doi.org/10.1091/mbc.e08-12-1248.

78. Memisoglu, G., Eapen, V.V., Yang, Y., Klionsky, D.J., and Haber, J.E. (2019). PP2C phosphatases promote autophagy by dephosphorylation of the Atg1 complex. Proc. Natl. Acad. Sci. USA *116*, 1613–1620. https://doi.org/10.1073/pnas.1817078116.

79. Fujioka, Y., Suzuki, S.W., Yamamoto, H., Kondo-Kakuta, C., Kimura, Y., Hirano, H., Akada, R., Inagaki, F., Ohsumi, Y., and Noda, N.N. (2014). Structural basis of starvation-induced assembly of the autophagy initiation complex. Nat. Struct. Mol. Biol. *21*, 513–521. https://doi.org/10.1038/nsmb.2822.

80. Yamamoto, H., Fujioka, Y., Suzuki, S.W., Noshiro, D., Suzuki, H., Kondo-Kakuta, C., Kimura, Y., Hirano, H., Ando, T., Noda, N.N., et al. (2016). The Intrinsically Disordered Protein Atg13 Mediates Supramolecular Assembly of Autophagy Initiation Complexes. Dev. Cell *38*, 86–99. https://doi.org/10.1016/j.devcel.2016.06.015.

81. Liang, Y., and Sigrist, S. (2018). Autophagy and proteostasis in the control of synapse aging and disease. Curr. Opin. Neurobiol. *48*, 113–121. https://doi.org/10.1016/j.conb.2017.12.006.

82. Lüningschrör, P., and Sendtner, M. (2018). Autophagy in the presynaptic compartment. Curr. Opin. Neurobiol. *51*, 80–85. https://doi.org/10.1016/j.conb.2018.02.023.

83. Ji, C.C., Zhao, H.Y., Li, D.F., Sun, H.Y., Hao, J.F., Chen, R.G., Wang, X.Q., Zhang, H., and Zhao, Y.G. (2020). Role of *Wdr45b* in maintaining neural autophagy and cognitive function. Autophagy *16*, 615–625. https://doi.org/10.1080/15548627.2019.1632621.

84. Suleiman, J., Allingham-Hawkins, D., Hashem, M., Shamseldin, H.E., Alkuraya, F.S., and El-Hattab, A.W. (2018). WDR45B-related intellectual disability, spastic quadriplegia, epilepsy, and cerebral hypoplasia: A consistent neurodevelopmental syndrome. Clin. Genet. *93*, 360–364. https://doi.org/10.1111/cge.13054.

85. Zhao, Y.G., Chen, Y., Miao, G.Y., Zhao, H.Y., Qu, W.Y., Li, D.F., Wang, Z., Liu, N., Li, L., Chen, S., et al. (2017). The ER-localized transmembrane protein EPG-3/VMP1 regulates SERCA activity to control ER-isolation membrane contacts for autophagosome formation. Mol. Cell *67*, 974–989.e6. https://doi.org/10.1016/j.molcel.2017.08.005.

86. Kimura, S., Noda, T., and Yoshimori, T. (2007). Dissection of the autophagosome maturation process by a novel reporter protein, tandem fluorescent-tagged LC3. Autophagy *3*, 452–460. https://doi.org/10.4161/auto.4451.

87. Wang, Z., Miao, G.Y., Xue, X., Guo, X.Y., Yuan, C.Z., Wang, Z.Y., Zhang, G.M., Chen, Y.Y., Feng, D., Hu, J.J., et al. (2016). The Vici syndrome

protein EPG5 is a Rab7 effector that determines the fusion specificity of autophagosomes with late endosomes/lysosomes. Mol. Cell *63*, 781–795. https://doi.org/10.1016/j.molcel.2016.08.021.

88. Chen, D., Zheng, Q.X., Sun, L., Ji, M.M., Li, Y., Deng, H.Y., and Zhang, H. (2021). ORF3a of SARS-CoV-2 promotes lysosomal exocytosis-mediated viral egress. Dev. Cell *56*, 3250–3263.e5. https://doi.org/10.1016/j.devcel.2021.10.006.
89. Zhao, Y.G., Liu, N., Miao, G.Y., Chen, Y., Zhao, H.Y., and Zhang, H. (2018). The ER contact proteins VAPA/B interact with multiple autophagy proteins to modulate autophagosome biogenesis. Curr. Biol. *28*, 1234–1245.e4. https://doi.org/10.1016/j.cub.2018.03.002.
90. Zhang, G., Wang, Z., Du, Z., and Zhang, H. (2018). mTOR regulates phase separation of PGL granules to modulate their autophagic degradation. Cell *174*, 1492–1506.e22. https://doi.org/10.1016/j.cell.2018.08.006.
91. Li, J., Shang, Z., Chen, J.H., Gu, W., Yao, L., Yang, X., Sun, X., Wang, L., Wang, T., Liu, S., et al. (2023). Engineering of NEMO as calcium indicators with large dynamics and high sensitivity. Nat. Methods *20*, 918–924. https://doi.org/10.1038/s41592-023-01852-9.

STAR★METHODS

KEY RESOURCES TABLE

REAGENT or RESOURCE	SOURCE	IDENTIFIER
Antibodies		
Rabbit polyclonal anti-FIP200	Proteintech	Cat# 17250-1-AP; RRID: AB_10666428
Mouse anti-ATG13	Merck	Cat# MABC46; RRID: AB_11211663
Rabbit anti-ATG13	Cell Signaling Technology	Cat# 13468S; RRID: AB_2797419
Mouse monoclonal anti-WIPI2	Abcam	Cat# ab105459; RRID: AB_10860881
Rabbit anti-ATG101	Cell Signaling Technology	Cat# 13492S; RRID: AB_2798234
Rabbit Anti-ULK1	Cell Signaling Technology	Cat# 8054S; RRID: AB_11178668
Anti-Thiophosphate ester antibody	Abcam	Cat# ab133473; RRID: AB_2737094
Mouse monoclonal anti-LC3 (clone 4E12)	MBL	Cat# M152-3; RRID: AB_1279144
Rabbit polyclonal anti-LC3	Cell Signaling Technology	Cat# 2775S; RRID: AB_915 950
Rabbit polyclonal anti-p62	MBL	Cat# PM045; RRID: AB_1279301
Mouse monoclonal anti-Halo	Promega	Cat# G9211; RRID: AB_2688011
Anti-FIP200 p-1127	This paper	N/A
Mouse monoclonal anti-GFP (clone 7.1 and 13.1)	Roche	Cat# 11814460001; RRID: AB_390913
Mouse monoclonal anti-GAPDH	Proteintech	Cat# 60004-1-Ig; RRID: AB_2107436
Bacterial and virus strains		
E. coli BL21-CodonPlus (DE3)	Agilent	Cat# 280230
Chemicals, peptides, and recombinant proteins		
Dulbecco's Modified Eagle's Medium, high glucose	Gibco	Cat# 11965092
Fetal Bovine Serum	ThermoFisher Scientific	Cat# 10099-141C
CellsSaving TM	NCM Biotech	Cat# C40100
Hank's balanced salt solution (HBSS)	Gibco	Cat# 14025092
DMEM without amino acids	Gibco	Cat# ME18226L1
BAPTA-AM	Abcam	Cat# AB120503
SNAP-Cell 647-SiR	New England BioLabs	Cat# S9102S
SNAP-Cell 505-Star	New England BioLabs	Cat# S9103S
HaloTag TMR ligand	Promega	Cat# G8251
Baf A1	MCE	HY-100558
Poly-L-Lysine	Sigma Aldrich	Cat# P4832
Triton X-100	ThermoFisher Scientific	Cat# HFH10
Digitonin	Sigma	Cat# D141
ATP-gS	Abcam	Cat# ab138911
p-Nitrobenzyl mesylate	Abcam	Cat# ab138910
Protease inhibitor cocktail	Roche	Cat# 11836170001
Protease and Phosphatase Inhibitor Cocktail	NCM Biotech	Cat# P002
Polybrene	M&C Gene Technology	Cat# MC032
Lipofectamine 2000	Life Technologies	Cat# 12566014
Lipofectamine RNAi MAX	Life Technologies	Cat# 13778150
Sepharose 4B beads	GE Healthcare	Cat# 17-0756-05
Ni-NTA agarose beads	QIAGEN	Cat# 30210
GFP-Trap agarose beads	Lablead	Cat# GNA-25-500
Coverslips	Matsunami	Cat# C015001
Deposited data		
Original blots and images	This paper	Mendeley Data: https://doi.org/10.17632/vhtn5s5dbx.1

(*Continued on next page*)

Continued

REAGENT or RESOURCE	SOURCE	IDENTIFIER
Experimental models: Cell lines		
COS7 cells	ATCC	N/A
Hela cells	ATCC	N/A
SHSY5Y cells	ATCC	N/A
CaMKIIβ KO COS7 cells	This paper	N/A
EI24 KO COS7 cells	Zheng et al.[36]	N/A
FIP200 KO COS7 cells	Zheng et al.[36]	N/A
Oligonucleotides		
Primers used for qRT-PCR experiments, see Table S1	This paper	N/A
siRNA and gRNA sequences, see Table S1	This paper	N/A
Recombinant DNA		
Flag-CaMKIIβ	This paper	N/A
SNAP-C1	This paper	N/A
SNAP-CaMKIIβ	This paper	N/A
SNAP-CaMKIIβ(ΔV1)	This paper	N/A
SNAP-CaMKIIβ(T287A)	This paper	N/A
SNAP-CaMKIIβ(T287D)	This paper	N/A
SNAP-CaMKIIβ(K43R)	This paper	N/A
SNAP-CaMKIIβ(P139L)	This paper	N/A
SNAP-CaMKIIβ(E110K)	This paper	N/A
SNAP-CaMKIIβ(K301E)	This paper	N/A
SNAP-CaMKIIβ(R284S)	This paper	N/A
SNAP-CaMKIIβ(E237K)	This paper	N/A
MBP-Calmodulin	This paper	N/A
WIPI2-mCherry	Zhao et al.[85]	N/A
Lifeact-mCherry	This paper	N/A
RFP-GFP-LC3	Kimura et al.[86]	Addgene Plasmid #21074
Halo-LC3	Zheng et al.[36]	N/A
mCherry-Sec61β	Zhao et al.[85]	N/A
SNAP-Sec61β	This paper	N/A
GFP-CN21	This paper	N/A
mCherry-CN21-CYB5	This paper	N/A
SNAP-CN21-CYB5	This paper	N/A
mGFP-FIP200	This paper	N/A
mGFP-FIP200-S105A	This paper	N/A
mGFP-FIP200-S161A	This paper	N/A
mGFP-FIP200-S415A	This paper	N/A
mGFP-FIP200-T1465A	This paper	N/A
mGFP-FIP200-T269A	This paper	N/A
mGFP-FIP200-T1127A	This paper	N/A
mGFP-FIP200-S1484A	This paper	N/A
mGFP-FIP200-T269D	This paper	N/A
mGFP-FIP200-T1127D	This paper	N/A
mGFP-FIP200-S1484D	This paper	N/A
mGFP-FIP200-T269A/T1127A/S1484A	This paper	N/A
MBP-FIP200-NTD	This paper	N/A
MBP-FIP200-CC1	This paper	N/A
MBP-FIP200-CC2	This paper	N/A
MBP-FIP200-Claw	This paper	N/A

(*Continued on next page*)

Continued

REAGENT or RESOURCE	SOURCE	IDENTIFIER
mCherry-FIP200	Zhao et al.[85]	N/A
RFP-LC3	Wang et al.[87]	N/A
TuNm	This paper	N/A
TuNer-c	This paper	N/A
ER-TuNm	This paper	N/A
NEMOf-CYB5	This paper	N/A
LAPM1-GCaMP6f	Chen et al.[88]	N/A
sfGFP-LC3	This paper	N/A
BFP2-LC3	This paper	N/A
Software and algorithms		
ImageJ	NIH	https://imagej.en.softonic.com/
GraphPad Prism	GraphPad Software	https://www.graphpad.com/
PyCharm Community Edition	JetBrains	https://www.jetbrains.com/pycharm/?var=1
3D Surface Plot plugins	ImageJ plugins	https://imagej.net/ij/plugins/surface-plot-3d.html
Proteome Discovery version 2.4.1.15	ThermoFisher	https://www.thermofisher.cn/cn/zh/home/industrial/mass-spectrometry/liquid-chromatography-mass-spectrometry-lc-ms/lc-ms-software/multi-omics-data-analysis/proteome-discoverer-software.html

EXPERIMENTAL MODEL AND STUDY PARTICIPANT DETAILS

Cell lines

COS7 cells, Hela cells and SHSY5Y cells are from ATCC and free of mycoplasma contamination. Cells were cultured in DMEM, supplemented with 10% FBS and 50 mg/ml penicillin-streptomycin at 37 °C with 5% CO_2. To starve cells, cells were washed with PBS three times and then cultured in amino acids-free DMEM or HBSS for the indicated time. For Bafilomycin.A1 (BafA1) treatment, cells were cultured in full DMEM containing BafA1 (100 nM) for the indicated time. For BAPTA-AM treatment, cells were treated with BAPTA-AM at 50 μM in full DMEM for 2 h.

METHOD DETAILS

Plasmids

mCherry-FIP200, WIPI2-mCherry, RFP-GFP-LC3, Halo-LC3, mCherry-Sec61β, and sfGFP-LC3 were generated as previously described.[85,89] CaMKIIβ was a gift from Mingjie Zhang (Southern University of Science and Technology). CaMKIIβ(ΔV1) was constructed by inserting mouse cDNA encoding CaMKIIβ(ΔV1) into SNAP vector. SNAP-CaMKIIβ and Flag-CaMKIIβ were constructed by inserting CaMKIIβ into SNAP vector or Flag vector. SNAP-CaMKIIβ(K43R), SNAP-CaMKIIβ(T287A), SNAP-CaMKIIβ(T287D), SNAP-CaMKIIβ(E110K), SNAP-CaMKIIβ(P139L), SNAP-CaMKIIβ(E237K), SNAP-CaMKIIβ(R284S) and SNAP-CaMKIIβ(K301E) were mutated from CaMKIIβ. mGFP-FIP200 was constructed by mutating GFP to GFP(A206K). mGFP-FIP200(S105A, S161A, S415A, T1465A, T269A, T1127A, S1484A, T269D, T1127D or S1484D) were constructed by introducing the corresponding mutation in mGFP-FIP200. NEMOf, TuNm and TuNer-C were gifts from Professor Youjun Wang (College of Life Sciences, Beijing Normal University). To construct NEMOf-CYB5, NEMOf was fused to the N-terminus of the CYB5 transmembrane domain.[36] ER-TuNm was constructed by fusing TuNm to the C-terminus of the transmembrane domain of TMCO1(1-31).

Transfection and RNAi

Cells were transiently transfected with the indicated plasmids using Lipofectamine 3000. For RNAi, cells were transfected with negative control (NC) or gene-specific siRNA oligos using Lipofectamine RNAi MAX, and collected 48 h or 72 h after transfection. The siRNA sequences used in this study are listed in Table S1.

Generation of knock-out cell lines

The COS7 *CaMKIIβ* KO cell line was generated using the CRISPR/Cas9 editing system. Cells were transiently transfected with the CRISPR px260 plasmid expressing the specific gRNA (Table S1) for 48 h and then selected with 2 μg/ml puromycin. Single clones

were picked, and the clones with the corresponding *CaMKIIβ* gene mutation were identified by genomic sequencing. *CaMKIIβ* KO cells were further confirmed by sequencing and also lack of detectable mRNA.

Immunostaining

Cells cultured on coverslips were fixed with 4% PFA for 15 min at room temperature. After rinsing 3 times with PBS, cells were permeabilized with 50 μg/ml digitonin (for LC3 staining) or 0.2% Triton X-100 (for other antibodies) for 10 min at room temperature. Permeabilized cells were blocked with 5% goat serum for 30 min. Cells were then incubated with the indicated primary antibodies (diluted in 5% goat serum) overnight at 4 °C. After washing 3 times with PBS, cells were incubated with fluorescent-dye conjugated secondary antibodies for 1 h at room temperature. Coverslips were mounted with DAPI in 50% glycerol and imaged using confocal microscope (LSM 880 Meta plus Zeiss Axiovert zoom, Zeiss) with a 63×/1.40 oil-immersion objective lens (Plan-Apochromatlan, Zeiss) and a camera (Axiocam HRm, Zeiss).

Immunoblotting assays

For immunoblotting, cells were lysed with lysis buffer (20 mM HEPES, pH 7.4, 150 mM NaCl, 1 mM EDTA, 1% Triton X-100 and protease inhibitor cocktail) and incubated for 30 min on ice. Homogenates were centrifuged at 13,000 rpm for 10 min at 4 °C. Supernatants were collected and boiled with SDS sample buffer and subjected to SDS-PAGE electrophoresis. Proteins were detected using the indicated primary and secondary antibodies. The polyvinylidene difluoride membrane was exposed using the ChemiScope 6000 Touch imaging system.

Halo-LC3 processing assay

COS7 cells were transfected with Halo-LC3 plasmid. 24 h post-transfection, cells were incubated with 100 nM TMR-conjugated HaloTag ligand in full DMEM for 30 min. After rinsing 3 times with PBS, cells were incubated with amino acid-free DMEM for 2 h. Cells were then lysed with lysis buffer (20 mM HEPES, pH 7.4, 150 mM NaCl, 1 mM EDTA, 1% Triton X-100 and protease inhibitor cocktail). After heating at 100 °C for 5 min, protein samples were separated by SDS-PAGE. Proteins were detected using the mouse monoclonal anti-Halo antibody and indicated secondary antibodies. The polyvinylidene difluoride membrane was exposed using the ChemiScope 6000 Touch imaging system. The processing rate for Halo-LC3 was calculated by the ratio of the free Halo band to the sum of the free Halo and unprocessed Halo-LC3 bands.

GFP-Trap

For GFP-Trap assays, cells were transfected with the indicated plasmids for 24 h, and harvested with lysis buffer (50 mM HEPES, pH 7.4, 150 mM NaCl, 1 mM EDTA and 1% Triton X-100) supplemented with protease inhibitor cocktail and phosphatase inhibitors. After incubation on ice for 30 min, cells were centrifuged at 13,000 rpm for 10 min at 4 °C. Supernatants were collected and incubated with GFP-Trap agarose beads with gentle rotation for 1-2 h at 4 °C. After washing 3 times with washing buffer (50 mM HEPES, pH 7.5, 150 mM NaCl, 1 mM EDTA and 0.1% Triton X-100), the bound proteins were eluted from GFP-Trap agarose beads by SDS sample buffer and analyzed by immunoblotting.

Exogenous Ca^{2+} stimulation assay

Cells expressing mGFP-FIP200, SNAP-CaMKIIβ or their mutants were cultured in medium containing 2 mM $CaCl_2$. Exogenous Ca^{2+} stimulation was performed by rapidly changing the medium Ca^{2+} concentration from 2 mM to 60 mM.

Fluorescence recovery after photobleaching (FRAP)

Cells cultured on coverslips were transfected with indicated plasmids for 24 h. FRAP experiments were performed on a Zeiss LSM 980 confocal microscope equipped with a 63×, 1.4 NA oil-immersion objective. Defined regions were photobleached by laser. The fluorescence intensities in these regions were collected every 1 s. The averaged image intensity of each region was normalized by the initial intensity before bleaching. Traces of normalized fluorescent changes before bleaching and after bleaching were plotted by GraphPad Prism.

Protein expression and purification

cDNAs encoding FIP200 fragments (NTD, CC1, CC2 and Claw) were PCR-amplified from GFP-FIP200 and inserted into pGEX-6P-1(GST), pET-MBP-3C and pET-GFP-3C vector. cDNA encoding Calmodulin was PCR-amplified from GFP-Calmodulin (CaM), then inserted into pET-MBP-3C vector. Recombinant proteins were expressed in *Escherichia coli* BL21-CodonPlus (DE3) in LB medium at 18 °C and purified using Sepharose 4B beads (for GST-tagged protein) and Ni-NTA agarose beads (for MBP-tagged proteins). After desalination with desalting columns, proteins were eluted with desalting buffer (20 mM HEPES, pH 7.4, 500 mM NaCl) and assessed by SDS-PAGE. For *in vitro* phosphorylation assays, CaMKIIβ protein was purified as follows. CaMKIIβ with N-terminal His6-SUMO tag was co-expressed with λ phosphatase in *Escherichia coli* BL21-CodonPlus (DE3) in LB medium at 16 °C for 24 h. The recombinant CaMKIIβ protein was purified by Ni^{2+}-NTA Sepharose 6 Fast Flow resin. Following the removal of the His6-SUMO tag by Ulp1

protease, the protein was subjected to further purification through Mono Q anion exchange chromatography and Superose 6 10/300 gel filtration chromatography. The final column buffer and storage buffer consisted of 50 mM Tris pH 8.0, 200 mM NaCl, 10% glycerol, and 5 mM DTT.

In vitro phosphorylation of fusion proteins by CaMKIIβ

For *in vitro* CaMKIIβ phosphorylation assays, the purified recombinant proteins CaMKIIβ, MBP-CaM, MBP-FIP200(NTD, CC1, CC2 and Claw) were preincubated with 2.5 mM EGTA in buffer (25 mM HEPES, 500 mM NaCl) for 30 min. CaMKIIβ was preincubated in kinase buffer (25 mM HEPES, 10 mM $MgCl_2$, 10 mM DTT, 2.5 mM EGTA, 500 μM ATP-γS, 3.5 mM $CaCl_2$, 1.5 μM MBP-CaM) for 10 min at 30°C. CaMKIIβ preincubated in kinase buffer in the absence of $CaCl_2$ and MBP-CaM was used as control. The preincubated fusion proteins (MBP-FIP200(NTD, CC1, CC2 and Claw)) were added to kinase buffer only, active CaMKIIβ or inactive CaMKIIβ for 30 min at 30°C. For detection by anti-thiophosphate-ester antibody, the reaction mixtures were further supplemented with 2.5 mM p-nitrobenzyl mesylate (PNBM). Alkylating reactions were incubated at room temperature for 1 h. The reactions were terminated with SDS sample buffer and boiled before analysis by SDS-PAGE.

In-gel digestion of proteins and LC-MS/MS analysis

In-gel digestion of proteins and LC-MS/MS analysis were performed as previously described.[90] Briefly, the gel bands were excised and digested manually. The protein bands were cut into small plugs, then washed twice in distilled water for 10 min each time. The gel bands were dehydrated in 100% acetonitrile and dried in a speedvac. Reduction (10 mM DTT in 25 mM NH_4HCO_3 for 45 min at 56°C) and alkylation (40 mM iodoacetamide in 25 mM NH_4HCO_3 for 45 min at room temperature in the dark) were performed, followed by washing of the gel plugs with 50% acetonitrile in 25 mM ammonium bicarbonate twice. The gel plugs were then dried using a speed-vac and digested with sequence-grade modified trypsin (40 ng for each band) in 25 mM NH_4HCO_3 overnight at 37 °C. The enzymatic reaction was stopped by adding formic acid to a 1% final concentration. The solution was then transferred to a sample vial for LC-MS/MS analysis.

All nanoLC-MS/MS experiments were performed on a Orbitrap Exploris 480 (Thermo Scientific) equipped with an Easy n-LC 1200 HPLC system (Thermo Scientific). The peptides were loaded onto a 100 μm id×2 cm fused silica trap column packed in-house with reversed phase silica (Reprosil-Pur C18 AQ, 5 μm, Dr. Maisch GmbH) and then separated on a 75 μm id×25 cm C18 column packed with reversed phase silica (Reprosil-Pur C18 AQ, 1.9 μm, Dr. Maisch GmbH). The peptides bound on the column were eluted with a 73-min linear gradient.

The MS analysis was performed with an Orbitrap Exploris 480 mass spectrometer with the FAIMS Pro interface (Thermo Scientific). FAIMS separations were performed with two compensation voltage (-45 and -65). With the data-dependent acquisition mode, the MS data were acquired at a high resolution 60,000 (m/z 200) across the mass range of 350–1500 m/z. The target value was 3.00E+06 with a maximum injection time of 22 ms. The precursor ions were selected from each MS full scan with isolation width of 1.6 m/z for fragmentation in the Ion Routing Multipole with normalized collision energy of 28%. Subsequently, MS/MS spectra were acquired at resolution 15,000 at m/z 200. The target value was 7.50E+04 with a maximum injection time of 22 ms. The dynamic exclusion time was 40 s. For nano electrospray ion source setting, the spray voltage was 2.0 kV; no sheath gas flow; the heated capillary temperature was 320 °C.

The raw data from Orbitrap Exploris 480 were analyzed with Proteome Discovery version 2.4.1.15 using Sequest HT search engine for protein identification. The data from the samples were searched against the Uniprot human protein database (updated on 11/2022).

p-FIP200(T1127) antibody

The anti-p-FIP200(T1127) antibody was generated by Hangzhou HuaAn Biotechnology Co., Ltd. The antigen peptide (AELRT(pi) LMTIEKDQC) was conjugated to carrier proteins (KLH, BSA, OVA) and the conjugated immunogen was injected into rabbits. The resulting antibody was purified and tested manually.

Multi-modal SIM (multi-SIM) living-cell imaging

The multi-SIM system was described previously.[36] The NA of the multi-SIM lens is 1.49 (Nikon CFI SR HP Apo TIRF 100×/1.49 oil objective lens).

For multi-SIM imaging experiments, COS7 cells transfected with the indicated plasmids were seeded onto coverslips 12-24 h prior to image. Cells transfected with SNAP plasmids were labeled with 20 nM SNAP-Cell 647-SiR for 10 min, and the cells were imaged immediately afterward. Cells were maintained in 37 °C and 5% CO_2 during imaging. Multiple cells were imaged at the same time using multi-ROI module. Time-lapse images were collected for 90 mins at intervals of 1 min, or 900 s at intervals of 10 to 20 seconds. Super-resolution images were processed by the WideField Deconvolution method and were analyzed by Image J.

Measurement of Ca^{2+} dynamics on the outer ER surface and data analysis

The Ca^{2+} indicator NEMOf, which exhibits less pH sensitivity and much larger dynamic range (F_{max}/F_{min}) than GCaMP6f,[91] was used for imaging Ca^{2+} dynamics on the ER surface in control and *CaMKIIβ* KO cells. The *EI24* KO cell line stably expressing GCaMP6f-CYB5 was used for analyzing ER Ca^{2+} transients in *EI24* KO cells and *EI24* KO cells with simultaneous depletion of *CaMKIIβ* or

expression of CYB5-CN21. Cells were cultured on coverslips 12 to 24 h after transfection of the indicated plasmids. During imaging, cells were maintained in HBSS (pH 7.2-7.3) at 37 °C and 5% CO_2. Time-lapse imaging was performed using a 100× objective (CFI Plan Apochromat Lambda, NA 1.45; Nikon) with immersion oil on an inverted fluorescence microscope (Eclipse Ti-E; Nikon) with a spinning-disk confocal scanner unit (UltraView; PerkinElmer). The excitation was 488 nm. Time-lapse images were acquired for 40 mins at intervals of 1 second with exposure time of 300 ms for each image. The XY axial pixel size of each image was 107 nm.

For data analysis, the regions with intensity transition were cropped manually. Background intensity was subtracted. The trace of NEMOf-CYB5 signal was normalized by the averaged initial baseline fluorescence of the whole focal plane, F_0. For analyzing Ca^{2+} transient amplitude, baseline fluorescence (F_0) was subtracted from the peak fluorescence (F), then $F-F_0$ was normalized by the baseline value (F_0) to give the transient amplitude $\Delta F/F_0 = (F-F_0)/F_0$. The area of transients was measured as the total pixels occupied by each peak. The transient number per ROI, amplitude ($\Delta F/F_0$), area of transients (pixels) and duration were calculated. An in-house Graphical User Interface (GUI) was developed using the PyQt5 framework. Transient peaks were marked manually using the GUI, and the amplitude and duration of each peak were recorded automatically. Data were analyzed by GraphPad Prism.

Ratiometric measurement of cytosolic Ca^{2+} concentration, ER store Ca^{2+} concentration and ER surface Ca^{2+} concentration

Ratiometric measurement of cytosolic Ca^{2+} concentration by TuNm was performed on a Zeiss LSM 880 confocal microscope equipped with a 63×, 1.4 NA oil-immersion objective lens and line sequential scan mode. Briefly, TuNm was constructed by fusing blue fluorescence protein mTurquoise2 to the N-terminus of NEMOf. The excitation and emission spectrum were set as GFP for NEMOf and CFP for mTurquoise2. Cytosolic Ca^{2+} concentration was measured by the ratio of GFP/CFP signal. Ratiometric measurement of ER store Ca^{2+} concentration by TuNer-C was similar to TuNm. The ER surface Ca^{2+} concentration indicator ER-TuNm was constructed by fusing TuNm with the transmembrane domain of TMCO1 as described above in "Plasmids". The ER surface Ca^{2+} changes were measured by the ratio of NEMOf signal to mTurquoise2 signal.

Image 3D surface plot

The amplitude and location of Ca^{2+} transients occurring at the same time in the cell is plotted by Fiji software. The 3D surface plot plug-in (https://imagej.net/ij/plugins/surface-plot-3d.html) was used to visualize the distribution of spatial fluorescence intensity of Ca^{2+} transients.

Electron microscopy

Cells were harvested and fixed with 2.5% glutaraldehyde in PBS overnight at 4 °C. Then cells were washed two times with PBS and once in ddH_2O. Next, cells were post-fixed in 1% OsO_4 and 1.5% $K_3Fe(CN)_6$ for 90 min at room temperature. Then, cells were washed with ddH_2O and placed in chilled 2% aqueous uranyl acetate for 1 h at room temperature. After washing with ddH_2O, cells were further dehydrated by a graded series of ethanol solutions and embedded in epoxy EMBED-812 resin (14120, Electron Microscopy Sciences). Images were acquired with an electron microscope (H-7800, Hitachi) at 100 kV using RADIUS 2.2 software at room temperature. The electron microscope was equipped with an AMT CCD camera (MoradaG3; EMSIS).

QUANTIFICATION AND STATISTICAL ANALYSIS

All of the experiments were repeated at least 3 times. Co-IP and immunoblotting results are representatives of at least three independent experiments. For immunostaining, the cells or images were randomly selected for analysis. Graph plots and *P*-values were generated using GraphPad Prism 7 software. Densities of immunoblot bands and immunofluorescence intensities of images were quantified using Image J software (NIH Image). Following one-way ANOVA, post hoc tests were conducted with the Dunnett or Sidak methods to analyze the differences between groups. Differences between the mean of each non-control group and the mean of a single control group (Figures 2B, 6S, 7D, 7E, S1F, S1I, S1C1, S2B, S2M, S4L, S5N, S5P, S6L, and S7B) were analyzed using Dunnett's multiple comparison test. Pairwise multiple comparisons between group means (Figures 5B, 5D, 5K, 5M, S4I, S4J, S5B, S5D, S5F, S5H, S5J, and S5L) were analyzed using Sidak's multiple comparison test. Other comparisons (comparisons between two normally distributed groups) were analyzed by Student's t test. The results are shown as mean ± S.E.M. ns: no significant difference; *: $P<0.05$; **: $P<0.01$; ***: $P<0.001$. Statistical parameters including the definitions, exact values of n, what n represents, and statistical significance are reported in the Figures and corresponding Figure Legends.

Molecular Cell, Volume *85*

Supplemental information

Ca^{2+}/calmodulin-dependent protein kinase II β decodes ER Ca^{2+} transients to trigger autophagosome formation

Qiaoxia Zheng, Huan Zhang, Hongyu Zhao, Yong Chen, Hongzhining Yang, Tingting Li, Qixu Cai, Yingyu Chen, Youjun Wang, Mingjie Zhang, and Hong Zhang

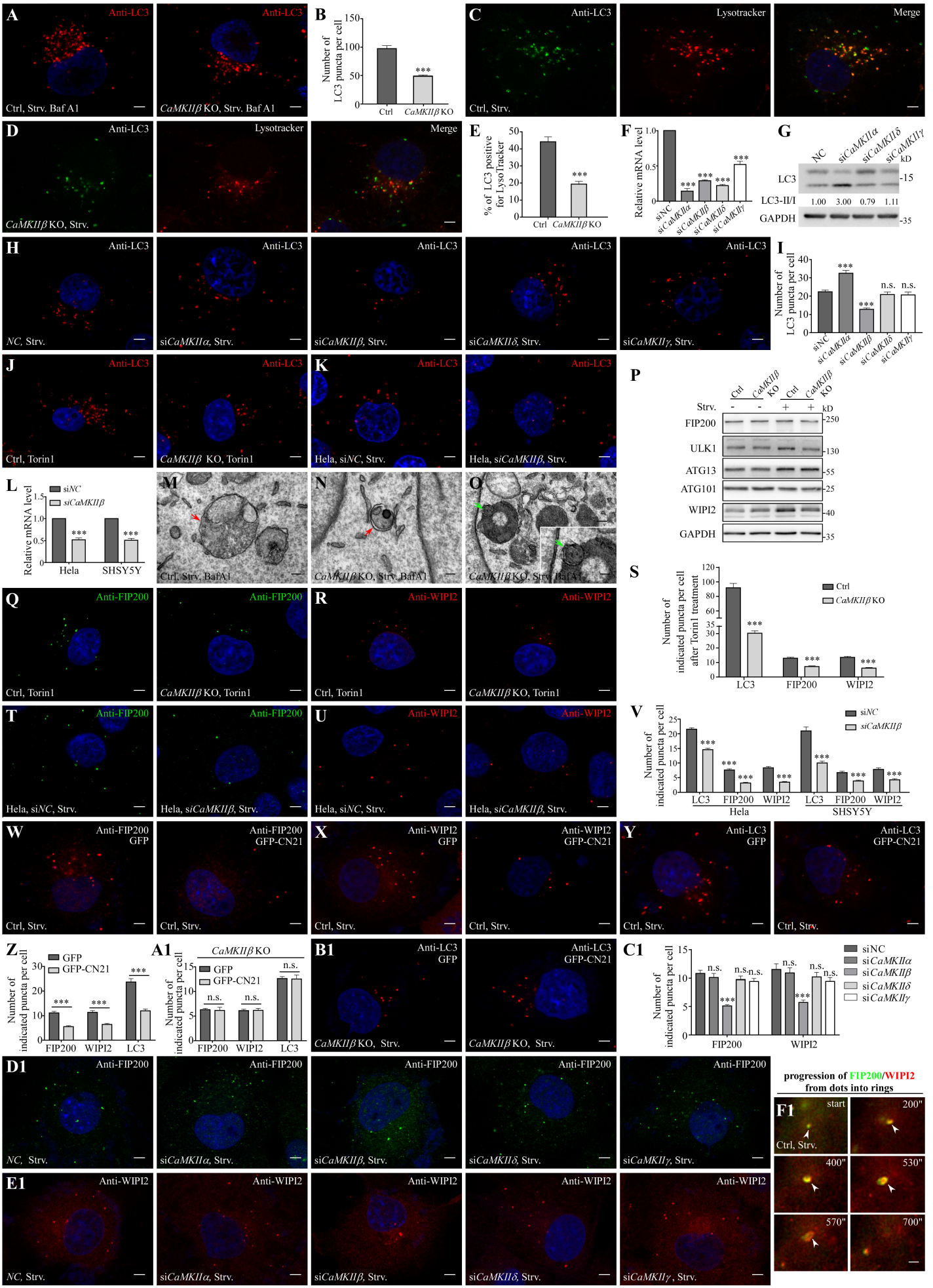
A
Anti-LC3
Ctrl, Strv. Baf A1
CaMKIIβ KO, Strv. Baf A1
B
Number of LC3 puncta per cell
Ctrl
CaMKIIβ KO
C
Anti-LC3
Lysotracker
Merge
Ctrl, Strv.
D
CaMKIIβ KO, Strv.
E
% of LC3 positive for LysoTracker
F
Relative mRNA level
siNC
siCaMKIIα
siCaMKIIβ
siCaMKIIδ
siCaMKIIγ
G
NC
kD
LC3
LC3-II/I
1.00 3.00 0.79 1.11
GAPDH
H
NC, Strv.
siCaMKIIα, Strv.
siCaMKIIβ, Strv.
siCaMKIIδ, Strv.
siCaMKIIγ, Strv.
I
n.s.
J
Ctrl, Torin1
CaMKIIβ KO, Torin1
K
Hela, siNC, Strv.
Hela, siCaMKIIβ, Strv.
P
Ctrl
CaMKIIβ KO
Strv.
FIP200
ULK1
ATG13
ATG101
WIPI2
GAPDH
L
siNC
siCaMKIIβ
Hela
SHSY5Y
M
Ctrl, Strv. BafA1
N
CaMKIIβ KO, Strv. BafA1
O
CaMKIIβ KO, Strv. BafA1
S
Number of indicated puncta per cell after Torin1 treatment
LC3
FIP200
WIPI2
Q
Anti-FIP200
R
Anti-WIPI2
T
U
V
Hela
SHSY5Y
W
Anti-FIP200
GFP
GFP-CN21
X
Anti-WIPI2
Y
Anti-LC3
Z
A1
CaMKIIβ KO
B1
C1
siNC
siCaMKIIα
siCaMKIIβ
siCaMKIIδ
siCaMKIIγ
D1
E1
progression of FIP200/WIPI2 from dots into rings
F1
start
200"
400"
530"
570"
700"

Figure S1

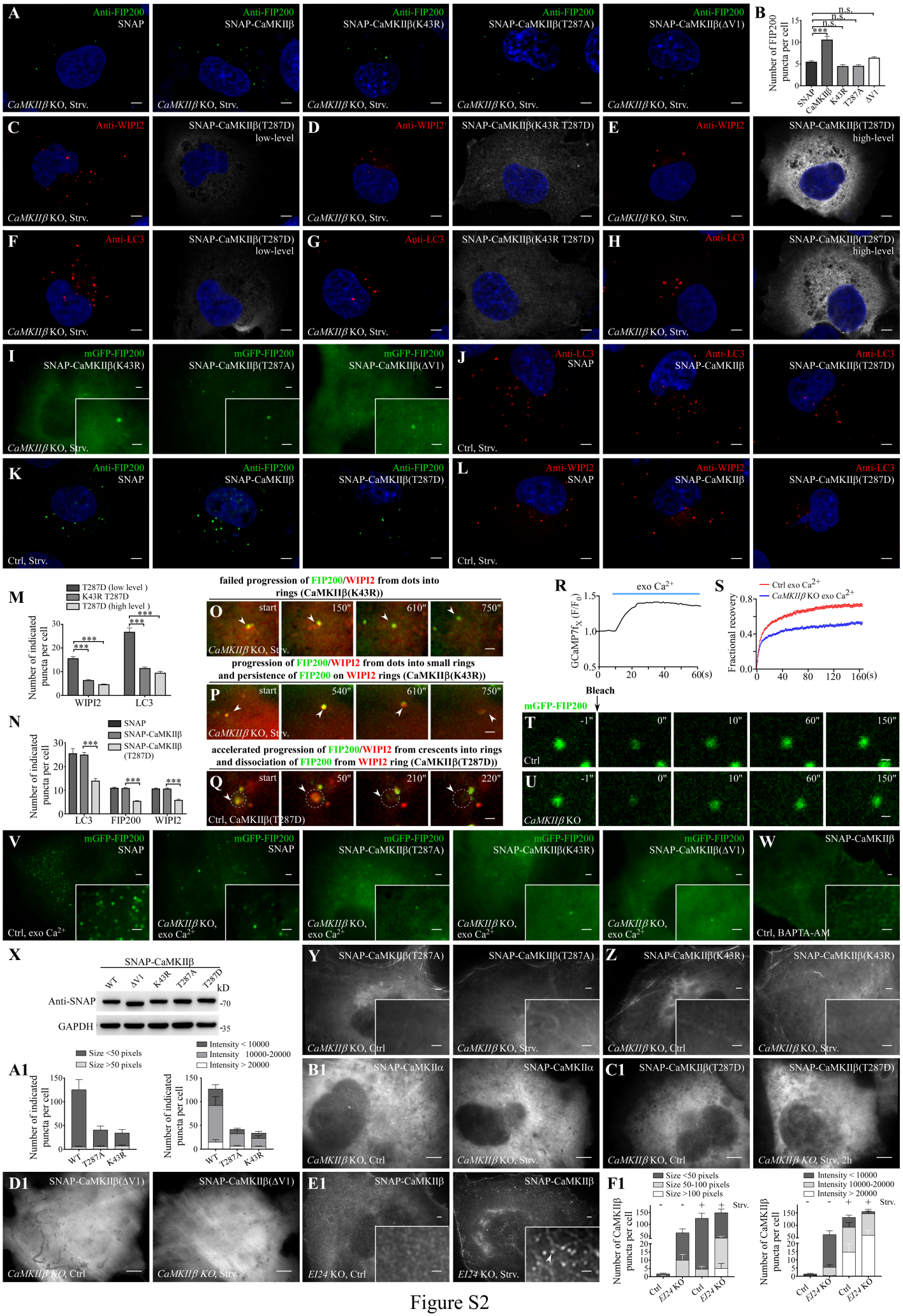
A
Anti-FIP200
SNAP
SNAP-CaMKIIβ
SNAP-CaMKIIβ(K43R)
SNAP-CaMKIIβ(T287A)
SNAP-CaMKIIβ(ΔV1)
CaMKIIβ KO, Strv.
B
Number of FIP200 puncta per cell
n.s.
***
C
Anti-WIPI2
SNAP-CaMKIIβ(T287D) low-level
D
SNAP-CaMKIIβ(K43R T287D)
E
SNAP-CaMKIIβ(T287D) high-level
F
Anti-LC3
G
H
I
mGFP-FIP200
J
Ctrl, Strv.
K
Ctrl, Strv.
L
M
T287D (low level)
K43R T287D
T287D (high level)
WIPI2
LC3
failed progression of FIP200/WIPI2 from dots into rings (CaMKIIβ(K43R))
O
start
150"
610"
750"
progression of FIP200/WIPI2 from dots into small rings and persistence of FIP200 on WIPI2 rings (CaMKIIβ(K43R))
P
540"
accelerated progression of FIP200/WIPI2 from crescents into rings and dissociation of FIP200 from WIPI2 ring (CaMKIIβ(T287D))
Q
50"
210"
220"
Ctrl, CaMKIIβ(T287D)
N
SNAP
SNAP-CaMKIIβ
SNAP-CaMKIIβ (T287D)
LC3
FIP200
WIPI2
R
exo Ca2+
GCaMP7fX (F/F0)
S
Ctrl exo Ca2+
CaMKIIβ KO exo Ca2+
Fractional recovery
Bleach
mGFP-FIP200
T
-1"
0"
10"
60"
150"
Ctrl
U
CaMKIIβ KO
V
Ctrl, exo Ca2+
CaMKIIβ KO, exo Ca2+
W
Ctrl, BAPTA-AM
X
SNAP-CaMKIIβ
WT
ΔV1
K43R
T287A
T287D
kD
Anti-SNAP
-70
GAPDH
-35
A1
Size <50 pixels
Size >50 pixels
Intensity < 10000
Intensity 10000-20000
Intensity > 20000
Number of indicated puncta per cell
Y
SNAP-CaMKIIβ(T287A)
Z
SNAP-CaMKIIβ(K43R)
B1
SNAP-CaMKIIα
C1
D1
SNAP-CaMKIIβ(ΔV1)
E1
SNAP-CaMKIIβ
F1
Size <50 pixels
Size 50-100 pixels
Size >100 pixels
Intensity < 10000
Intensity 10000-20000
Intensity > 20000
Number of CaMKIIβ puncta per cell
Strv.
Ctrl
E124 KO

Figure S2

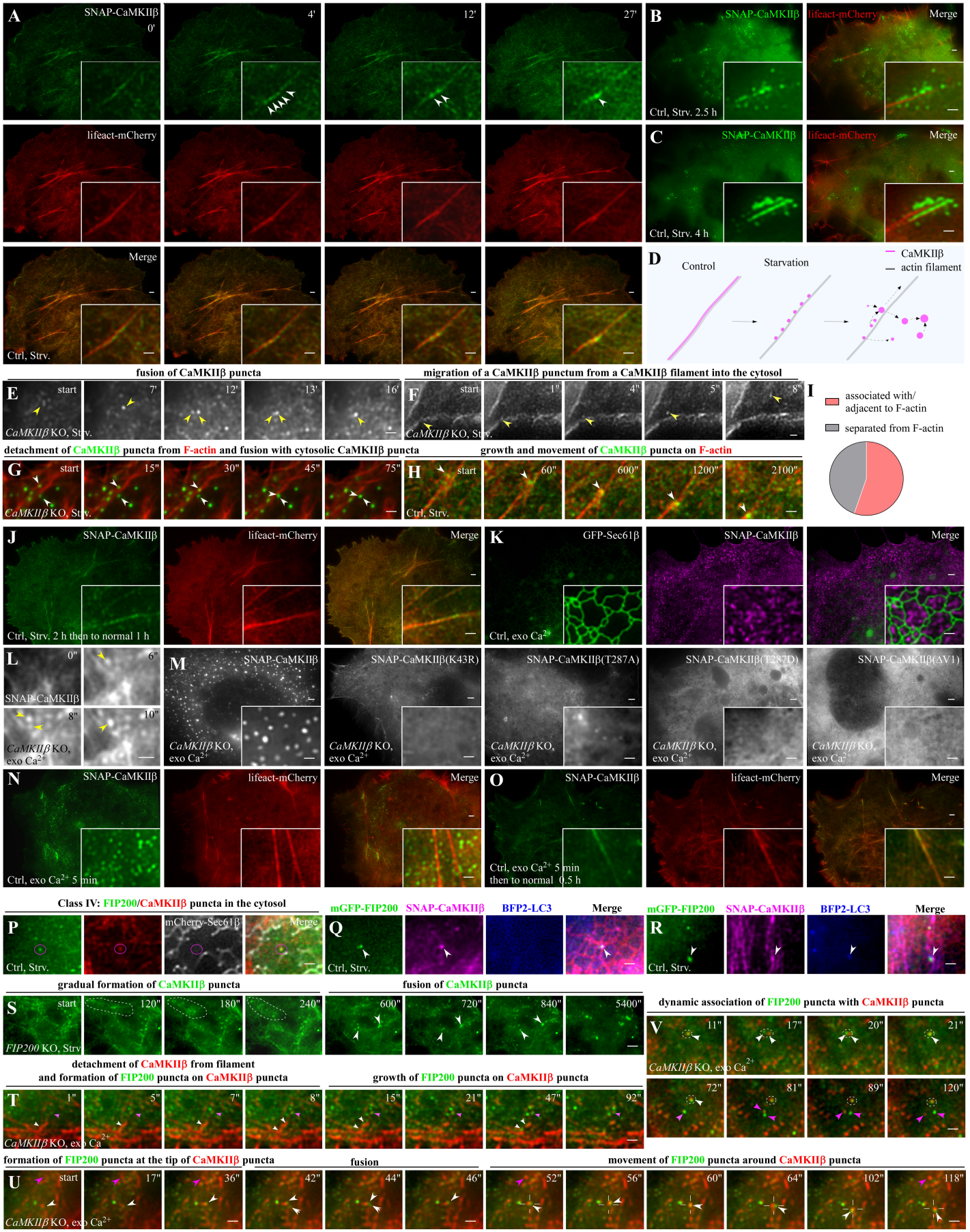
A
SNAP-CaMKIIβ
0'
4'
12'
27'
lifeact-mCherry
Merge
Ctrl, Strv.
B
SNAP-CaMKIIβ
lifeact-mCherry
Merge
Ctrl, Strv. 2.5 h
C
SNAP-CaMKIIβ
lifeact-mCherry
Merge
Ctrl, Strv. 4 h
D
Control
Starvation
CaMKIIβ
actin filament
fusion of CaMKIIβ puncta
E
start
7'
12'
13'
16'
CaMKIIβ KO, Strv.
migration of a CaMKIIβ punctum from a CaMKIIβ filament into the cytosol
F
start
1"
4"
5"
8"
CaMKIIβ KO, Strv.
I
associated with/
adjacent to F-actin
separated from F-actin
detachment of CaMKIIβ puncta from F-actin and fusion with cytosolic CaMKIIβ puncta
G
start
15"
30"
45"
75"
CaMKIIβ KO, Strv.
growth and movement of CaMKIIβ puncta on F-actin
H
start
60"
600"
1200"
2100"
Ctrl, Strv.
J
SNAP-CaMKIIβ
lifeact-mCherry
Merge
Ctrl, Strv. 2 h then to normal 1 h
K
GFP-Sec61β
SNAP-CaMKIIβ
Merge
Ctrl, exo Ca2+
L
0"
6"
8"
10"
SNAP-CaMKIIβ
CaMKIIβ KO,
exo Ca2+
M
SNAP-CaMKIIβ
SNAP-CaMKIIβ(K43R)
SNAP-CaMKIIβ(T287A)
SNAP-CaMKIIβ(T287D)
SNAP-CaMKIIβ(ΔV1)
CaMKIIβ KO,
exo Ca2+
N
SNAP-CaMKIIβ
lifeact-mCherry
Merge
Ctrl, exo Ca2+ 5 min
O
SNAP-CaMKIIβ
lifeact-mCherry
Merge
Ctrl, exo Ca2+ 5 min
then to normal 0.5 h
Class IV: FIP200/CaMKIIβ puncta in the cytosol
P
mCherry-Sec61β
Merge
Ctrl, Strv.
mGFP-FIP200
SNAP-CaMKIIβ
BFP2-LC3
Merge
Q
Ctrl, Strv.
R
Ctrl, Strv.
gradual formation of CaMKIIβ puncta
S
start
120"
180"
240"
FIP200 KO, Strv
fusion of CaMKIIβ puncta
600"
720"
840"
5400"
dynamic association of FIP200 puncta with CaMKIIβ puncta
V
11"
17"
20"
21"
72"
81"
89"
120"
CaMKIIβ KO, exo Ca2+
detachment of CaMKIIβ from filament
and formation of FIP200 puncta on CaMKIIβ puncta
T
1"
5"
7"
8"
CaMKIIβ KO, exo Ca2+
growth of FIP200 puncta on CaMKIIβ puncta
15"
21"
47"
92"
formation of FIP200 puncta at the tip of CaMKIIβ puncta
fusion
movement of FIP200 puncta around CaMKIIβ puncta
U
start
17"
36"
42"
44"
46"
52"
56"
60"
64"
102"
118"
CaMKIIβ KO, exo Ca2+

Figure S3

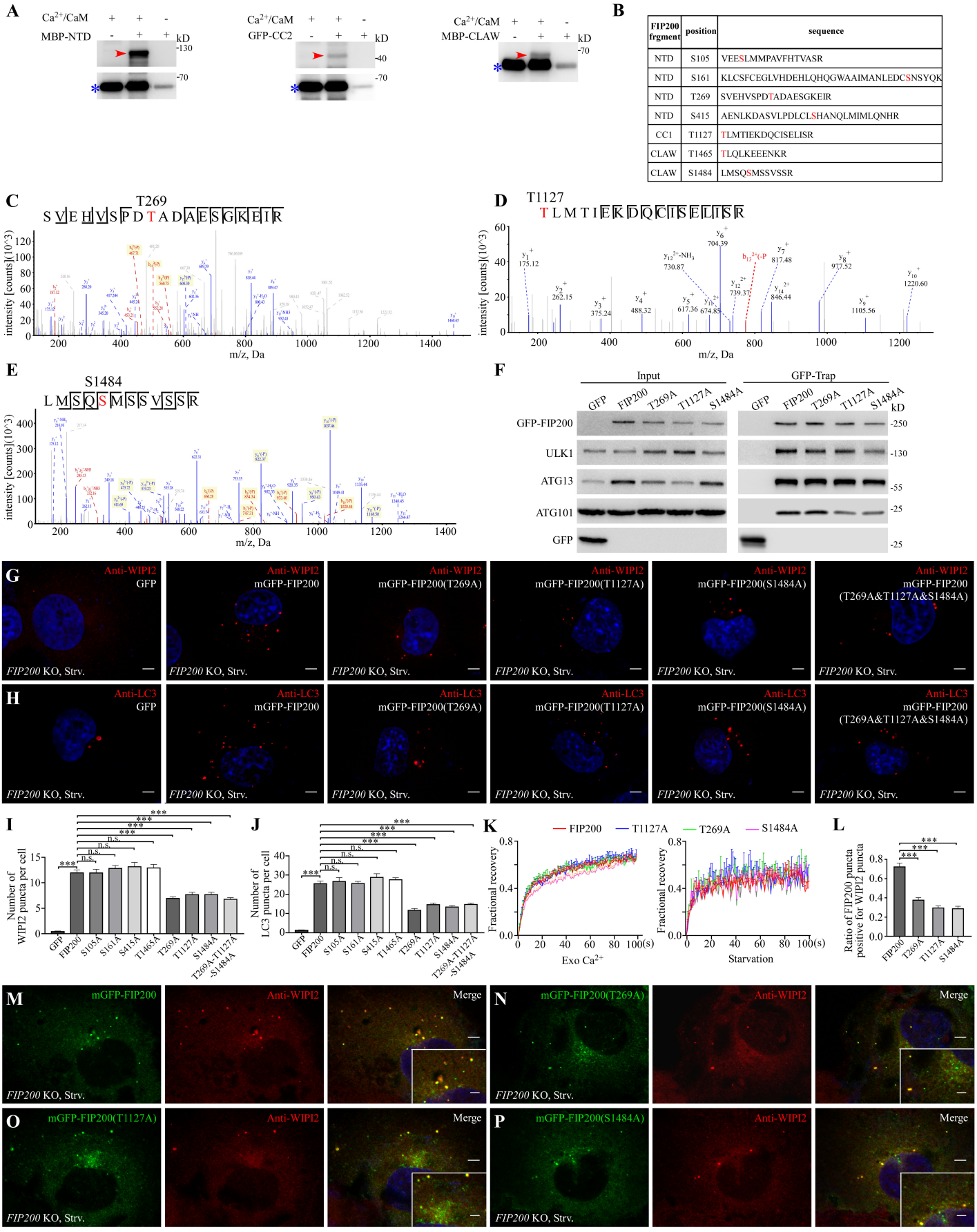
A
Ca2+/CaM + + -
MBP-NTD - + + kD
-130
-70
Ca2+/CaM + + -
GFP-CC2 - + + kD
-40
-70
Ca2+/CaM + + -
MBP-CLAW - + + kD
-70
B
FIP200 frgment | position | sequence
NTD | S105 | VEESLMMPAVFHTVASR
NTD | S161 | KLCSFCEGLVHDEHLQHQGWAAIMANLEDCSNSYQK
NTD | T269 | SVEHVSPDTADAESGKEIR
NTD | S415 | AENLKDASVLPDLCLSHANQLMIMLQNHR
CC1 | T1127 | TLMTIEKDQCISELISR
CLAW | T1465 | TLQLKEEENKR
CLAW | S1484 | LMSQSMSSVSSR
C
T269
S V E H V S P D T A D A E S G K E I R
intensity [counts](10^3)
m/z, Da
D
T1127
T L M T I E K D Q C I S E L I S R
intensity [counts](10^3)
m/z, Da
E
S1484
L M S Q S M S S V S S R
intensity [counts](10^3)
m/z, Da
F
Input
GFP-Trap
GFP FIP200 T269A T1127A S1484A
kD
GFP-FIP200
ULK1
ATG13
ATG101
GFP
-250
-130
-55
-25
-25
G
Anti-WIPI2
GFP
mGFP-FIP200
mGFP-FIP200(T269A)
mGFP-FIP200(T1127A)
mGFP-FIP200(S1484A)
mGFP-FIP200 (T269A&T1127A&S1484A)
FIP200 KO, Strv.
H
Anti-LC3
GFP
mGFP-FIP200
mGFP-FIP200(T269A)
mGFP-FIP200(T1127A)
mGFP-FIP200(S1484A)
mGFP-FIP200 (T269A&T1127A&S1484A)
FIP200 KO, Strv.
I
Number of WIPI2 puncta per cell
GFP FIP200 S105A S161A S415A T1465A T269A T1127A S1484A T269A-T1127A -S1484A
J
Number of LC3 puncta per cell
GFP FIP200 S105A S161A S415A T1465A T269A T1127A S1484A T269A-T1127A -S1484A
K
FIP200 T1127A T269A S1484A
Fractional recovery
Exo Ca2+
Starvation
L
Ratio of FIP200 puncta positive for WIPI2 puncta
FIP200 T269A T1127A S1484A
M
mGFP-FIP200
Anti-WIPI2
Merge
FIP200 KO, Strv.
N
mGFP-FIP200(T269A)
Anti-WIPI2
Merge
FIP200 KO, Strv.
O
mGFP-FIP200(T1127A)
Anti-WIPI2
Merge
FIP200 KO, Strv.
P
mGFP-FIP200(S1484A)
Anti-WIPI2
Merge
FIP200 KO, Strv.

Figure S4

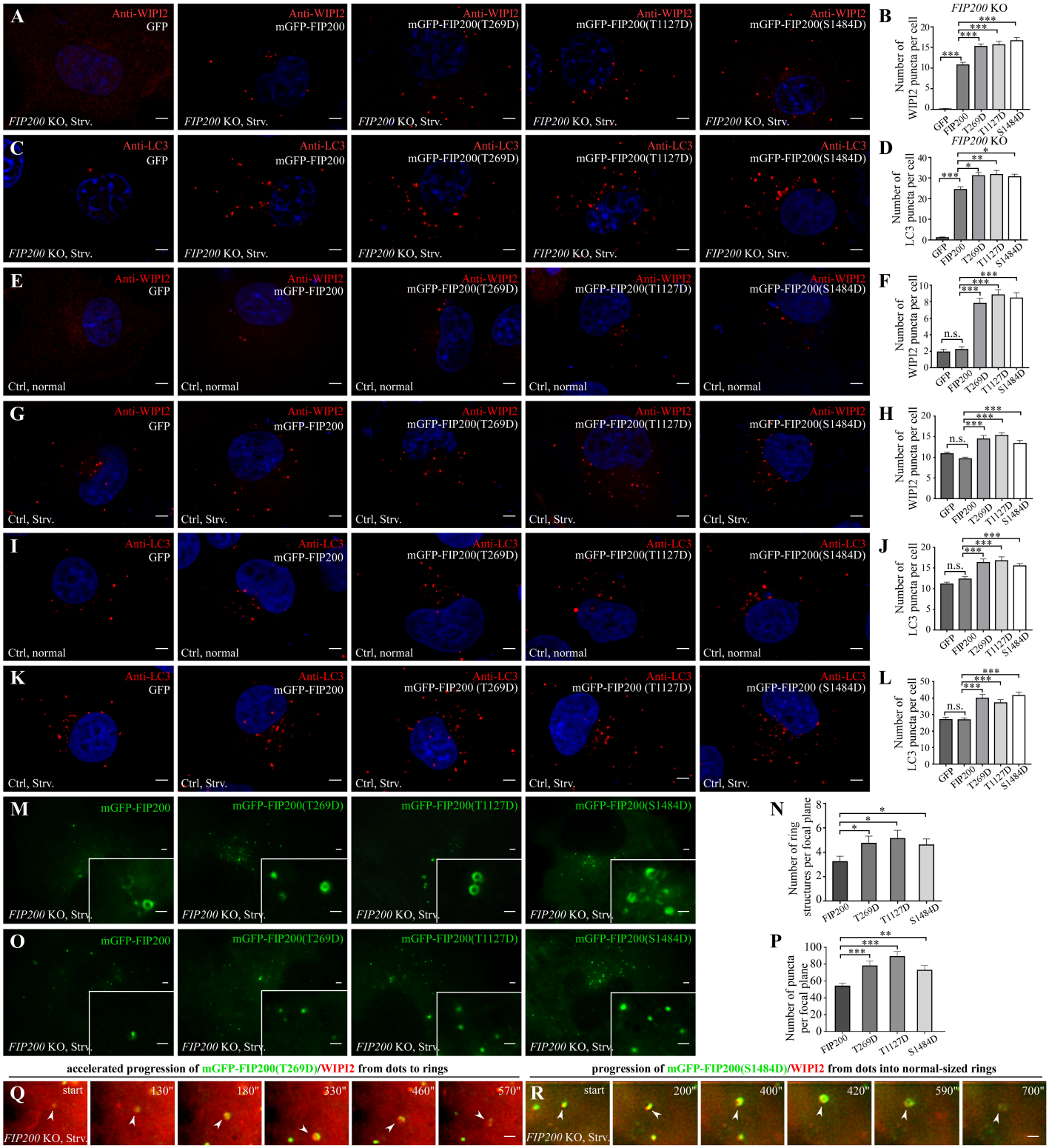
A
Anti-WIPI2
GFP
mGFP-FIP200
mGFP-FIP200(T269D)
mGFP-FIP200(T1127D)
mGFP-FIP200(S1484D)
FIP200 KO, Strv.
B
FIP200 KO
Number of WIPI2 puncta per cell
GFP
FIP200
T269D
T1127D
S1484D
C
Anti-LC3
D
Number of LC3 puncta per cell
E
Ctrl, normal
F
n.s.
G
Ctrl, Strv.
H
I
J
K
mGFP-FIP200 (T269D)
mGFP-FIP200 (T1127D)
mGFP-FIP200 (S1484D)
L
M
N
Number of ring structures per focal plane
O
P
Number of puncta per focal plane
accelerated progression of mGFP-FIP200(T269D)/WIPI2 from dots to rings
progression of mGFP-FIP200(S1484D)/WIPI2 from dots into normal-sized rings
Q
start
130"
180"
330"
460"
570"
R
200"
400"
420"
590"
700"

Figure S5

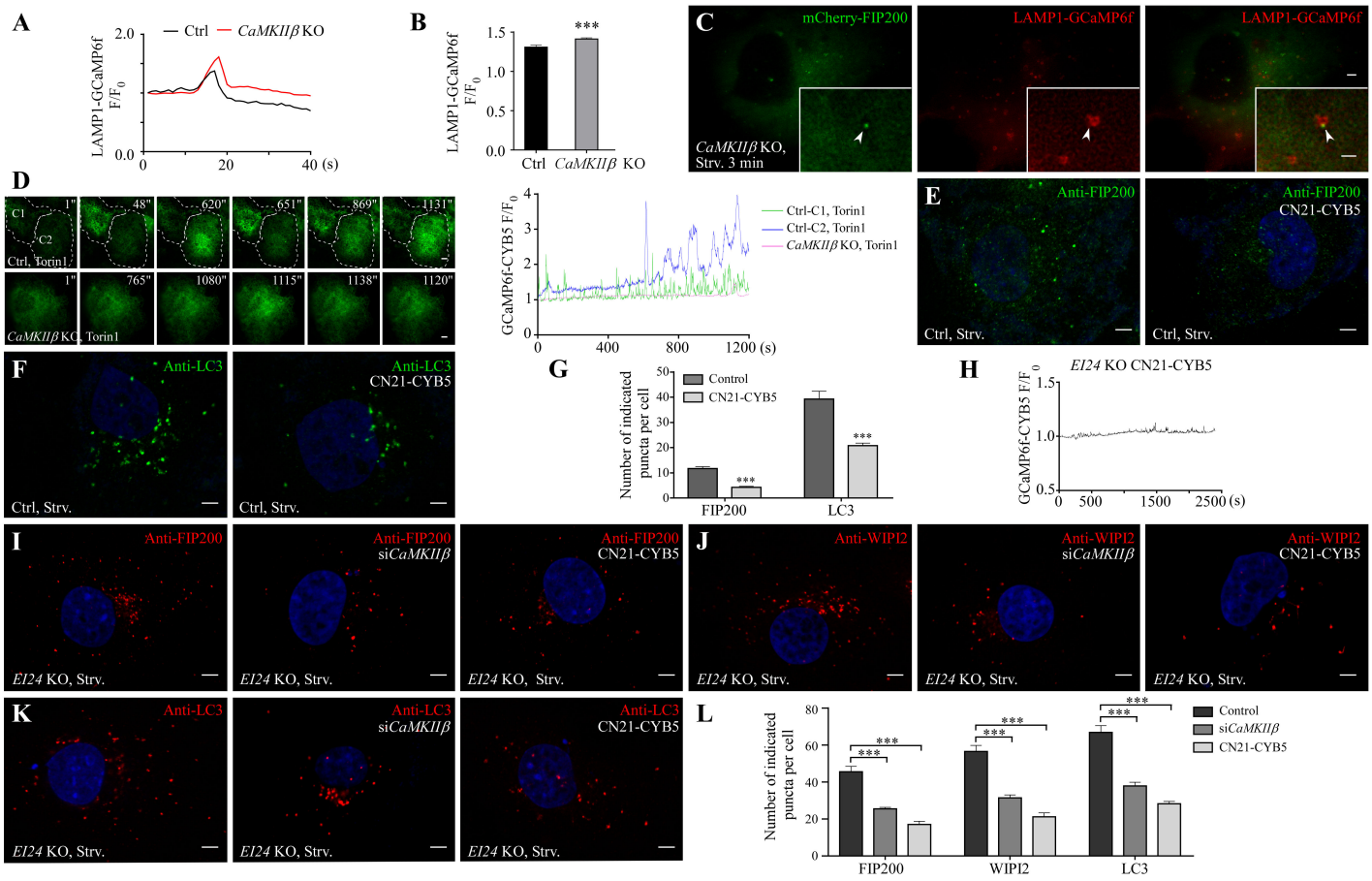
A
Ctrl
CaMKIIβ KO
LAMP1-GCaMP6f F/F0
2.0
0.0
0
20
40 (s)
B
LAMP1-GCaMP6f F/F0
1.5
1.0
0.5
0.0
***
Ctrl
CaMKIIβ KO
C
mCherry-FIP200
LAMP1-GCaMP6f
LAMP1-GCaMP6f
CaMKIIβ KO, Strv. 3 min
D
C1
C2
1"
48"
620"
651"
869"
1131"
Ctrl, Torin1
1"
765"
1080"
1115"
1138"
1120"
CaMKIIβ KO, Torin1
GCaMP6f-CYB5 F/F0
4
3
2
1
0
0
400
800
1200 (s)
Ctrl-C1, Torin1
Ctrl-C2, Torin1
CaMKIIβ KO, Torin1
E
Anti-FIP200
Anti-FIP200
CN21-CYB5
Ctrl, Strv.
Ctrl, Strv.
F
Anti-LC3
Anti-LC3
CN21-CYB5
Ctrl, Strv.
Ctrl, Strv.
G
Number of indicated puncta per cell
50
40
30
20
10
0
Control
CN21-CYB5
***
***
FIP200
LC3
H
EI24 KO CN21-CYB5
GCaMP6f-CYB5 F/F0
1.5
1.0
0.5
0
500
1500
2500 (s)
I
Anti-FIP200
Anti-FIP200
siCaMKIIβ
Anti-FIP200
CN21-CYB5
EI24 KO, Strv.
EI24 KO, Strv.
EI24 KO, Strv.
J
Anti-WIPI2
Anti-WIPI2
siCaMKIIβ
Anti-WIPI2
CN21-CYB5
EI24 KO, Strv.
EI24 KO, Strv.
EI24 KO, Strv.
K
Anti-LC3
Anti-LC3
siCaMKIIβ
Anti-LC3
CN21-CYB5
EI24 KO, Strv.
EI24 KO, Strv.
EI24 KO, Strv.
L
Number of indicated puncta per cell
80
60
40
20
0
***
***
***
***
***
***
Control
siCaMKIIβ
CN21-CYB5
FIP200
WIPI2
LC3

Figure S6

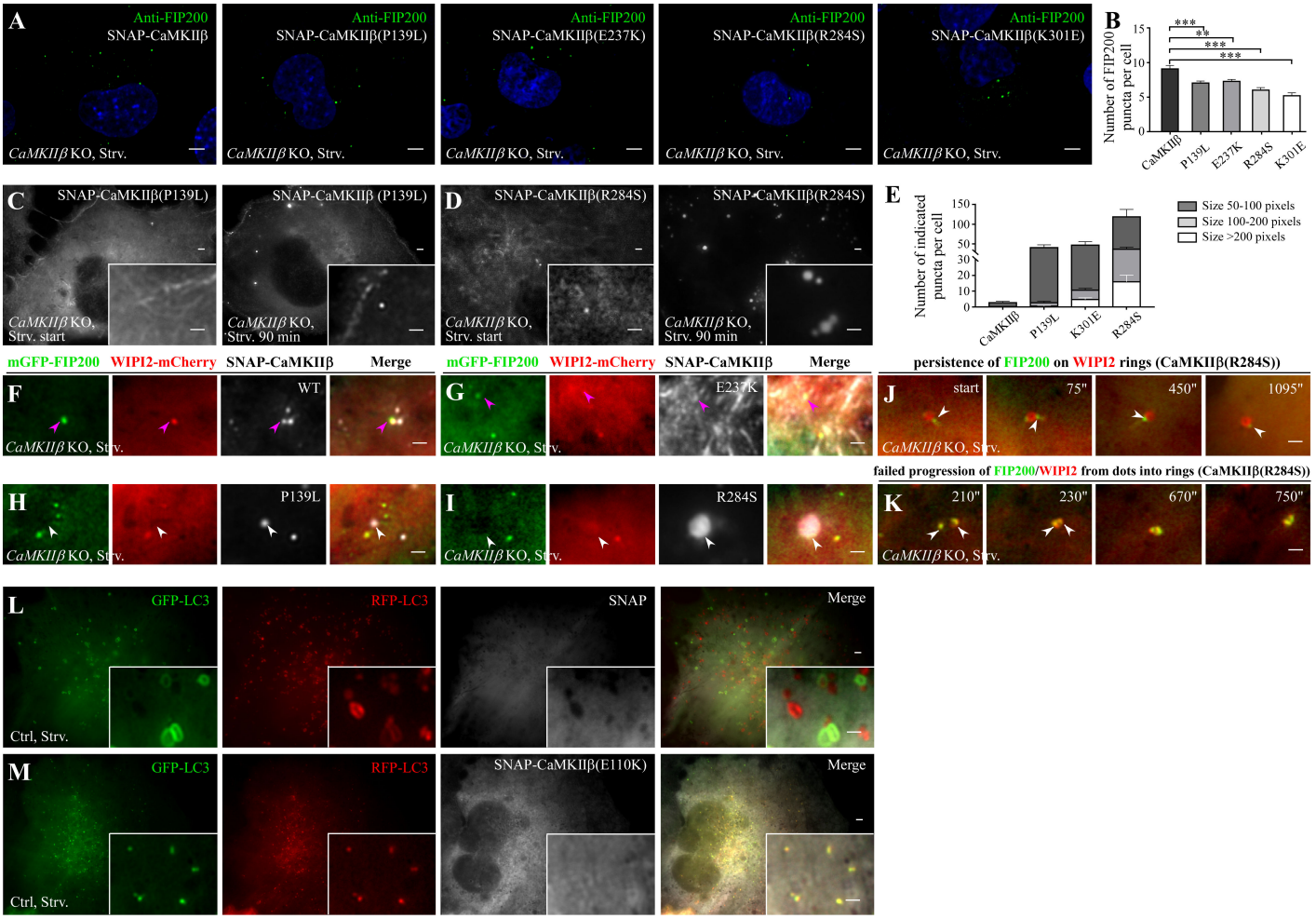
A
Anti-FIP200
SNAP-CaMKIIβ
SNAP-CaMKIIβ(P139L)
SNAP-CaMKIIβ(E237K)
SNAP-CaMKIIβ(R284S)
SNAP-CaMKIIβ(K301E)
CaMKIIβ KO, Strv.
B
Number of FIP200 puncta per cell
CaMKIIβ
P139L
E237K
R284S
K301E
C
SNAP-CaMKIIβ(P139L)
SNAP-CaMKIIβ (P139L)
CaMKIIβ KO, Strv. start
CaMKIIβ KO, Strv. 90 min
D
SNAP-CaMKIIβ(R284S)
E
Number of indicated puncta per cell
Size 50-100 pixels
Size 100-200 pixels
Size >200 pixels
mGFP-FIP200 WIPI2-mCherry SNAP-CaMKIIβ Merge
F
WT
G
E237K
persistence of FIP200 on WIPI2 rings (CaMKIIβ(R284S))
J
start
75"
450"
1095"
failed progression of FIP200/WIPI2 from dots into rings (CaMKIIβ(R284S))
H
P139L
I
R284S
K
210"
230"
670"
750"
L
GFP-LC3
RFP-LC3
SNAP
Merge
Ctrl, Strv.
M
SNAP-CaMKIIβ(E110K)

Figure S7

SUPPLEMENTAL ITEM

Table S1. List of oligonucleotides used in this study (related to STAR METHODS: Key Resources Table)

REAGENT or RESOURCE	SOURCE	IDENTIFIER
Oligonucleotides		
siRNA sequence for green monkey NC: 5'-UUCUCCGAACGUGUCACGUTT-3'	This paper	N/A
siRNA sequence for green monkey *CaMKIIα*: 5'-CCAAGGAUCUGAUCAAUAATT-3' 5'-GACUUCCAUCGAUUCUAUTT-3' 5'-CGAGGAUGAAGACACCAAATT-3'	This paper	N/A
siRNA sequence for green monkey *CaMKIIβ*: 5'-GGGAGCUCUUUGAAGACAUTT-3'	This paper	N/A
siRNA sequence for green monkey *CaMKIIδ*: 5'-GUGCCAUCUUGACAACUAUTT-3'	This paper	N/A
siRNA sequence for green monkey *CaMKIIγ*: 5'-GUGGCUCAAUGUCCACUAUTT-3'	This paper	N/A
siRNA sequence for human *CaMKIIβ*: 5'-CGUCACUCCUGAAGCCAAATT-3' 5'-CAGUGAAGCUGGCAGACUUTT-3' 5'-CCGGAAGCAGGAGAUCAUUTT-3'	This paper	N/A
gRNA for *CaMKIIβ* KO: 5'-TCTCCACGACAGCATCTCCG-3'	This paper	N/A
TMCO1 transmembrane domain (1-31) sequence: ATGAGCACTATGTTCGCGGACACTCTCCTCATCG TTTTTATCTCTGTGTGCACGGCTCTGCTCGCAGAG GGCATAACCTGGGTCCTGGTTTAC	This paper	N/A
RT-PCR primers for green monkey *GAPDH* (5'-3'): F: CAGCCTCAAGATCGTCAGCA R: TCTTCTGGGTGGCAGTGATG	This paper	N/A
RT-PCR primers for green monkey *CaMKIIα* (5'-3'): F: GTGGGCTTGTGGGGTCATCT R: TCCTGTTTCCGCACTTTGGT	This paper	N/A
RT-PCR primers for green monkey *CaMKIIβ* (5'-3'): F: CTTCGCAAAGAGGCGTATGG R: CGCTTGGCAGGGTTGATGGT	This paper	N/A
RT-PCR primers for green monkey *CaMKIIδ* (5'-3'): F: TCTGGGTAATTTAGTGGAAGG R: CATTTGGAATACAGGGTGGC	This paper	N/A
RT-PCR primers for green monkey *CaMKIIγ* (5'-3'): F: GCTTCACCGACGACTACCAG R: CGACATATCCGAGCCTCACG	This paper	N/A
RT-PCR primers for human *CaMKIIβ* (5'-3'): F: TGCACCACCAACTGCTTAGC R: GGCATGGACTGTGGTCATGAG	This paper	N/A

RT-PCR primers for human *GAPDH* (5'-3'): F: GCACACCAGGCTACCTGTC R: GGACGGGAAGTCATAGGCA	This paper	N/A

Supplemental figure legends

Figure S1. Depleting CaMKIIβ, but not other CaMKII family members, blocks autophagy, related to Figure 1.

(**A and B**) Compared to control cells, fewer LC3 puncta are formed in starved *CaMKIIβ* KO cells after BafA1 treatment. Quantification is shown in B (n=28 for BafA1-treated control cells and n=27 for BafA1-treated *CaMKIIβ* KO cells).

(C-E) Compared to control cells, LC3 puncta are largely separate from LysoTracker-labeled lysosomes in *CaMKIIβ* KO cells 4 h after amino acid starvation. Quantification of the % of LC3 puncta positive for LysoTracker is shown in (E) (n=32 for control cells and n=30 for *CaMKIIβ* KO cells).

(F) Knockdown efficiency shown by qRT-PCR. The mRNA level is effectively depleted by the corresponding siRNA. Data (normalized by *GAPDH* mRNA level) from three independent experiments are shown as mean ± SEM. The mRNA level in control cells is set to 1.0.

(G) Immunoblotting assays showing levels of LC3 in *CaMKIIα* KD cells, *CaMKIIγ* KD cells and *CaMKIIδ* KD cells. Quantifications of the ratio of LC3-II/LC3-I are shown at the bottom of the blot. The level in control cells is set to 1.00.

(H and I) The numbers of LC3 puncta are dramatically decreased in *CaMKIIβ* knockdown (KD) cells and increased in *CaMKIIα* KD cells. *CaMKIIγ* or *CaMKIIδ* KD has no evident effect on the number of LC3 puncta. Statistical analysis of LC3 puncta is shown in (I) (from left to right: n=44, 34, 39, 17 and 24 cells).

(**J**) Compared to Torin1-treated control cells, the number of endogenous LC3 puncta is dramatically reduced in Torin1-treated *CaMKIIβ* KO cells. Statistical analysis is shown in (S).

(K) The number of LC3 puncta is dramatically decreased in *CaMKIIβ* knockdown (KD) Hela cells after amino acid starvation. Statistical analysis of LC3 puncta in *CaMKIIβ* KD Hela and SHSY5Y cells after starvation is shown in (V).

(L) Knockdown efficiency shown by qRT-PCR in Hela and SHSY5Y cells. The mRNA level is depleted by the corresponding siRNA. Data (normalized by *GAPDH* mRNA level) from three independent experiments are shown as mean ± SEM. The mRNA level in control cells is set to 1.0.

(M-O) TEM analysis of autophagosomes and amphisomes in control and *CaMKIIβ* KO cells. In BafA1-treated starved control cells, amphisomes accumulate (arrow in M). In BafA1-treated starved *CaMKIIβ* KO cells, small unclosed autophagic structures are formed (arrow in N). The autophagic structures are sometimes closely associated with electron-dense late endosomal/lysosomal structures (arrow in O).

(P) Levels of FIP200, ULK1, ATG13, ATG101 and WIPI2 are not evidently changed in control cells and *CaMKIIβ* KO cells under normal or starvation conditions.

(**Q-S**) Compared to Torin1-treated control cells, the numbers of endogenous FIP200 puncta and WIPI2 puncta are dramatically reduced in Torin1-treated *CaMKIIβ* KO cells. Statistical analysis is shown in (S) (n=22, 23, 24, 20, 23 and 21 cells for bars from left to right).

(T-V) The numbers of FIP200 puncta and WIPI2 puncta are dramatically decreased in *CaMKIIβ* KD Hela cells after amino acid starvation. Statistical analyses of the

indicated puncta in *CaMKIIβ* KD Hela and SHSY5Y cells after starvation are shown in (V) (for bars from left to right: n=22, 23, 25, 26, 23 and 24 for Hela cells; n=26, 30, 36, 41, 39 and 42 for SHSY5Y cells).

(W-B1) Expressing GFP-CN21 dramatically reduces the number of FIP200 puncta (W), WIPI2 puncta (X) and LC3 puncta (Y) in starved control cells, but does not further reduce the number in *CaMKIIβ* KO cells (A1 and B1). Statistical analyses of the indicated puncta in control cells and *CaMKIIβ* KO cells are shown in (Z) and (A1), respectively (for bars from left to right: n=33, 33, 35, 39, 30 and 34 cells in (Z); n=22, 24, 35, 40, 26 and 26 cells in (A1)).

(C1-E1) The formation of FIP200 puncta and WIPI2 puncta in *CaMKIIα* KD, *CaMKIIβ* KD, *CaMKIIδ* KD, *CaMKIIγ* KD cells under starvation conditions. Statistical analysis of FIP200 puncta and WIPI2 puncta is shown in (C1) (for bars from left to right: n=25, 26, 30, 27 and 28 cells for FIP200 puncta; n=28, 29, 34, 37 and 35 cells for WIPI2 puncta).

(F1) The dynamic progression of FIP200/WIPI2 from dots into ring-like structures in HBSS-starved control cells. The whole process, from dots to disappearance of WIPI2 from ring structures, took about 700 seconds.

n.s.: no significance; ***: $p<0.001$. Data are shown as mean ± SEM in (B, E F, I, L, S, V, Z, A1 and C1). Scale bars: 5 μm (A, C, D, H, J, K, Q, R, T, U, W-Y, B1, D1, E1); 1 μm (F1); 200 nm (M-O); 100 nm (insert in O).

Figure S2. The kinase and actin-binding activities of CaMKIIβ are required for its function in autophagosome formation, related to Figure 2.

(A) FIP200 puncta in starved *CaMKIIβ* KO cells expressing WT CaMKIIβ or various CaMKIIβ mutants. Statistical analysis of FIP200 puncta is shown in (B) (for bars from left to right: n=25, 22, 22, 31 and 24 cells for FIP200 puncta).

(C-H) WIPI2 puncta (C-E) and LC3 puncta (F-H) in starved *CaMKIIβ* KO cells expressing a low or high level of CaMKIIβ(T287D) mutants or CaMKIIβ(K43R T287D). Statistical analysis of WIPI2 puncta and LC3 puncta in starved cells is shown in (M) (for bars from left to right: n=26, 29 and 25 cells for WIPI2 puncta; n=24, 34 and 22 cells for LC3 puncta).

(I) Multi-SIM imaging shows the formation of mGFP-FIP200 puncta in *CaMKIIβ* KO cells expressing various CaMKIIβ mutants after HBSS starvation for 90 min.

(J-L and N) Compared to expression of wild-type CaMKIIβ, high-level expression of CaMKIIβ(T287D) suppresses the number of LC3 puncta (J), FIP200 puncta (K) and WIPI2 puncta (L) in control cells under starvation conditions. Quantifications of LC3 puncta, FIP200 puncta and WIPI2 puncta are shown in (N) (n=23, 26, 24, 25, 31, 28, 25, 31 and 28 cells for bars from left to right).

(O and P) In *CaMKIIβ* KO cells expressing CaMKIIβ(K43R), FIP200/WIPI2 puncta (indicated by arrowheads) fail to organize into ring-like structures (O), or the puncta progress into small ring structures with persistence of FIP200 on WIPI2 rings (P).

(Q) In control cells expressing a low level of CaMKIIβ(T287D), the progression of a crescent FIP200/WIPI2 structure into a ring structure and also dissociation of FIP200/WIPI2 (highlighted by dashed circles) is faster than in control cells (Figure 1P) under starvation conditions.

(R) Adding Ca^{2+} in the culture medium (exo Ca^{2+} stimulation) causes an abrupt increase in cytosolic Ca^{2+} transients, which is shown by $GCaMP7_f$ fluorescence.

(S-U) FRAP analysis of the FIP200 fluorescence signal in puncta formed in response to exo Ca^{2+} stimulation in control and *CaMKIIβ* KO cells. (S) shows the quantification of FRAP. Data are shown as mean ± SEM (n=76 per group). The y axis shows the fractional recovery, which refers to the fraction of the difference between the intensity before or immediately after bleaching.

(V) Upon exo Ca^{2+} stimulation, compared to control cells, mGFP-FIP200 puncta are fewer in number in *CaMKIIβ* KO cells or in *CaMKIIβ* KO cells expressing CaMKIIβ(T287A, K43R or ΔV1) mutants. The number of mGFP-FIP200 puncta is lower in *CaMKIIβ* KO cells expressing CaMKIIβ(T287A, K43R or ΔV1) than in *CaMKIIβ* KO cells.

(W) BAPTA-AM treatment inhibits the formation of CaMKIIβ puncta.

(X) Immunoblotting assay showing levels of different CaMKIIβ mutants in *CaMKIIβ* KO cells. The same transfection level was used for analyzing formation of CaMKIIβ mutant puncta during starvation.

(Y and Z) SNAP-CaMKIIβ(T287A) and SNAP-CaMKIIβ(K43R) exhibit filamentous distribution under normal conditions, and form puncta after starvation. The number of SNAP-CaMKIIβ(T287A or K43R) puncta is lower than for wild-type SNAP-CaMKIIβ.

(A1) The size and intensity of puncta formed by wild-type and mutant CaMKIIβ in *CaMKIIβ* KO cells under starvation for 2.5 h (n=1503 puncta from 12 wild-type CaMKIIβ-transfected cells, 865 puncta from 21 CaMKIIβ(T287A)-transfected cells,

and 703 puncta from 21 CaMKIIβ(K43R)-transfected cells). Images were taken with the same laser power and exposure time. The size (in pixels) and fluorescence intensity of CaMKIIβ puncta were analyzed with GraphPad Prism.

(B1-D1) Distribution pattern of wild-type CaMKIIα, CaMKIIβ(T287D) and CaMKIIβ(ΔV1) expressed in *CaMKIIβ* KO cells. All three are diffuse in the cytosol under both normal and starvation conditions.

(E1) The number of SNAP-CaMKIIβ puncta is much higher in *EI24* KO cells than in control cells under nutrient-rich and starvation conditions.

(F1) The size and intensity of CaMKIIβ puncta under normal and starvation conditions in control (CaMKIIβ-transfected *CaMKIIβ* KO cells) and *EI24* KO cells. n=12 puncta from 12 control cells; 1503 puncta from 12 control cells starved for 2.5 h. n=752 puncta from 6 *EI24* KO cells under normal conditions; 3663 puncta from 13 *EI24* KO cells starved for 2.5 h. Images were taken with the same laser power and exposure time. The size (in pixels) and fluorescence intensity of CaMKIIβ puncta were analyzed with GraphPad Prism.

***: $p<0.001$. Scale bars: 5 μm (A, C-H, J-L); 2 μm (I, V, W, Y, Z, B1-E1); 1 μm (O-Q, T, U, and inserts in I, V, W, Y, Z, E1).

Figure S3. The spatiotemporal organization of CaMKIIβ puncta and FIP200 puncta in response to starvation or exo Ca^{2+} stimulation, related to Figure 3.

(A) Prior to starvation, SNAP-CaMKIIβ exhibits a filamentous distribution pattern which is closely aligned with F-actin. Upon HBSS starvation, breaks appear in the SNAP-CaMKIIβ signal, and distinct puncta (white arrowheads) form on or closely adjacent

to F-actin filaments. The intensity of puncta is gradually increased as the starvation proceeds. The F-actin pattern does not change during HBSS starvation.

(B and C) Multi-SIM images showing that CaMKIIβ puncta form on or close to F-actin and in the cytosol in *CaMKIIβ* KO cells under HBSS starvation conditions for 2.5 h (B) and 4 h (C).

(D) Schematic illustration of the formation and dynamics of CaMKIIβ puncta on F-actin and in the cytosol during HBSS starvation.

(E) Fusion of small CaMKIIβ puncta (arrowheads) during HBSS starvation.

(F) A CaMKIIβ punctum (arrowheads) migrates from the CaMKIIβ filament into the cytosol during HBSS starvation.

(G) Time-lapse analysis showing that a CaMKIIβ punctum moves away from F-actin and fuses with a cytosolic CaMKIIβ punctum (arrowheads) during HBSS starvation.

(H) CaMKIIβ puncta (arrowheads) move on an actin filament during HBSS starvation.

(I) Quantification of the relationship between CaMKIIβ puncta and actin filaments in cells starved for 2.5 hours. n=1869 CaMKIIβ puncta from 12 *CaMKIIβ* KO cells. The proportion of CaMKIIβ puncta associated with/adjacent to F-actin and separate from F-actin was 0.55 and 0.45, respectively.

(J) CaMKIIβ returns to its F-actin-associated filament pattern when cells were allowed to recover for 1 hour after 2 hours' starvation.

(K) Exo Ca^{2+} triggers formation of a large number of CaMKIIβ puncta that are localized in the cytosol or on the ER.

(L) CaMKIIβ puncta triggered by exo Ca^{2+} stimulation undergo fusion (labeled by yellow arrowheads).

(M) In response to exo Ca^{2+} stimulation, SNAP-CaMKIIβ forms a large number of puncta. Compared to wild-type SNAP-CaMKIIβ, SNAP-CaMKIIβ(K43R or T287A) forms fewer puncta. Formation of SNAP-CaMKIIβ(K43R) puncta is also slower (filamentous structures are still present). CaMKIIβ(T287D) and CaMKIIβ(ΔV1) remain diffuse upon exo Ca^{2+} stimulation.

(N and O) Upon exo Ca^{2+} stimulation, CaMKIIβ forms a large number of puncta that are attached to or separate from the actin filaments (N). After exo Ca^{2+} is removed, CaMKIIβ re-attaches and aligns with the actin filaments (O).

(P) Some FIP200/CaMKIIβ puncta are located in the cytosol, away from the ER.

(Q and R) FIP200 puncta that are associated with CaMKIIβ puncta can be negative for (Q) or associated with (R) LC3 puncta (indicated by arrowheads).

(S) In *FIP200* KO cells, CaMKIIβ still forms a large number of puncta (in the area enclosed by dashed lines) under starvation conditions. CaMKIIβ puncta occasionally undergo fusion (indicated by arrowheads).

(T) In response to exo Ca^{2+} stimulation, FIP200 puncta are formed on the CaMKIIβ filaments, and many of them, as in starved cells, are found at the breakage sites of CaMKIIβ filaments (white arrowheads). FIP200 puncta can also form on the tip of CaMKIIβ puncta (magenta arrowheads).

(U) CaMKIIβ puncta triggered by exo Ca^{2+} stimulation show dynamic association with FIP200 puncta. FIP200 forms puncta on the tip of CaMKIIβ puncta (0-42 seconds, arrowheads). The FIP200 puncta move around the CaMKIIβ puncta (46-118 seconds; the crosshairs indicate the position of the CaMKIIβ puncta). Neighboring FIP200 puncta, but not the associated CaMKIIβ puncta, undergo fusion (42-44

seconds, arrowheads). The CaMKIIβ puncta also grow larger and stronger over time (indicated by the magenta arrowhead).

(V) The FIP200 puncta induced by exo Ca^{2+} stimulation undergo dynamic association and dissociation with SNAP-CaMKIIβ puncta. FIP200 puncta can attach to SNAP-CaMKIIβ puncta (white arrowheads). Attached puncta can also separate (magenta arrowheads).

Scale bars: 2 μm (A-C, J, K, M-O); 1 μm (inserts in A-C, J, K, M-O); 1 μm (E-H, L, P-V).

Figure S4. CaMKIIβ-mediated phosphorylation of FIP200 controls phase separation and organization of FIP200 puncta, related to Figure 4.

(A) Purified recombinant FIP200 fragments containing NTD(1-643), CC2(1285-1396) or Claw(1396-1594) were used for *in vitro* phosphorylation in a reaction containing purified CaMKIIβ and ATP-γS with or without Ca^{2+}/CaM (indicated by + or − at the top of the figure). In the active reaction buffer containing Ca^{2+}/CaM and CaMKIIβ, phosphorylation of FIP200 fragments (indicated by red arrows) and autophosphorylation of CaMKIIβ (labeled with blue asterisks) were detected. In the reactions shown in lane 1, purified FIP200 fragments were not added. The signal is detected by anti-thiophosphate ester antibody.

(B) Table showing the FIP200 residues (S105, S161, T269, S415, T1127, T1465 and S1484) that are phosphorylated by CaMKIIβ. Residues were identified by MS analysis of *in vitro*-phosphorylated FIP200 fragments.

(C-E) Tandem mass spectrum of the doubly charged peptides SVEHVSPDTADAESGKEIR, TLMTIEKDQCISELISR and LMSQSMSSVSSR showing phosphorylation of T269 (C), T1127 (D) and S1484 (E), respectively.

(F) FIP200(T269A, T1127A or S1484A) mutants interact with ULK1, ATG13 and ATG101 in GFP-Trap assays.

(G-J) In *FIP200* KO cells upon amino acid starvation, wild-type FIP200 and FIP200(S105A, S161A, S415A or T1465A) mutants completely rescue the formation of WIPI2 puncta (G) and LC3 puncta (H), while FIP200(T269A, T1127A or S1484A) mutants show attenuated rescuing activity (G-J). The FIP200(T269A&T1127A&S1484A) mutant does not further reduce the number of WIPI2 puncta and LC3 puncta compared to each single mutation. Quantifications of WIPI2 puncta and LC3 puncta are shown in (I) and (J), respectively (n=23, 22, 21, 22, 22, 24, 21, 23, 24 and 25 cells for bars from left to right in (I). n=26, 24, 24, 23, 24, 25, 24, 26, 22 and 31 cells for bars from left to right in (J)).

(K) FRAP analysis of wild-type FIP200 puncta and mutant FIP200 puncta formed in response to exo Ca^{2+} stimulation (left) and under starvation conditions (right).

(L-P) In starved *FIP200* KO cells, the ratio of FIP200(T269A, T1127A or S1484A) puncta colocalized with endogenous WIPI2 puncta is lower compared to wild-type FIP200 puncta. Quantification is shown in (L) (n=26, 24, 24, and 25 cells for bars from left to right).

n.s.: no significance; ***: $p<0.001$. Data are shown as mean ± SEM in (I, J, K). Scale bars: 5 μm (G, H, M-P); 2 μm (inserts in M-P).

Figure S5. Phosphomimetic FIP200 promotes autophagosome formation, related to Figure 5.

(A-D) Phosphomimetic FIP200(T269D, T1127D or S1484D) mutants rescue the defective formation of endogenous WIPI2 puncta (A) and LC3 puncta (C) in starved *FIP200* KO cells. Quantifications of WIPI2 and LC3 puncta are shown in (B) and (D), respectively (for bars from left to right: n=29, 22, 31, 22 and 24 cells in (B); n=22, 23, 24, 25 and 26 cells in (D)).

(E-L) In control cells under normal (E and I) and starvation conditions (G and K), the numbers of endogenous WIPI2 puncta (E-H) and LC3 puncta (I-L) are higher in cells expressing FIP200(T269D, T1127D or S1484D) than in cells expressing wild-type FIP200. Quantifications of the number of WIPI2 puncta and LC3 puncta under normal and starvation conditions are shown in (F), (H), (J) and (L), respectively (n=27, 28, 27, 27 and 26 cells for bars from left to right in (F); n=25, 28, 28, 27 and 29 cells for bars from left to right in (H); n=23, 24, 27, 24 and 26 cells for bars from left to right in (J); n=33, 38, 32 30 and 31 cells for bars from left to right in (L)).

(M-P) Multi-SIM analysis reveals that after HBSS starvation for 40 min to 1 h, *FIP200* KO cells expressing mGFP-FIP200(T269D, T1127D or S1484D) form more ring-like structures and more puncta than *FIP200* KO cells expressing wild-type mGFP-FIP200. Quantification of the number of ring structures per focal plane is shown in (N) (n=42, 37, 35 and 35 cells for bars from left to right). Quantification of the number of puncta per focal plane is shown in (P) (n=28, 24, 29 and 26 cells for bars from left to right). More mGFP-FIP200 puncta can be detected by high-resolution multi-SIM imaging than confocal imaging.

(Q and R) Time-lapse analysis of the progression of mGFP-FIP200(T269D)/WIPI2-mCherry dots (Q) or mGFP-FIP200(S1484D)/WIPI2-mCherry dots (R) (indicated by arrowheads) into ring structures and their dissociation from rings in *FIP200* KO cells during HBSS starvation. In cells expressing FIP200(T269D), the progression of this process is slightly faster than in cells expressing wild-type FIP200 (shown in Figure 4G).

n.s.: no significance; *: $p<0.05$; **: $p<0.01$; ***: $p<0.001$. Data are shown as mean ± SEM in (B, D, F, H, J, L, N, P). Scale bars: 5 μm (A, C, E, G, I, K); 2 μm (M and O); 1 μm (Q, R, and inserts in M and O).

Figure S6. Depleting CaMKIIβ attenuates the amplitude, duration and propagation of ER Ca^{2+} oscillations during autophagy induction, related to Figure 6.

(A and B) Lysosome Ca^{2+} release triggered by HBSS in control cells and *CaMKIIβ* KO cells. Quantification of the amplitude of lysosome Ca^{2+} release is shown in (B) (n=29 for control cells, n=30 for *CaMKIIβ* KO cells).

(C) In *CaMKIIβ* KO cells, HBSS starvation triggers lysosomal Ca^{2+} release that induces formation of mCherry-FIP200 puncta (arrowheads) on the lysosomes.

(D) Images showing dynamic fluorescence signals in Torin1-treated control cells and Torin1-treated *CaMKIIβ* KO cells. The ER Ca^{2+} transients are abundant and propagate into large areas of the ER network in 2 Torin1-treated control cells (in the areas enclosed by dashed lines and labeled as C1 and C2). The trace diagrams showing dynamic fluorescence changes in the whole cell (Torin1-treated control cells C1 and C2 and a Torin1-treated *CaMKIIβ* KO cell) are presented on the right.

(E-G) Expressing CYB5-CN21 reduces the number of endogenous FIP200 puncta (E) and LC3 puncta (F) in starved control cells. Quantifications of the FIP200 puncta and LC3 puncta are shown in (G) (n=25 and 25 for control cells from left to right, and n=26 and 25 for cells expressing CN21-CYB5 from left to right).

(H) Expressing CYB5-CN21 greatly attenuates the number, amplitude and duration of ER Ca^{2+} transients in *EI24* KO cells.

(I-L) *CaMKIIβ* KD or expression of CN21-CYB5 reduces the number of endogenous FIP200 puncta (I), WIPI2 puncta (J) and LC3 puncta (K) in *EI24* KO cells. Quantification is shown in (L) (n=33, 32, 20, 32, 38, 25, 29, 31 and 20 cells for bars from left to right).

***: $p<0.001$. Data are shown as± SEM in (B, G, L). Scale bars: 5 μm (D-F, I-K); 2 μm (C); 1 μm (inserts in C).

Figure S7. Disease-related CaMKIIβ mutations impair autophagy, related to Figure 7.

(A and B) Compared to wild-type SNAP-CaMKIIβ, SNAP-CaMKIIβ(P139L, E237K, R284S and K301E) show impaired ability to rescue the number of endogenous FIP200 puncta in starved *CaMKIIβ* KO cells. Quantification of the number of FIP200 puncta is shown in (B) (n=27, 29, 22, 22 and 21 cells for bars from left to right).

(C and D) CaMKIIβ(P139L or R284S) mutants show a more diffuse distribution compared to wild-type CaMKIIβ (Figure 2G). Upon starvation, CaMKIIβ(P139L)

forms both small and large puncta. CaMKIIβ(R284S) forms predominantly large puncta.

(E) The size of puncta formed by wild-type and mutant CaMKIIβ in *CaMKIIβ* KO cells under starvation (n=69 puncta from 26 wild-type CaMKIIβ-transfected cells, 604 puncta from 15 CaMKIIβ(P139L)-transfected cells, 930 puncta from 20 CaMKIIβ(K301E)-transfected cells and 1535 puncta from 13 CaMKIIβ(R284S)-transfected cells). The majority of wild-type CaMKIIβ puncta are smaller than 50 pixels. Images were taken with the same laser power and exposure time. The size (in pixels) of CaMKIIβ puncta was analyzed with GraphPad Prism.

(F-I) Relationship between FIP200/WIPI2 puncta and mutant CaMKIIβ puncta in starved *CaMKIIβ* KO cells. The FIP200/WIPI2 dots colocalize with CaMKIIβ puncta in *CaMKIIβ* KO cells expressing wild-type CaMKIIβ (F, magenta arrowheads). The few CaMKIIβ(E237K) puncta also interact with FIP200/WIPI2 puncta (G, magenta arrowheads). The abnormally large CaMKIIβ(P139L or R284S) puncta show no interaction with FIP200/WIPI2 puncta (white arrowheads in H, I).

(J and K) In *CaMKIIβ* KO cells expressing SNAP-CaMKIIβ(R284S), small FIP200 dots (arrowheads) persist on WIPI2 ring structures (J), or the FIP200/WIPI2 dots (arrowheads) fail to progress into ring structures (K).

(L and M) In starved control cells, RFP-GFP-LC3 forms a large number of ring-like structures. Red-only LC3 structures indicate acidified autolysosomes. In control cells expressing SNAP-CaMKIIβ(E110K), a large number of small yellow GFP-RFP-LC3 structures accumulate after 3 h starvation. The degree of defects in formation of LC3 structures depends on the expression level of SNAP-

CaMKIIβ(E110K). A higher level of SNAP-CaMKIIβ(E110K) causes a stronger defect.

**: $p<0.01$; ***: $p<0.001$. Data are shown as mean ± SEM in (B). Scale bars: 5 μm (A); 2 μm (C, D, L, M); 1 μm (F-K, and inserts in C, D, L, M).